Engineered Microenvironment for Quantitative Studies of Neutrophil Migration

by

Henry Hung Li Chung

Submitted in Partial Fulfillment of the Requirement for

the Degree of Doctor of Philosophy

Supervised by Professor James L. McGrath and

Professor Richard E. Waugh

Department of Biomedical Engineering

Arts, Sciences and Engineering

Edmund A. Hajim School of Engineering and Applied Sciences

University of Rochester

Rochester, NY

2015

ProQuest LLC.
789 East Eisenhower Parkway
P.O. Box 1346
Ann Arbor, MI 48106 - 1346

Biographical Sketch

The author was born in Kaohsiung, Taiwan, on April 7th, 1984. He nearly completed his primary school education in Taiwan and spent the rest of his schooling in the USA. He graduated from the Brooklyn Technical High School in 2002 in the concentration of Mathematics and Science and received his Bachelor of Engineering degree in Biomedical Engineering from the Stony Brook University in 2006. Thereafter, he enrolled in the Biomedical Engineering graduate program at the University of Rochester and researched under the supervision of Dr. James McGrath and Dr. Richard Waugh. He completed his Master of Science degree from the University of Rochester in 2008.

List of Publications

- H.H. Chung, C.K. Chan, T.S. Khire, G.A. Marsh, A. Clark Jr., R.E. Waugh, and J.L. McGrath. (2014) "Highly permeable silicon membranes for shear free chemotaxis and rapid cell labeling", *Lab Chip*, **14**, 2456-2468.

- C.M. Baker, W.A. Comrie, Y.M. Hyun, H.L. Chung, C.A. Fedorchuk, K. Lim, C. Brakebusch, J.L. McGrathb, R.E. Waugh, M. Meier-Schellersheim, and M. Kim. (2012). "Opposing roles for RhoH GTPase during T-cell migration and activation", *Proc. Natl. Acad. Sci.*, **109**, 10474-10479.

- W. Domm, L. Brooks, H.L. Chung, C. Feng, W.J. Bowers, G. Watson, G, J.L. McGrath, and S. Dewhurst. (2011). "Robust antigen-specific humoral immune responses to sublingually delivered adenoviral vectors encoding HIV-1 Env: association with mucoadhesion and efficient penetration of the sublingual barrier", *Vaccine*, **29**, 7080-7089.

- Y.M. Hyun, H.L. Chung, J.L. McGrath, R.E. Waugh, and M. Kim. (2009). "Activated integrin VLA-4 localizes to the lamellipodia and mediates T cell migration on VCAM-1", *J. Immunol.*, **183**, 359-369.

- G.F. Elphick, P.P. Sarangi, Y.M. Hyun, J.A. Hollenbaugh, A. Ayala, W.L. Biffl, H.L. Chung, A.R. Rezaie, J.L. McGrath, D.J. Topham, J.S. Reichner, and M. Kim M. (2009). "Recombinant human activated protein C inhibits integrin-mediated neutrophil migration", *Blood*, **113**, 4078-85.

Acknowledgements

The presented works emerged from the collaboration of many people. First I would like to thank my advisors, Dr. James McGrath and Dr. Richard Waugh, for their guidance, troubleshooting, and moral support throughout the years. Not only are they insightful and dedicated to scientific truths, their compassionate good nature made my research experience enjoyable. I would also like to thank the members of the Nanomembrane Research Group and the Vascular Biophysics Group. The former is constantly perfecting the membrane technology that I used to create microfluidic systems, while the latter inspire the big picture that guides the designs and applications. In particular, Richard Bauserman, Dr. Michael Bindschadler, Dr. David Fang, Dr. Thomas Gaborski, Dr. Dooyoung Lee, Dr. Elena Lomakina, and Margaret Youngman taught me the fundamentals that help launch my research.

My thesis committee members, Dr. Edward Brown III, Dr. Lisa DeLouise, and Dr. Minsoo Kim periodically offered different perspectives and constructive criticisms to keep my research work in check. Lauren Brooks, Tara Capece, Dr. Steve Dewhurst, and Dr. Young-Min Hyun provided the collaborative opportunities that culminated in four journal publications, with one more potentially on the way.

In particular, I would also like to thank Dr. Morton Ehrenberg, Dr. Jessica Snyder, Dr. Kuldeepsinh Rana, Dr. Gram Marsh, Dr. Anant Agrawal, Nakul Nataraj, Charles Chan, Jon-Paul DesOrmeaux, Tejas Khire, Dr. Joshua Winans, Gregory Madjeski, and Karl Smith for their companionship at and beyond work. Last but not least, I thank my friends and families, who are always there to support and cheer.

Abstract

Cell migration is present in virtually all life processes, including fertilization, embryogenic development, immune response, wound healing, and tumor metastasis. To improve the treatment of diseases associated with these various life processes, it is important to understand the underlying mechanisms of cell migration involved. This often requires that we recreate the environment that leads to and supports the continuous migration of cells. Here, we present two engineering approaches toward such a goal, with the additional emphasis that cell migration can be conducted in the absence of fluid flow, a mechanical stimulus that is known to influence cell behaviors. We chose the primary human neutrophil, which is highly motile and sensitive to both fluid flow and chemoattraction, as the model cell type for all our studies.

In the first approach, we used fluid flow to create a linear and time-invariant gradient of chemoattractants to guide the migration of neutrophils. A thin and porous membrane was used to screen off the associated flow forces while still permitting the diffusion of the gradient to the neutrophils. We showed that the membrane-based system is capable of directing neutrophil migration without the bias from fluid flow, and allowed within minutes the exchange of media to label and wash the migrated neutrophils. To assess the reduction of flow forces enabled by the membrane, we developed an analytical model to predict the direction and the magnitude of flow within the system. The validity of the model was verified both experimentally and numerically with particle tracking and computational fluid mechanic (CFM) simulations. We also performed total internal reflection fluorescence (TIRF) microscopy to verify the preservation of the gradient after

its diffusion through the membrane.

In the second approach, we created immobilized gradients of the chemoattractant interleukin 8 (IL-8) and the intercellular adhesion molecule 1 (ICAM-1) in the attempt to guide neutrophil migration. A gradient of soluble factors is first established, and the resulting difference of concentration over space leads to a bias in the binding of the soluble factors unto the substrate, forming an immobilized gradient. The immobilization is mediated by a combination of different physicochemical linkages, including electrostatic attraction, protein/protein interactions, and covalent bonding. We showed through labeling with fluorescent antibody that the number of IL-8 or ICAM-1 immobilized in a given area could be controlled, and varied over distances to form different gradient profiles. We further showed that our immobilization procedure does not affect the ability of IL-8 and ICAM-1 to activate and bind the neutrophils. However, with all the immobilized gradients that we have created so far, none were able to effectively promote the directed migration of neutrophils in long distances. Additional work is therefore required to establish if an immobilized gradient of either IL-8 or ICAM-1 alone can direct the migration of neutrophils in long distances, and if it does, what are the required conditions. Currently, our efforts suggest that the membrane-based chemotaxis system is a more attainable platform for promoting a directed migration that is shear-free.

The presented thesis work offers many potential applications. The membrane-based chemotaxis system, which has the general structure of two compartments separated by a membrane, resembled many physiological structures, including bone marrow, blood vessel, blood-brain barrier, hepatic portal vein, nephron in the kidneys, and alveolus in

the lungs, and therefore serves as a versatile platform for understanding the transport phenomenon and the biochemical signaling in the aforementioned tissues. With improvements, the membrane-based system can also host larger-scale cell culture for protein production and tissue engineering. The protocols established for the gradient immobilization also provided many valuable references. These include: 1. A 1st order approximation of the reagents and the times required to fully saturate the substrate to be functionalized. 2. An automated image processing tool to measure the various parameters of cell motility. 3. A statistical framework to detect the presence of a directed migration. In theory, the standard operating procedures established are applicable to the surface functionalization with other peptides and proteins.

Contributors and Funding Sources

This work was supported by a dissertation committee consisting of Dr. Richard Waugh (co-advisor, Biomedical Engineering), Dr. James McGrath (co-advisor, Biomedical Engineering), Dr. Edward Brown III (Biomedical Engineering), Dr. Lisa DeLouise (Biomedical Engineering), and Dr. Minsoo Kim (Microbiology and Immunology).

Chapter 2 and Chapter 3 were both parts of the published work in *Lab on a Chip* by H.H. Chung (Biomedical Engineering), C.K. Chan (Chemical Engineering), T.S. Khire (Biomedical Engineering), G.A. Marsh (Biomedical Engineering), A. Clark Jr. (Mechanical Engineering), R.E. Waugh (co-advisor from Biomedical Engineering), and J.L. McGrath (co-advisor from Biomedical Engineering) [*Lab Chip*, **14**, 2456-2468 (2014)]. The core technology used in the making of the device, the porous nanocrystalline silicon (pnc-Si) membrane, was invented by Dr. Chris Striemer at the University of Rochester (Electrical Engineering) and is now commercially available through Simpore Inc. in different chip formats and a range of pore specifications. Dr. Chris Striemer, Jon-Paul DesOrmeaux, and Charles Chan co-invented the silicon nitride (SiN) grid technology used to boost the mechanical strength of the pnc-Si membrane. In particular, Charles Chan of Simpore Inc. aided in the customization of the membrane chip that was used specifically for the works in Chapter 2, at both the design and the manufacturing level. Dr. Graham Marsh assisted in the total internal reflection fluorescence (TIRF) microscopy to verify the presence of a soluble gradient near the

substrate floor, a feat that has not been demonstrated by other investigators for their membrane-based chemotaxis systems.

Dr. Alfred Clark Jr., Tejas Khire, Dr. James McGrath, and Dr. Richard Waugh all assisted in the development of the analytical model described in Chapter 3. Dr. Richard Waugh proposed the use of a cable theory for the modeling of system flow, in which each flow path is treated as a resistor. Dr. James McGrath supplemented the use of Hagen-Poiseuille and Dagan equations to calculate the resistance of each flow path, and helped in relating the Darcy's permeability of the pnc-Si membrane to its pore geometry and pore spacing. The use of Darcy's permeability greatly simplified and expedited the CFM simulations of system flow (Chapter 3), which subsequently validated the analytical model. Tejas Khire and Dr. Alfred Clark Jr. each provided the key mathematical manipulations that actualized the solution to the analytical model. Specifically, Tejas Khire derived the recurrence relation that generalizes the system flow, and Dr. Alfred Clark Jr. answered the closed form solution to the recurrence relation. The Supplementary Information Section of Chapter 3 (Section 3.7), which explained the analytical model of system flow in details, is based mostly on the correspondence with Dr. Alfred Clark Jr. Lastly, Dr. Michael Bindschadler wrote the core engine of the cell tracking program, which expedited the analysis of cell migration that is vital throughout our studies (Chapter 2 and Chapter 4).

Funding for this research is supported by the National Institutes of Health under program project grant no. PO1HL018208.

Table of Contents

List of Tables

List of Figures

Chapter 1
Background

1.1 The Neutrophil and Its Clinical Relevance

Neutrophils are the most abundant human immune cells, averaging approximately 3 million cells per milliliter of blood and being produced at a rate of ~5-10 × 10^{10} cells per day in the bone marrow [1, 2]. Neutrophils constantly patrol the body through blood circulation and form the first line of immune defense against foreign pathogens [3]. During injury, soluble or surface-presenting factors from the pathogens and infected cells trigger neutrophil emigration from the blood to the site of injury. The entire process includes receptor-mediated activation, adhesion to the blood vessel wall, exit from the blood vessel, migration through the extracellular matrix (ECM) to the sites of injury, and the attack on pathogens [4-6] (Fig. 1.1). Each step in the process is coordinated by a number of intracellular and membrane-bound mediators.

In subsequent sections, we provide an overview of the biology of the neutrophil, focusing specifically on the mechanism of signal sensing and adhesion that the neutrophil uses to migrate directionally (Section 1.1.2 – 1.1.6). We discuss previous studies on neutrophil chemotaxis (Section 1.1.7) and prior chemotaxis platforms (Section 1.2.1 – 1.2.8) that inspired our design of novel microenvironments to study neutrophil migration.

Lastly, we discuss the underlying rationale for using surface-bound IL-8 (a chemoattractant) and ICAM-1 (an adhesion molecule) as a potential platform for inducing the directed migration of neutrophils (Section 1.3.1 – 1.3.3).

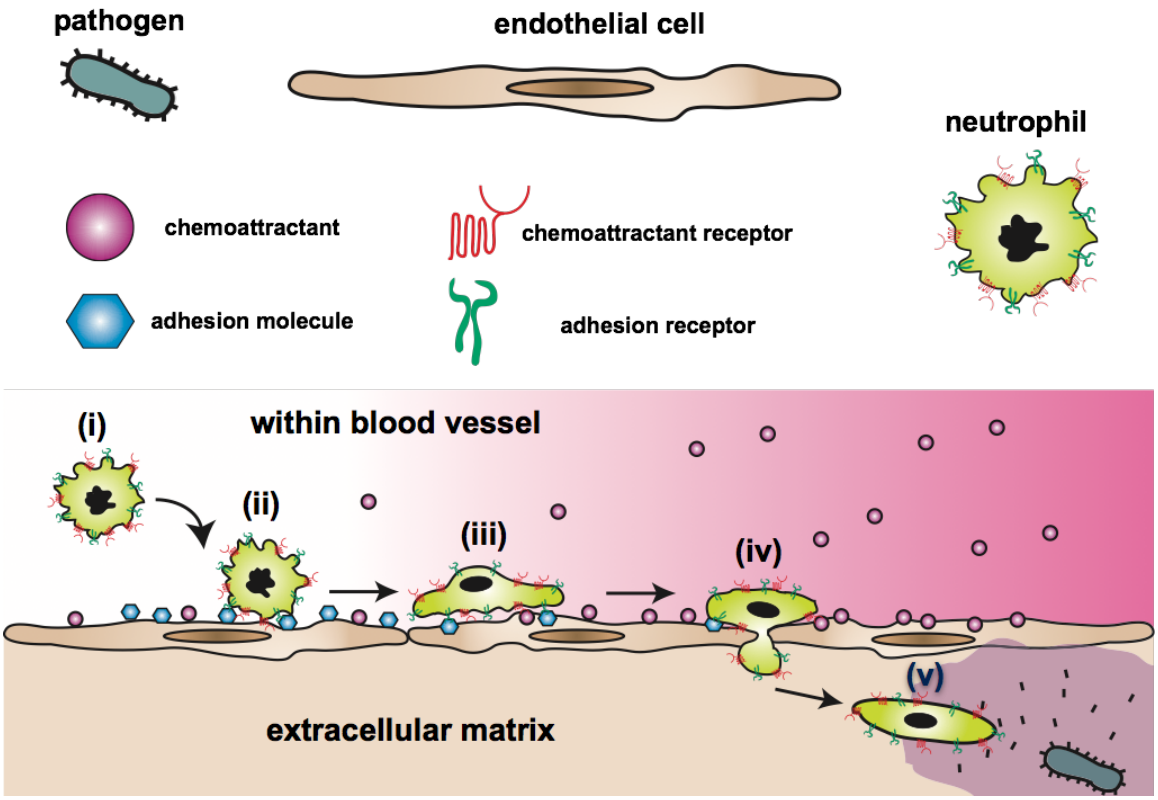

Figure 1.1: Neutrophil adhesion cascade. Neutrophils in blood circulation (i) periodically visit the endothelial cells that form the vessel wall. When the endothelial cells sense foreign pathogens, they release soluble activators (*e.g.*, IL-8) into the blood stream to alert the neutrophils. Some of these soluble activators bind to the vessel wall to enhance neutrophil recruitment. The activated neutrophils subsequently become firmly-adherent (ii) and undergo lateral migration (iii). Some neutrophils transmigrate out of the blood vessel (iv) to seek and attack the foreign pathogens (v) in the extracellular matrix. The adhesion and the migration entailed in step ii through v are coordinated *via* the adhesion molecules on the endothelium (*e.g.*, ICAM-1).

1.1.1 Neutrophil-related Pathologies

Neutrophil dysfunctions are related to a number of severe pathologies, including cystic fibrosis, chronic obstructive pulmonary disease (COPD), rheumatoid arthritis (RA), leukocyte adhesion deficiency (LAD), sepsis, and complications related to autoimmunity and cancer [7, 8]. The most notable of these is sepsis, which is the imbalance of the inflammatory response to infection [9, 10]. Sepsis is the leading cause of death in intensive care units [11], affecting more than 700,000 people in the United States each year with an associated mortality rate of ~20% [12]. While the pathological features of sepsis are diverse, growing evidence indicates that the fundamental etiology of sepsis to be the imbalance between excess and inadequate immune response [13, 14].

The neutrophils, being key mediators of the innate immune system [3], are consequently a major target of study for understanding sepsis [15-18]. The only Food and Drug Administration (FDA)-approved drug for the treatment of sepsis, recombinant activated protein C (rhAPC), is thought to counteract sepsis in part through its inhibition of neutrophil migration [16]. However, rhAPC was subsequently withdrawn from use because increased incidence of bleeding led to additional pathology and improved patient outcomes could not be demonstrated [10, 19].

1.1.2 Chemotaxis

Neutrophils recognize a specific set of commonly-encountered chemoattractants that are derived either from invading microorganisms or human cells in distress. Examples of these chemoattractants include lipopolysaccharide (LPS), bacterial peptides containing

the N-formyl-methionyl-leucyl-phenylalanine (fMLP) sequence, complement component 5a (C5a), interleukin-8 (IL-8), and leukotriene B4 (LTB4). These chemoattractants are recognized by two main classes of receptors that are expressed on the surface of neutrophils: the toll-like receptors (TLRs) and the G-protein coupled receptors (GPCRs) [3, 20, 21]. In the presence of a soluble gradient, the region with a higher concentration of chemoattractants promotes a higher likelihood of receptor engagement. It is the differential engagement of receptors over the cell surface that specifies the direction of migration. We chose IL-8 and fMLP as the chemoattractants for our investigations. Both are recognized through GPCRs and are commonly used to study neutrophil migration.

1.1.3 Integrins and Neutrophil Locomotion

The firm adhesion, extravasation (exit from blood vessel), and crawling of neutrophils are all mediated by the coordinated binding and unbinding of integrins, a major class of adhesion receptors. Currently, 24 variants of integrins have been identified at the protein level [22, 23]. Depending on the cell type, cell state of maturity, and the cell-hosting microenvironment, different subsets of integrins are used to carry out specific cellular tasks [23]. For neutrophils, the β_2-integrins LFA-1 and Mac-1 are the most abundant integrins expressed, averaging around 25,000-40,000 and 45,000-60,000 copies per cell, respectively [24, 25]. All literature thus far indicates that during the immune response, Mac-1 functioning is enhanced through both increase in number (~150-500% more) and binding affinity [25, 26], whereas LFA-1 functioning is enhanced primarily through the increase in affinity alone [25-27].

1.1.4 LFA-1, Mac-1, and α_4-integrins

While the functions of different integrins are not necessarily mutually exclusive, certain integrins do have dominance over the others in particular tasks. *In vitro* and *in vivo* antibody blocking studies repeatedly indicate that LFA-1, not Mac-1, is essential in mediating the firm adhesion of neutrophils to intercellular adhesion molecule 1 (ICAM-1) on endothelium [25, 28-30]. Some publications also suggest that LFA-1 provides directional guidance to neutrophil polarization [31] and migration [32]. In particular, Dixit *et al.* [31] showed that the site of β_2-integrin engagement to ICAM-1 is also the initial site of calcium influx, and that the colocalization of high affinity state LFA-1, F-actin, and the calcium release-activated channel (CRAC) protein 1 (Orai1) only occurred in the presence of fluid flow. Based on the above observations, Dixit *et al.* [31] hypothesized that a high-affinity state LFA-1, when subjected to a flow-induced tensile force, signals *via* Orai1, which in turn elicits a localized cytoskeletal rearrangement that results in cell extension.

Mac-1 is known as the most promiscuous member of the integrin family, and can bind to at least 30 different molecules [33]. Therefore not surprisingly, Mac-1 is involved in multiple cellular tasks, including engulfment of pathogens or damaged cells (phagocytosis), release of chemical factors to kill cells (degranulation), extravasation, and migration through 3D extracellular matrix [33]. Essentially, Mac-1 seems to provide the general traction needed for the neutrophil to perform various functions, and this traction increases during an immune response. In particular, Mac-1 has been demonstrated to be more important than LFA-1 during neutrophil extravasation [34].

Another integrin member worth noting is the α_4-integrin ($\alpha_4\beta_1$). While not expressed in large number (only ~1,000 even after the neutrophils are activated) [35], α_4-integrins seem to strongly cooperate with LFA-1 in both firm arrest and directional migration [30, 32, 35]. Antibody blocking against both LFA-1 and α_4-integrin, but not Mac-1, has been shown to abolish the directed migration of neutrophils toward fMLP, whereas the blocking of LFA-1 alone does not [32]. Furthermore, antibody blocking against either LFA-1 or α_4-integrin significantly reduced the number of neutrophils that firmly arrested from flow, and this reduction is even more pronounced for the antibody blocking of α_4-integrins in LFA-1 null mice [30].

1.1.5 Chemoattractant-specific Activation of Integrins: LFA-1 v.s. Mac-1

Not only do LFA-1 and Mac-1 function differently, they are preferentially activated by different chemoattractants [22, 32]. Heit *et al.* [32] used activation state-specific antibodies to show that IL-8 promoted significantly higher levels of LFA-1 clustering than fMLP, whereas fMLP promoted a higher level of Mac-1 activation (Fig. 1.2). Furthermore, treatment of neutrophils with p38 MAP kinase inhibitor (SB203580) reduced the level of fMLP-promoted Mac-1 activation to a level comparable to IL-8-induced Mac-1 activation (Fig. 1.3). They further demonstrated through migration studies that Mac-1 is the main integrin mediating fMLP-induced chemotaxis, whereas for IL-8-induced chemotaxis LFA-1 is more important [32]. For fMLP-induced chemotaxis, antibody blocking of Mac-1 significantly reduced the number of neutrophils that migrated directionally, whereas the blocking of either LFA-1 or the α_4-integrins alone

had no significant effect. However, the blocking of both LFA-1 and the α_4-integrins also significantly reduced the number of chemotaxing neutrophils, even when there is no blocking of Mac-1. The above observations led Heit *et al.* to conclude that Mac-1 is essential for fMLP-induced chemotaxis, and that LFA-1 and the α_4-integrins are also required together to provide directionality to neutrophil migration. For IL-8-induced chemotaxis, however, it is the antibody blocking of LFA-1, but not any combination of Mac-1 or the α_4-integrins, that significantly reduces the number of chemotaxing neutrophils.

1.1.6 LFA-1 and Mac-1 Localization during Cell Migration

Not only do LFA-1 and Mac-1 function differently, their localization may also differ as neutrophils migrate. It was noted that in response to stimulation by chemoattractants, active LFA-1 formed dot-like clusters throughout the basal surface of the neutrophil, whereas active Mac-1 localized to a single patch [32], most often at the uropod (back) of a polarized neutrophil [36, 37]. Since traction force mapping also showed the uropod to be the region with highest stress on migrating neutrophils [38, 39], it is highly likely that it is Mac-1 that facilitates the adhesion at the uropod. With the aid of our shear-free chemotaxis system (Chapter 2), which enables the labeling and washing of migrating cells, Mac-1 and LFA-1 could be labeled sequentially, allowing us to visualize how the two integrins reorganize spatially and temporally during the initial polarization and subsequent migration of neutrophils.

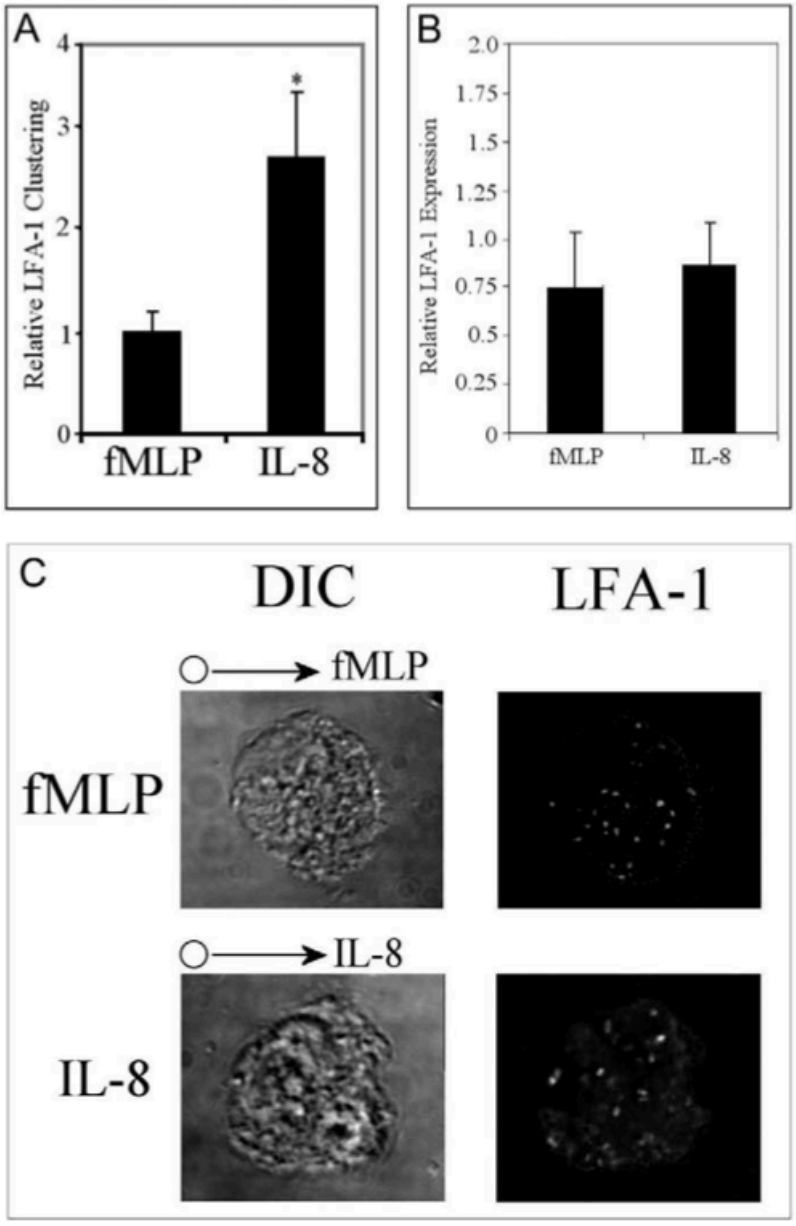

Figure 1.2: LFA-1 activation and clustering after stimulation with IL-8 and fMLP. After stimulating with IL-8 and fMLP, neutrophils were labeled with activation state-specific LFA-1 antibody to assess the relative fold change (with respect to baseline) in the expression of activated LFA-1. A statistically significant fold change was observed in the clustering of activated LFA-1 (a), but not in the overall expression (b). Representative images of labeled neutrophils during fMLP- and IL-8- mediated chemotaxis (c). The fluorescence clustering is more pronounced during an IL-8-mediated chemotaxis. Figure from "Fundamentally different roles for LFA-1, Mac-1 and α4-integrin in neutrophil chemotaxis" by Heit *et al.*, *J Cell Sci.*, 118:5205-20. Copyright 2005 by Elsevier Inc. Reprinted with permission.

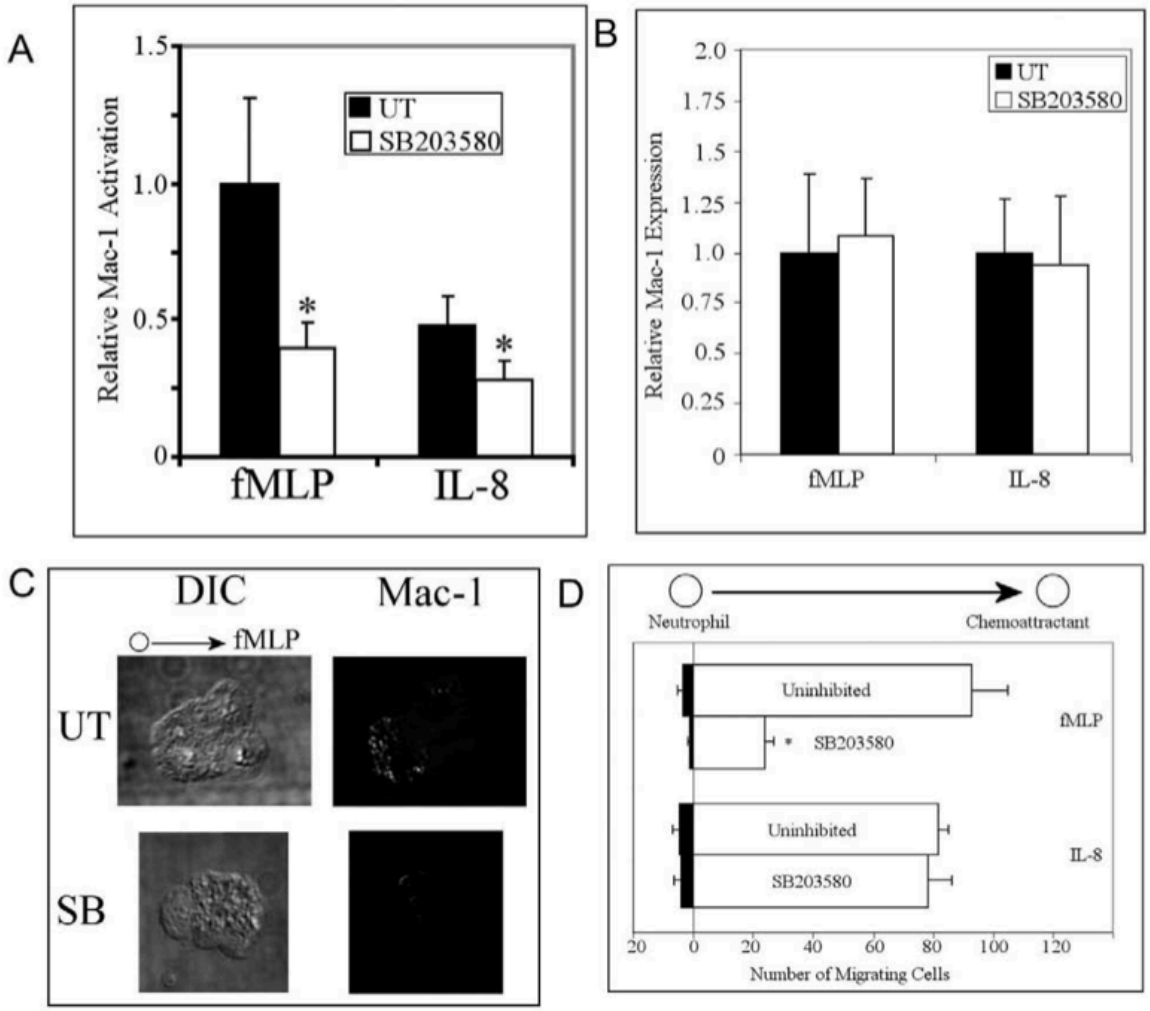

Figure 1.3: Mac-1 activation after stimulation with IL-8 and fMLP. The neutrophils treated with or without the p38 MAP kinase inhibitor (SB203580) were stimulated either with IL-8 or fMLP. The neutrophils were then labeled with activation state-specific Mac-1 antibody (a) or activation-independent Mac-1 antibody (b). The relative fold change with respect to baseline is statistically significant in (a) but not in (b). Representative images of migrating neutrophils labeled with the activation state-specific Mac-1 antibody during fMLP-mediated chemotaxis (c). Most of the activated Mac-1 is found in the uropod of the migrating neutrophil (away from the higher concentration of fMLP). For the neutrophil treated with SB203580, substantially less activated Mac-1 was observed. After treatment of the neutrophils with SB203580, the number of neutrophils that migrated toward the higher concentration of fMLP is also significantly lower in comparison to the untreated control (d). Figure from "Fundamentally different roles for LFA-1, Mac-1 and α4-integrin in neutrophil chemotaxis" by Heit *et al.*, *J Cell Sci.*, 118:5205-20. Copyright 2005 by Elsevier Inc. Reprinted with permission.

1.1.7 IL-8-mediated Chemotaxis

With the aid of a flow-based gradient generator, Lin *et al.* were able to create linear IL-8 gradients with different steepness and mean level of concentration to rigorously promote the chemotaxis of neutrophils on a fibronectin-coated substrate [40]. Prior to describing the study of Lin *et al.*, however, it is necessary to describe the three parameters that they used to characterize neutrophil migration: motility index (MI), chemotactic index (CI), and the effective chemotactic index (ECI). The motility index is defined by the ratio of the start-to-end displacement of a cell's migratory path to the total path length travelled. The MI thus describes the persistence of a neutrophil in maintaining its course toward a specific direction. The chemotactic index is defined by the ratio of a cell's displacement along the direction of the gradient to the total pathlength travelled. In this case, the direction of the gradient is specified by the principal axis of concentration difference. In essence, CI describes how effective the neutrophils are at migrating toward the higher concentration of chemoattractant. The effective chemotactic index, introduced by Lin *et al.* for this study, is defined as the product of motility index and chemotactic index (MI × CI).

Lin *et al.* [40] found that for all instances of gradient steepness tested, similar percentages of neutrophils migrated toward the direction of higher concentration, and that the migrating cells exhibited similar values of CI. However, the highest values of MI and ECI were all obtained when the mean level of the IL-8 gradient is ~3 nM (Fig. 1.4). Lin *et al.* thus concluded that the effectiveness of neutrophil chemotaxis is dictated by the mean level of IL-8 concentration, not the gradient steepness [40].

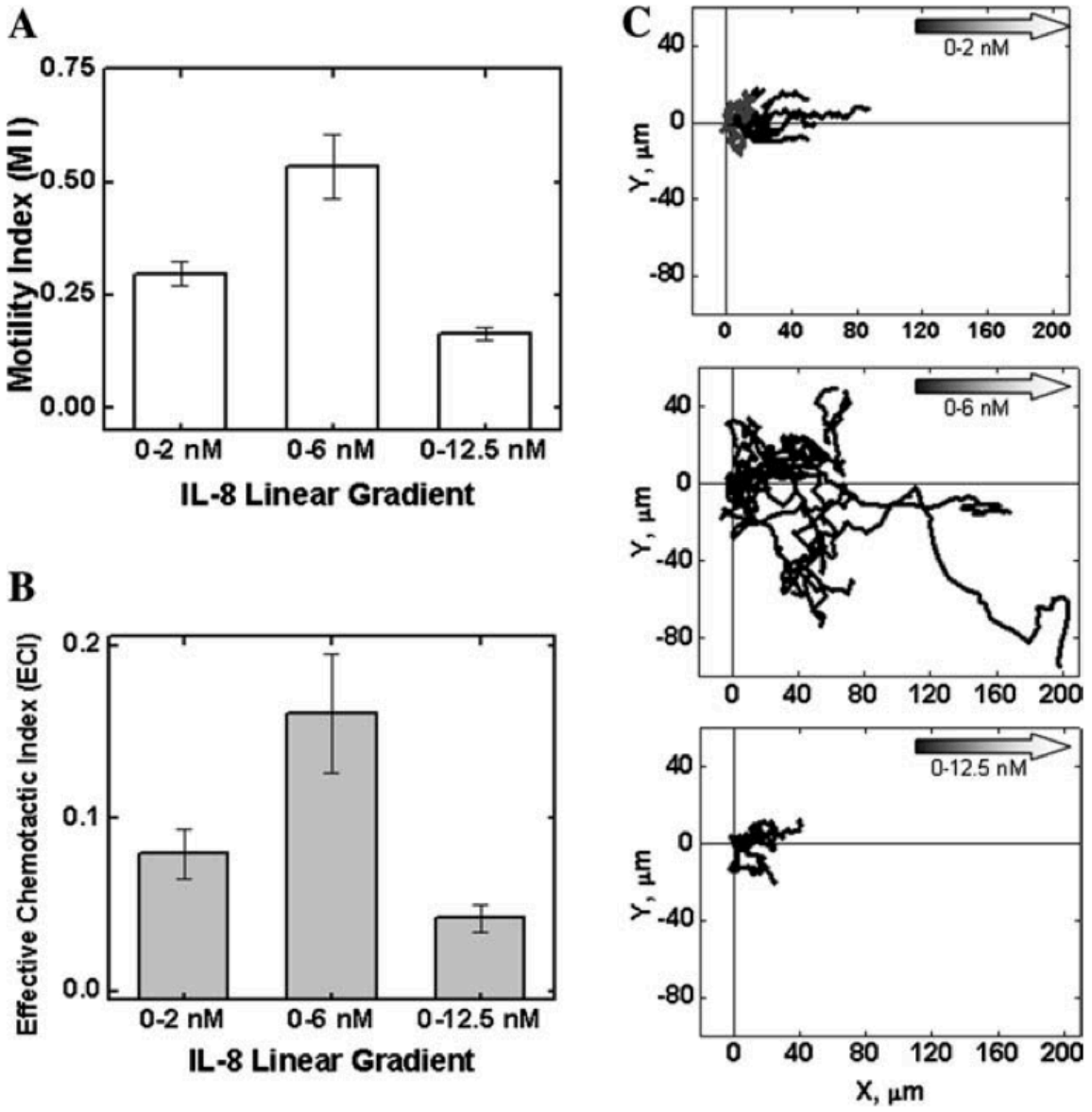

Figure 1.4: Neutrophil chemotaxis in response to varying steepness and mean level of IL-8 gradients. Both the motility index (A) and the effective chemotaxis index (B) are the highest when the mean level of the IL-8 gradient is ~ 3nM (gradient of 0-6 nM). Superimposed trajectories of twelve representative neutrophils observed under the different IL-8 gradients (C). The starting point of each neutrophil was repositioned to the origin. The mean displacement appears to be the highest for the 0-6 nM gradient. Figure from "Effective neutrophil chemotaxis is strongly influenced by mean IL-8 concentration" by Lin *et al.*, *Biochem Bioph Res Co.*, 319:576-81. Copyright 2004 by Elsevier Inc. Reprinted with permission.

In the same study, Lin *et al.* also performed migration studies on neutrophils subjected to different concentrations of uniform IL-8 (0, 0.33, 1, 3, and 9 nM) and found that 3 nM instigated the highest value of MI as well as the highest rate of random migratory dispersal. This finding therefore allowed an alternative interpretation that as long as there is a gradient of IL-8, neutrophils will be able to migrate directionally, but the baseline rate at which the neutrophils migrate is dictated by the mean level of IL-8. It is worth noting that the IL-8-mediated chemotaxis conducted by Lin *et al.* is the most rigorously controlled and quantitative study to date, and serves as a valuable reference for our IL-8-related investigations (Chapter 4).

1.2 Evolution of Chemotaxis Systems

1.2.1 Boyden Chamber, Zigmond Chamber, and Dunn Chamber

One of the earliest and the most well-known chemotaxis system is the Boyden chamber. It consists of two compartments separated by a micro-porous membrane (usually 10 μm thick, with an average pore diameter ~2-12 μm depending on the membrane) [41, 42] (Fig. 1.5a). Typically, the bottom compartment is loaded with the chemoattractant of interest and the top compartment is seeded with cells. The soluble gradient is established by the diffusion of chemoattractants through the membrane. The membrane served two major roles: a platform for cell migration and a medium that slows the diffusive flux of chemoattractant.

With the Boyden chamber, chemotaxis is assessed by the number of cells that migrated to the other side of the membrane. Since the Boyden chamber is easy to use and can run in multiple copies in parallel, it is widely used today and comes in a commercial form registered under the trademark "Transwell" cf.[43]. There are, however, three major drawbacks associated with the use of Boyden chamber, the first two of which are attributed to its diffusion-based mechanism of gradient formation: 1. The gradients produced are not linear and vary over time, eventually dissipating to uniformity; 2. Reproducibility of the migration assay is low. Since the gradients cannot be actively controlled, any unintended convection introduced by media evaporation or user handling cannot be rectified; 3. Cell migration cannot be directly visualized because the micro-porous membrane is opaque and in the way of imaging.

The chemotaxis systems later developed by Zigmond and Zicha *et al.*, known as the Zigmond chamber and the Dunn chamber, addressed the issue of visualization [44, 45]. The compartments that hold the cells and the chemoattractants are arranged laterally to fall on the same plane. In place of the opaque membrane, a thin and transparent glass channel is used to connect the compartments (Fig. 1.5b). While the issue of visualization was addressed, the drawbacks of nonlinearity and time-dependence remained because the mechanism of gradient formation is still diffusion-based.

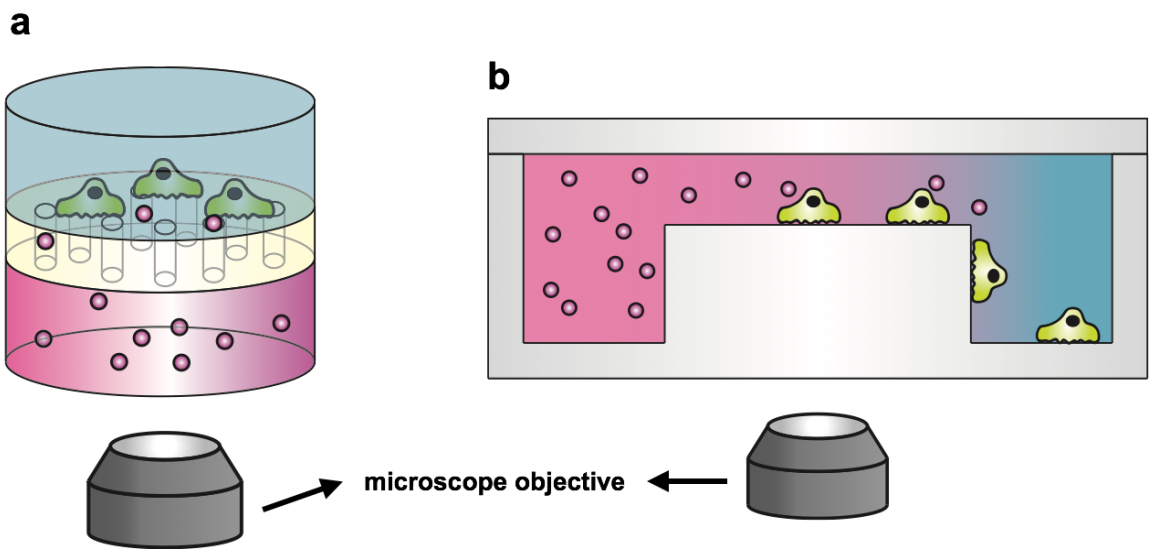

Figure 1.5: Diffusion-based gradient generators. a. Boyden chamber, in which the chemoattractant gradient is established vertically through the diffusion across a polymer membrane. **b.** Zigmond chamber, in which the gradient is established laterally through the diffusion across a small glass channel. Direct visualization of the cell migration is possible in the Zigmond chamber, but not in the Boyden chamber.

1.2.2 Under-Agarose Migration Assay

Another classical diffusion-based chemotaxis system is the under-agarose migration assay designed by Nelson *et al.* [46]. Holes were punched into a slab of agarose gel to create compartments to hold chemoattractants and cells. Configuration-wise, the under-agarose system is very similar to the Zigmond chamber and the Dunn chamber, but in place of the glass channel is an agarose gel. Since cells can crawl and climb through the agarose gel, their migratory paths are three-dimensional. This makes the cell tracking difficult on the 2D images obtained from time-lapse microscopy. The agarose gel, however, may be a more physiological representation of the ECM in terms of the

similarity in structure (three-dimensional matrix), substrate compliance, and the impedance conferred to molecular diffusion and cell migration.

1.2.3 Flow-based Systems: T-sensor and Flow-mixing Gradient Generators

To maintain and control the concentration profile of a soluble gradient, a mechanism that actively supplies and removes the chemoattractants is necessary. Fluidic transport is one such mechanism. The simplest design of a flow-based chemotaxis system is the T-sensor, composed of two merging channels that form a "T" shape [47] (Fig. 1.6). One channel carries the solution with the chemoattractants, and the other channel carries the solution without. The diffusive flux of solutes from one flow stream to the next creates the concentration gradient. At the upstream section of the merged channel, the gradient is a step function. Further downstream, the gradient becomes more linear and less steep before eventually dissipating to uniformity. At each fixed distance along the merged channel, the concentration profile is unique and stable over time. Since the T-sensor produces time-steady and pseudo-linear gradients, chemotaxis studies can be performed with higher reproducibility. In practice, however, the pseudo-linear gradients formed through the T-sensor do not span much more than 150 μm [47] due to the slowness of solute diffusion [48]. To form a pseudo-linear gradient that spans a long distance, a longer channel and more time are required.

One modification of the T-sensor, implemented by Jeon *et al.*, is the addition of a microfluidic concentration mixer upstream of the cell compartment [49]. The most basic design of the flow mixer consists of two source channels that merge and split

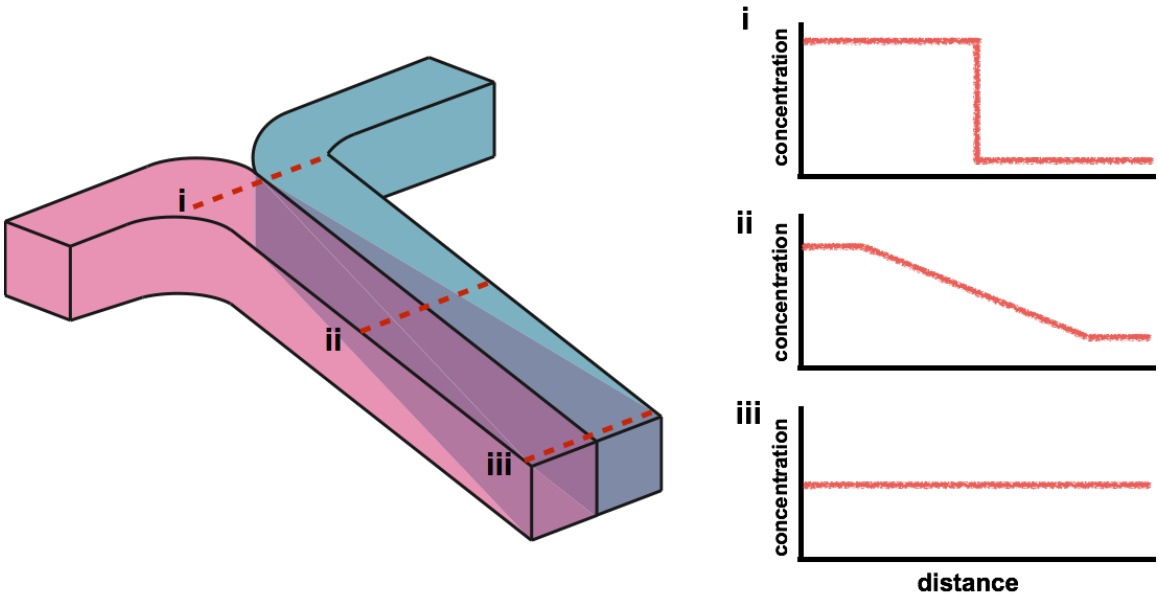

Figure 1.6: T-sensor explained. Two flow streams, each carrying a solute concentration, were merged back to back. The diffusive flux of solutes from one flow stream to the next produces a concentration gradient. **i.** at the beginning of the merge, the concentration profile is a step function; **ii.** Further along downstream, part of the gradient becomes pseudo-linear; **iii.** Eventually the gradient would dissipate to uniformity given a sufficient distance downstream.

successively to create multiple flow channels (Fig. 1.7). With each merging and splitting, a new intermediate solute concentration is created downstream. For a narrow channel (< 50 μm), thorough mixing (97%) can be achieved within one second [48]. When the well-mixed flows merge into one in the main channel downstream, the soluble gradients formed can span several cell body lengths. Gradients with more complex concentration profiles can also be made depending on how the different flows are made to interconnect. Consequently, the flow-mixed gradient generator and its design variants have been widely used in cell migration and growth studies [40, 49-52].

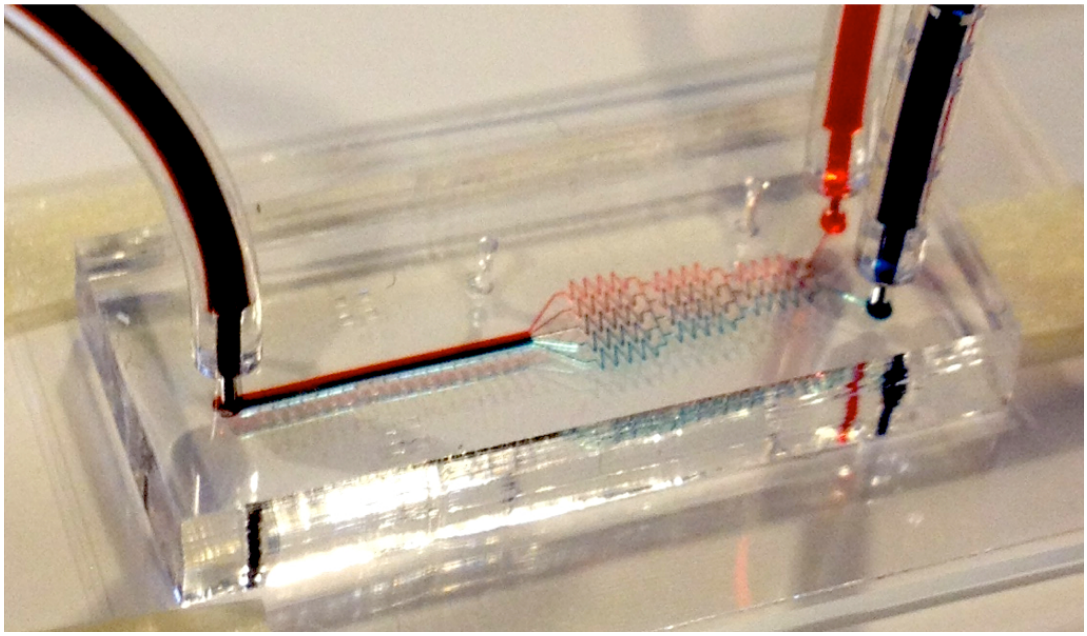

Figure 1.7: An example of the flow-mixing gradient generator. Two inlets (at the right of the image), each carrying a different color, were mixed and split repeatedly to form a range of colors, which were then combined to form a gradient of colors downstream.

1.2.4 Low Flow Chemotaxis Systems

While fluid flow enables the control over the formation of soluble gradients, the associated flow forces are known to influence a number of cellular processes, including gene regulation [53-55], protein production and trafficking [54, 55], surface receptor presentation [56], morphological change [53, 57], growth alignment [57, 58], and migration [31, 59-61]. Starting around 2005, a class of flow-based gradient generators have emerged that are designed with flow minimization as a goal [52, 62-67]. One such example is a simple variant of the flow-mixed gradient generator designed by Wang *et al.*, in which 100 μm deep trenches were etched into the merged channel to increase the cross sectional area of the cell-hosting space [52] (Fig. 1.8). While effective at low input

flow rates, the shear reduction offered is insufficient when higher flow rates are required to expedite the introduction of chemoattractants. Furthermore, the cell compartment cannot be redesigned without affecting the capacity of the system to reduce shear.

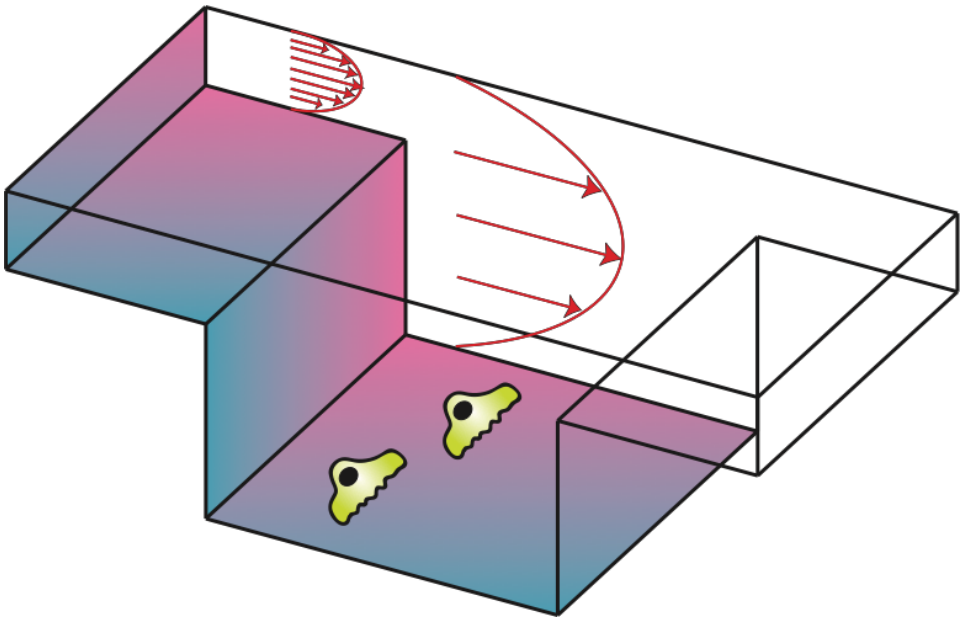

Figure 1.8: Example of shear reduction achieved through larger channel cross section. The gradient formed through the flow-mixing gradient generator propagates from left to right along the flow channel. As the channel cross section increases, the shear stress is reduced. The number of arrows represents the magnitude of wall shear stress.

1.2.5 Flow-resistive Systems

Other design strategies incorporate permeable flow-resistive dampers between the source and cell compartment. With the flow dampers, higher flow can be used to expedite the exchange of solutes while keeping the cell compartment relatively shear-free. The flow dampers can be made of hydrogels [63], microchannels [64], nitrocellulose [62],

polyester [65], or tracked-etched polycarbonate membrane [67]. The time rate of gradient establishment and the magnitude of flow reduction in the cell compartment are both dictated by the internal structure of the flow dampers and the geometry of the adjoining compartments.

1.2.6 Three-compartment Chemotaxis System

A commonly seen flow-resistive chemotaxis system consists of three compartments. Two flanking compartments serve as a source and a sink of a soluble factor to establish a gradient across the middle compartment where the cells are hosted [62-64] (Fig. 1.9). The flow dampers are integrated between the flow and the cell compartments to reduce the cell compartment flow. The time required to establish a steady-state gradient depends on the distance between the source and the sink compartment. As estimated by Shamloo *et al.* [64], ~45 min is required for a gradient of vascular endothelial growth factor (VEGF) to establish over the 1 mm span of the cell compartment in their system [64]. While well-suited for growing or slowly migrating cells, the three-compartment design does not permit the rapid establishment and reversal of a solute gradient that is necessary for studying the migratory response time of fast moving cells. One exception is the microjet system of Keenan *et al.* [68], which can establish a gradient in the middle cell compartment within 4 minutes through fast mixing of jets emitted from the source and the sink compartment. However, in the microjet system cells near the jet outputs can be temporarily exposed to high shear stress [68].

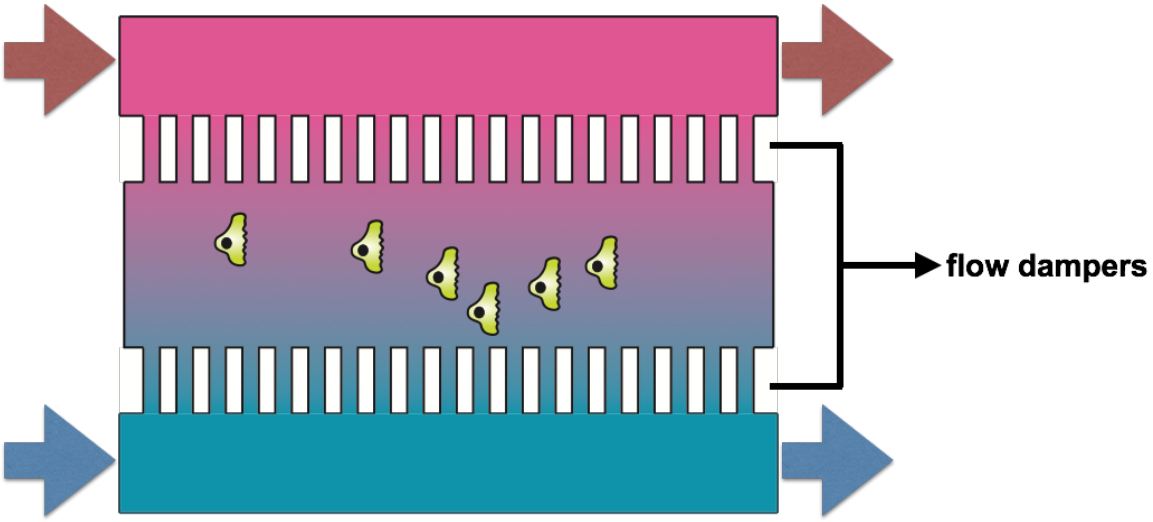

Figure 1.9: Example of three-compartment chemotaxis system. A soluble gradient is formed through the diffusive flux of solutes from the source channel on the top to the sink channel in the bottom. Cells are seeded in the middle compartment where a time-invariant gradient is established. The large arrows indicate the direction of flow. The flow dampers used to reduce the flow in the middle compartment can be made of different structures. In this case, the flow dampers are arrays of microchannels.

1.2.7 Ladder Gradient Generators

Another type of flow-resistive system consists of two parallel compartments connected by an array of small channels in between. The small channels function as a cell hosting space while the two compartments serve as a source and a sink of soluble factors to establish a gradient along the length of each small channel. When the hydrodynamic pressures at the two ends of each small channel are balanced to be equal, the small channel is free of flow. Seepage of flow into the small channels, however, can occur whenever there are fluctuations in pressure. Thus typically, the height of the small channels is constrained to be less than 10 microns to confer a high resistance to flow [69-71]. While not explicitly reported in the literature, it is likely that cell seeding is difficult

in the ladder gradient generators. Due to the high resistance of the small channels, cells may distribute preferentially to the parallel compartments during the flow seeding and may be damaged by high shear as they flow into the 10-μm tall channels. Like the three-compartment system, the time required to establish a gradient depends on the length of the small channel and may require more than 30 minutes for the promotion of chemotaxis for long distances.

1.2.8 Membrane-based Chemotaxis Systems

The chemotaxis systems that use polymer membranes (~10-24 μm) as flow dampers address the issue of slow gradient establishment [65, 67]. The lateral gradient that is formed instantly *via* flow passes vertically up through the membrane into the cell compartment (Fig. 1.10). The diffusive transport of the gradient across the thin membrane is generally within a few minutes [65, 67], much faster than the 30 minutes or more required to establish a gradient in the ladder and the three-compartment systems. Depending on the thickness, porosity (area of pores to the total area), and pore size of the membrane used, the time rate of gradient propagation into the cell compartment can be fine-tuned. For a membrane-based chemotaxis system, an ideal membrane is one that confers a high resistance to flow but a low resistance to diffusion. Since the membrane is also in the way of imaging, it should be optically transparent and low in background fluorescence to allow a high quality observation of the cell migration. The polymer membranes used by Kim *et al.* [65] and VanderSarl *et al.* [67], however, do not meet this latter criterion because they are optically opaque.

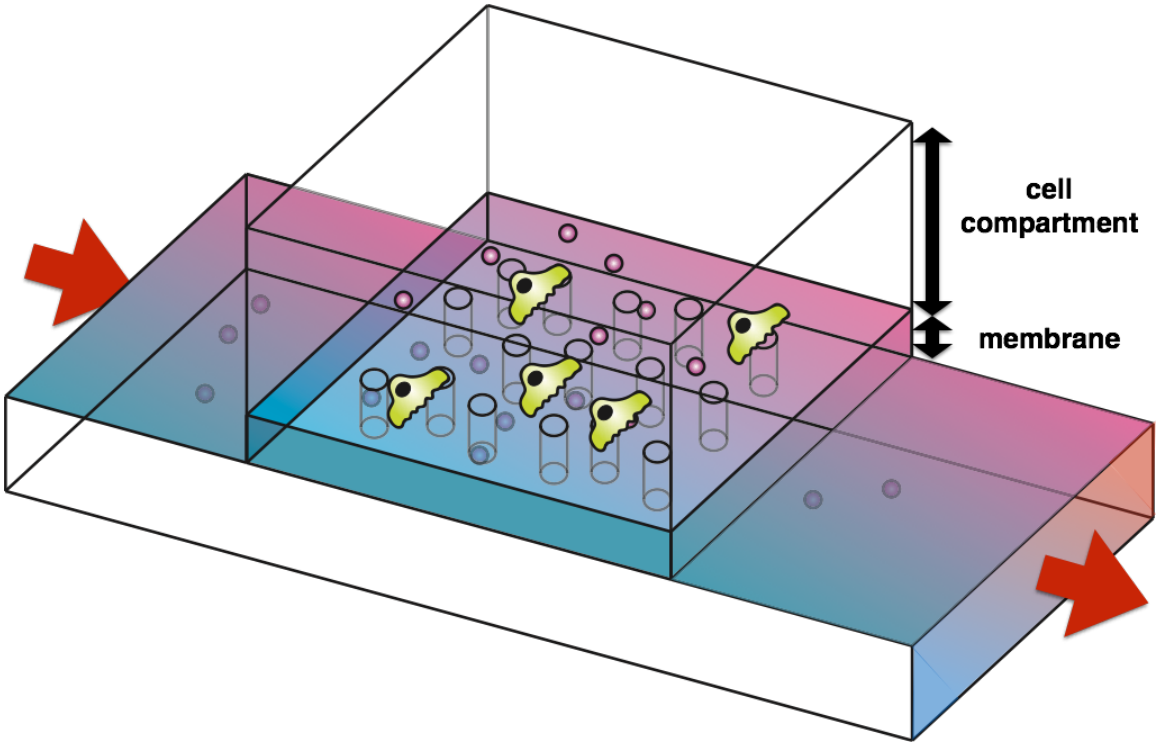

Figure 1.10: Example of membrane-based chemotaxis system. The gradient formed through the flow-mixing gradient generator propagates from left to right along the flow channel and diffuses up through the polymer membrane to direct the migration of the cells seeded on the membrane. The red arrows indicate the in and out fluid flow. When using an inverted microscope, the visualization of cell migration is impossible since the membrane is opaque and in way of the imaging.

In Chapter 2, we employ an ultrathin, nanoporous membrane, termed porous nano-crystalline silicon (pnc-Si) membrane [72], as the flow damper in our membrane-based chemotaxis system. Since the pnc-Si membrane is molecularly thin (~20 nm) and sufficiently porous (porosity ~10%), the diffusive transport of solutes across the membrane is six orders of magnitude faster the polymer membranes used by Kim *et al.* [65] and Vandersarl *et al.* [67]. Despite being thinner and more porous, the resistance of

the pnc-Si membrane to flow is still on par with that of the polymer membranes because the pnc-Si membrane has smaller average pore radius (15-40 nm vs the 200-350 nm in the polymer membranes). Another major advantage of the pnc-Si membrane over the polymer membranes is its optical transparency and zero background fluorescence. Therefore currently, a pnc-Si-based system may be the most ideal for interrogating the migratory response time of fast moving cells to the changing flux of cellular activators. In Chapter 2, we demonstrate that a pnc-Si-based thin-membrane system can promote chemotaxis and rapidly label and wash neutrophils in real time without biasing their migration.

1.3 Neutrophil Haptotaxis

Haptotaxis is the directed migration of cells in response to a surface bound gradient of molecular signals or other surface characteristic. While chemotaxis and haptotaxis both have been demonstrated to be possible modes of directional migration, the number of publications on chemotaxis (33642) out-number those on haptotaxis (227) in a ratio of ~150:1 in the of PubMed archive. The observed disparity may be due in part to the widespread use of the Boyden chamber and the relative ease with which chemotaxis can be studied. Currently, it is unclear if the low number of haptotaxis-related publications is due to the lack of interest or the rarity with which haptotaxis has been demonstrated.

Neutrophils encounter numerous surface-presented signals as they migrate about to seek pathogens (Fig. 1.1), and therefore the notion of haptotaxis is appealing. An

immobilized gradient would not be diluted and washed away in the presence of blood flow, and thus should be particularly advantageous for guiding the lateral migration of neutrophils on the vessel wall. While both *in vivo* and *in vitro* observations indicated that neutrophils migrate along the endothelium to sites of transmigration [73], whether or not there exists a specific mechanism that guides the neutrophils to these sites is unknown. Since it has been reported that higher site densities of IL-8 and ICAM-1 correlated with a higher density of neutrophils on functionalized substrates [74] and the vascular endothelium [73], we hypothesized an IL-8- or ICAM-1- mediated haptotaxis to be a possible mechanism.

1.3.1 Evidence for Neutrophil Haptotaxis: C5a, IL-8, and Lectin KM^+

To our knowledge, currently there are only three studies that investigated neutrophil haptotaxis *in vitro*, all of which were conducted using the Boyden chamber transmigration assay. The chemoattractants examined were C5a, IL-8, and lectin KM^+ [75-77].

In these studies, chemoattractants were coated on the microporous membrane of the Boyden chamber through incubation with a gradient. When cell suspension media without chemoattractant was placed on the side of the membrane where neutrophils were to be seeded, and media that contained chemoattractant was placed on the opposite side, the membrane was said to be coated with a positive haptotactic gradient. When this configuration is reversed, the membrane was said to be coated with a negative haptotactic gradient. After coating, the membrane was washed to remove soluble chemoattractant.

Measurements of the transmigration through a membrane incubated with chemoattractants on both sides served as a control for random transmigration (haptokinesis). If the number of transmigrated cells through a coated membrane was significantly higher than the one obtained through the haptokinesis control, the results were interpreted as haptotaxis.

While relatively easy to implement, the use of a Boyden chamber for haptotaxis studies has several drawbacks. Because cell migration cannot be directly visualized in the Boyden chamber, the presence of haptotaxis can only be inferred. Verifying the existence of an immobilized gradient in the membrane is also technically challenging, and often not performed cf.[75-77]. Finally it is difficult to rule out the possibility that small amounts of residual soluble chemoattractant could remain in the microporous membrane after washing, and cause cell migration that is not the result of an immobilized gradient.

With the microporous membranes (~5-22 μm thick) that Rot and Santos-de-Oliveira *et al.* used for IL-8- and lectin KM^+- studies [76, 77], the immobilized gradient spanned no more than 30 μm, only about three times the size of neutrophil (~10 μm). The cell motility data obtained therefore more closely reflect an all-or-nothing transmigration rather than a persistent haptotaxis. In contrast, complete transmigration through the 180 μm-thick microporous membrane used by Webster *et al.* for the C5a study is more convincing [75]. However, the thicker membrane raises a suspicion that there may be more residual chemoattractant in membrane that would create a soluble gradient, thereby confounding interpretation of the migration studies.

To help establish the claim that the transmigration is due to haptotaxis and not

haptokinesis, especially with the use of a thinner membrane, it would be meaningful to perform the haptokinesis controls with membranes that are coated uniformly throughout. While Rot and Santos-de-Oliveira *et al.* did not do so, they did use membranes coated with negative haptotactic gradients as the reference for comparison. Rot showed that the number of cells transmigrated exhibited a parabolic trend with respect to the increase in IL-8 coating concentration, which increased, peaked around the coating concentration of 1.5 μg/mL, and decreased back to a level comparable to the negative haptotaxis reference. In the case of the lectin KM^+ study, the number of cells transmigrated did not exhibit a parabolic trend. Instead, the number of transmigrated cells steeply increased near the incubating concentration of 100 ng/well, and remained about the same even at the higher incubating concentrations.

Another important requirement for claiming that migration is haptotactic is to verify the presence of a coated gradient with imaging techniques. In the C5a study, Webster *et al.* coated the membrane with ^{125}I-labeled C5a and showed through autoradiography that there indeed existed an increase in the number of ^{125}I-C5a grains along a 0.5 μm-thin cutout section of the membrane. Although not specified by Webster et al., it is highly likely that the act of sectioning actually altered the distribution of C5a. For the IL-8 study, Rot did perform an alkaline phosphatase anti-alkaline phosphatase (APAAP) immunocomplex assay to detect the presence of the coated IL-8. The APAAP assay uses IL-8-binding antibodies that are conjugated with enzymes to amplify the presence of IL-8 through the production of colored indicators. However, the APAAP assay cannot demonstrate the presence of a coated gradient through the membrane, and only indicated

that an increase in the IL-8 coating concentration leads to a higher number of coated IL-8 on the surface of the membrane. As for the lectin KM^+ study, the presence of a coated lectin KM^+ gradient was not verified at all.

Since the ultimate confirmation of haptotaxis would require both the direct observation of guided migration and the presence of an immobilized gradient, the aforementioned studies only suggest the existence of C5a-, IL-8-, and lectin KM^+-promoted haptotaxis. In this thesis, we sought to directly visualize directed migration of neutrophils on a verified gradient of immobilized IL-8 to confirm IL-8 haptotaxis. Since adhesion molecules such laminin, fibronectin (Fn), vitronectin, collagen, and RGD (L-arginine-glycine-L-aspartic acid peptide) have all been reported to promote the haptotaxis of different cell types [50, 78-81], we further extended our studies to include the adhesion molecule ICAM-1 in our migration studies.

1.3.2 Soluble and Immobilized Presentation of IL-8 *in vivo*

During sepsis or after the intravenous administration of immune stimulants, the level of soluble IL-8 in blood circulation substantially increases [27, 82-84], with peak concentration ranging from as little as 17 pg/mL to 20 ng/mL [27, 83, 84]. A number of *in situ* binding assays and biochemical studies on IL-8 also suggest that IL-8 can be immobilized on blood vessel walls [85-89]. Surface presentation of IL-8 may be an evolutionary adaptation that confers site-specificity and efficacy: neutrophils are recruited to sites where IL-8 is present, and the immobilized IL-8 does not become diluted due to blood flow.

Most studies that demonstrated the existence of IL-8 immobilization were performed by Dr. Antal Rot. In his 1992 study, Rot injected ^{125}I-radiolabeled IL-8 into human, pig, monkey, rabbit, and rat skin samples and found that as early as 30 min after the injection, most of the radiolabeled IL-8 was found in or near the postcapillary venules, but not in the arteries [86]. However, no IL-8 was found 1 hr after the injection, presumably because by then all the injected IL-8 was already released into the blood stream [86].

The biochemical study of Webb *et al.* demonstrated that IL-8 can bind to heparin-sepharose column, and that the salt concentration required to elute IL-8 substantially decreased for IL-8 with a truncated C-terminus [75]. Subsequent investigations indicated that it is the lysine residues near the C-terminus that enabled the electrostatic attraction of IL-8 to heparin, haparan-sulfate, and glycosaminoglycans (GAGs) [90-93]. Furthermore, *in situ* binding assays showed that the C-terminus truncated IL-8, when injected into skin samples, was found primarily on the abluminal endothelial cell surface, whereas native IL-8 was found mostly on the luminal surface (facing the blood flow) [88, 89]. All these findings are consistent with Dr. Rot's hypothesis that the IL-8 in skin ECM were first internalized by the endothelial cells, then eventually transported to the luminal glycocalyx on the luminal walls to mediate neutrophil activation [87].

While time-lapse immunofluorescence did show that IL-8 is produced, stored, and subsequently secreted from Golgi apparatus and the Golgi-derived Weibel-Palade bodies in endothelial cells [94], it is currently unclear what combination of intracellular, intercellular, and extracellular transport mechanisms shuttle IL-8 through the skin tissue to the luminal glycocalyx. We do know for certain, however, that soluble IL-8 is present

in blood during an acute immune response such as sepsis [27, 82-84], and that IL-8 can electrostatically bind to heparin, heparan-sulfate, and other glycosaminoglycans (GAGs) that are associated with the endothelial glycocalyx [90-93]. It is therefore likely that both the soluble and immobilized presentation of IL-8 does occur *in vivo*.

1.3.3 Higher ICAM-1 correlated with Higher Neutrophil Transmigration

Previous studies have shown that the transmigration of neutrophils out of the gingival sulcus and the vascular endothelium is associated with higher surface presentation of ICAM-1 [74, 95]. The underlying mechanisms, however, have not been specifically investigated. One possible explanation is that there exists a threshold of ICAM-1 density above which the neutrophils transitioned from luminal migration to transmigration. Another explanation is that there are simply more neutrophils at ICAM-1-rich hot spots. This may be a consequence of a flow-assisted adhesion or the haptotaxis of the neutrophil up the ICAM-1 gradient. Since currently there are no studies that specifically examined the presence of haptotaxis on ICAM-1, we included ICAM-1 as a candidate "haptoattractant" in our studies of neutrophil migration.

1.3.4 Potential of Haptotaxis as a Cell Migration Platform

It is worth pointing out that haptotaxis may be used as a platform to help determine if a cellular activator of interest is also an attractant to a specific cell type, much like the use of a Boyden chamber. Alternatively, a haptotaxis platform could also be used to identify different cell types based on their propensities to migrate toward different

chemoattractants. Unlike the flow-based chemotaxis platform where a mechanism of flow generation is required, a haptotaxis platform can be used immediately after cell seeding because the gradients are already preformed on the substrate.

1.4 Thesis Overview

The goal of this thesis is to create systems that enable controlled studies of the environmental parameters that control neutrophil motility. Such systems would help identify the activators and inhibitors of cell spreading, polarization, and migration. In the first approach, flow was used to generate the gradient, and a permeable yet flow-resistive membrane was used to shield the cells from the shear stress (Chapter 2). Such a scenario mimics the migration of neutrophils in the ECM where there is an absence of shear (Fig.1.1v). In addition (Chapter 3), we develop an analytical model and numerical simulations to better assess the level of shear-stress that is present in the membrane-based migration platform. In the second approach, a gradient was pre-coated onto the substrate through prolonged exposure of the substrate to a soluble gradient. On the coated substrate, cell migration commences immediately upon cell seeding, with or without the presence of flow to sustain a gradient. We chose IL-8 and ICAM-1 as the signalling cues of choice to assess the ease with which a directed migration of neutrophils can be induced (Chapter 4). This microenvironment mimics the endothelium that lines the blood vessel wall (Fig.1.1iii). Chapter 5 provides a brief overview and discusses future studies inspired from the findings from Chapters 2, 3, and 4.

1.5 References

1. Bain, B.J. and J.M. England, *Normal haematological values: sex difference in neutrophil count*. British Medical Journal, 1975. **1**(5953): p. 306.
2. Summers, C., et al., *Neutrophil kinetics in health and disease*. Trends in Immunology, 2010. **31**(8): p. 318-324.
3. Janeway, C.A., et al., *Immunobiology*. 2001.
4. Springer, T.A., *Traffic signals for lymphocyte recirculation and leukocyte emigration: the multistep paradigm*. Cell, 1994. **76**(2): p. 301-314.
5. Luster, A.D., R. Alon, and U.H. von Andrian, *Immune cell migration in inflammation: present and future therapeutic targets*. Nature Immunology, 2005. 6(12): p. 1182-1190.
6. Ley, K., et al., *Getting to the site of inflammation: the leukocyte adhesion cascade updated*. Nature Reviews Immunology, 2007. **7**(9): p. 678-689.
7. Wright, H.L., et al., *Neutrophil function in inflammation and inflammatory diseases*. Rheumatology, 2010. **49**(9): p. 1618-1631.
8. Amulic, B., et al., *Neutrophil function: from mechanisms to disease*. Annual Review of Immunology, 2012. **30**: p. 459-489.
9. American College of Chest Physicians, *Definitions for sepsis and organ failure and guidelines for the use of innovative therapies in sepsis*. Critical Care Medicine, 1992. **20**: p. 864-874.
10. Marti-Carvajal, A.J., et al., *Human recombinant protein C for severe sepsis and septic shock in adult and paediatric patients*. Cochrane Database System Review, 2012. **12**.
11. Stone, R., *Search for sepsis drugs goes on despite past failures*. Science, 1994. **264**(5157): p. 365.
12. Martin, G.S., et al., *The epidemiology of sepsis in the United States from 1979 through 2000*. New England Journal of Medicine, 2003. **348**(16): p. 1546-1554.
13. Dinarello, C.A., *Proinflammatory and anti-inflammatory cytokines as mediators in the pathogenesis of septic shock*. CHEST Journal, 1997. **112**(6_Supplement): p. 321S-329S.
14. Cohen, J., *The immunopathogenesis of sepsis*. Nature, 2002. **420**(6917): p. 885-891.
15. Brown, K.A., et al., *Neutrophils in development of multiple organ failure in sepsis*. The Lancet, 2006. **368**(9530): p. 157-169.
16. Elphick, G.F., et al., *Recombinant human activated protein C inhibits integrin-mediated neutrophil migration*. Blood, 2009. **113**(17): p. 4078-4085.
17. Reddy, R.C. and T.J. Standiford, *Effects of sepsis on neutrophil chemotaxis*. Current Opinion in Hematology, 2010. **17**(1): p. 18-24.
18. Kovach, M.A. and T.J. Standiford, *The function of neutrophils in sepsis*. Current Opinion in Infectious Diseases, 2012. **25**(3): p. 321-327.

19. Bernard, G.R., et al., *Efficacy and safety of recombinant human activated protein C for severe sepsis*. New England Journal of Medicine, 2001. **344**(10): p. 699-709.
20. Okuno, T., et al., *Leukotriene B4 receptor and the function of its helix 8.* Journal of Biological Chemistry, 2005. **280**(37): p. 32049-32052.
21. Cattaneo, F., M. Parisi, and R. Ammendola, *Distinct signaling cascades elicited by different formyl Peptide receptor 2 (FPR2) agonists.* International Journal of Molecular Sciences, 2013. **14**(4): p. 7193-7230.
22. Humphries, J.D., A. Byron, and M.J. Humphries, *Integrin ligands at a glance.* Journal of Cell Science, 2006. **119**(19): p. 3901-3903.
23. Barczyk, M., S. Carracedo, and D. Gullberg, *Integrins.* Cell and Tissue Research, 2010. **339**(1): p. 269-280.
24. Bikoue, A., et al., *Quantitative analysis of leukocyte membrane antigen expression on human fetal and cord blood: normal values and changes during development.* Clinical Immunology and Immunopathology, 1997. **84**(1): p. 56-64.
25. Ding, Z.-M., et al., *Relative contribution of LFA-1 and Mac-1 to neutrophil adhesion and migration.* The Journal of Immunology, 1999. **163**(9): p. 5029-5038.
26. Tandon, R., R.I. Sha'afi, and R.S. Thrall, *Neutrophil β2-integrin upregulation is blocked by a p38 MAP kinase inhibitor.* Biochemical and Biophysical Research Communications, 2000. **270**(3): p. 858-862.
27. Nupponen, I., et al., *Neutrophil CD11b expression and circulating interleukin-8 as diagnostic markers for early-onset neonatal sepsis.* Pediatrics, 2001. **108**(1): p. e12-e12.
28. Vedder, N.B. and J.M. Harlan, *Increased surface expression of CD11b/CD18 (Mac-1) is not required for stimulated neutrophil adherence to cultured endothelium.* Journal of Clinical Investigation, 1988. **81**(3): p. 676.
29. Smith, C.W., et al., *Cooperative interactions of LFA-1 and Mac-1 with intercellular adhesion molecule-1 in facilitating adherence and transendothelial migration of human neutrophils in vitro.* Journal of Clinical Investigation, 1989. **83**(6): p. 2008.
30. Henderson, R.B., et al., *The use of lymphocyte function–associated antigen (LFA)-1–deficient mice to determine the role of LFA-1, Mac-1, and α4 integrin in the inflammatory response of neutrophils.* The Journal of Experimental Medicine, 2001. **194**(2): p. 219-226.
31. Dixit, N., et al., *Migrational guidance of neutrophils is mechanotransduced via high-affinity LFA-1 and calcium flux.* The Journal of Immunology, 2011. **187**(1): p. 472-481.
32. Heit, B., P. Colarusso, and P. Kubes, *Fundamentally different roles for LFA-1, Mac-1 and α4-integrin in neutrophil chemotaxis.* Journal of Cell Science, 2005. **118**(22): p. 5205-5220.
33. Lishko, V.K., et al., *Multiple binding sites in fibrinogen for integrin αMβ2 (Mac-1).* Journal of Biological Chemistry, 2004. **279**(43): p. 44897-44906.

34. Sumagin, R., et al., *LFA-1 and Mac-1 define characteristically different intralumenal crawling and emigration patterns for monocytes and neutrophils in situ.* The Journal of Immunology, 2010. **185**(11): p. 7057-7066.
35. Kirveskari, J., Bono, P., Granfors, K., Leirisalo-Repo, M., Jalkanen, S., & Salmi, M. (2000). *Expression of α4-integrins on human neutrophils*. Journal of Leukocyte Biology, 68(2), 243-250.
36. Hughes, B.J., et al., *Recruitment of CD11b/CD18 to the neutrophil surface and adherence-dependent cell locomotion.* Journal of Clinical Investigation, 1992. **90**(5): p. 1687.
37. Seo, S.M., L.V. McIntire, and C.W. Smith, *Effects of IL-8, Gro-α, and LTB4 on the adhesive kinetics of LFA-1 and Mac-1 on human neutrophils.* American Journal of Physiology-Cell Physiology, 2001. **281**(5): p. C1568-C1578.
38. Smith, L.A., et al., *Neutrophil traction stresses are concentrated in the uropod during migration.* Biophysical Journal, 2007. **92**(7): p. L58-L60.
39. Oakes, P.W., et al., *Neutrophil morphology and migration are affected by substrate elasticity.* Blood, 2009. **114**(7): p. 1387-1395.
40. Lin, F., et al., *Effective neutrophil chemotaxis is strongly influenced by mean IL-8 concentration.* Biochemical and Biophysical Research Communications, 2004. **319**(2): p. 576-581.
41. Boyden, S., *The chemotactic effect of mixtures of antibody and antigen on polymorphonuclear leucocytes.* The Journal of Experimental Medicine, 1962. **115**(3): p. 453-466.
42. Toetsch, S., et al., *The evolution of chemotaxis assays from static models to physiologically relevant platforms.* Integrative Biology, 2009. **1**(2): p. 170-181.
43. Keenan, T.M. and A. Folch, *Biomolecular gradients in cell culture systems.* Lab on a Chip, 2008. **8**(1): p. 34-57.
44. Zigmond, S.H., *Ability of polymorphonuclear leukocytes to orient in gradients of chemotactic factors.* The Journal of Cell Biology, 1977. **75**(2): p. 606-616.
45. Zicha, D., G.A. Dunn, and A.F. Brown, *A new direct-viewing chemotaxis chamber.* Journal of Cell Science, 1991. **99**(4): p. 769-775.
46. Nelson, R.D., P.G. Quie, and R.L. Simmons, *Chemotaxis under agarose: a new and simple method for measuring chemotaxis and spontaneous migration of human polymorphonuclear leukocytes and monocytes.* The Journal of Immunology, 1975. **115**(6): p. 1650-1656.
47. Kamholz, A.E., et al., *Quantitative analysis of molecular interaction in a microfluidic channel: the T-sensor.* Analytical Chemistry, 1999. **71**(23): p. 5340-5347.
48. Jeon, N.L., et al., *Generation of solution and surface gradients using microfluidic systems.* Langmuir, 2000. **16**(22): p. 8311-8316.
49. Jeon, N.L., et al., *Neutrophil chemotaxis in linear and complex gradients of interleukin-8 formed in a microfabricated device.* Nature Biotechnology, 2002. **20**(8): p. 826-830.

50. Dertinger, S.K.W., et al., *Gradients of substrate-bound laminin orient axonal specification of neurons.* Proceedings of the National Academy of Sciences, 2002. **99**(20): p. 12542-12547.
51. Chung, B.G., et al., *Human neural stem cell growth and differentiation in a gradient-generating microfluidic device.* Lab on a Chip, 2005. **5**(4): p. 401-406.
52. Wang, C.J., et al., *A microfluidics-based turning assay reveals complex growth cone responses to integrated gradients of substrate-bound ECM molecules and diffusible guidance cues.* Lab on a Chip, 2008. **8**(2): p. 227-237.
53. Malek, A.M., et al., *Fluid shear stress differentially modulates expression of genes encoding basic fibroblast growth factor and platelet-derived growth factor B chain in vascular endothelium.* Journal of Clinical Investigation, 1993. **92**(4): p. 2013.
54. Duan, Y., et al., *Shear stress-induced changes of membrane transporter localization and expression in mouse proximal tubule cells.* Proceedings of the National Academy of Sciences, 2010. **107**(50): p. 21860-21865.
55. Flores, D., et al., *Fluid shear stress induces renal epithelial gene expression through polycystin-2-dependent trafficking of extracellular regulated kinase.* Nephron Physiology, 2010. **117**(4): p. p27-p36.
56. Mitchell, M.J. and M.R. King, *Shear-induced resistance to neutrophil activation via the formyl peptide receptor.* Biophysical Journal, 2012. **102**(8): p. 1804-1814.
57. Simmers, M.B., A.W. Pryor, and B.R. Blackman, *Arterial shear stress regulates endothelial cell-directed migration, polarity, and morphology in confluent monolayers.* American Journal of Physiology-Heart and Circulatory Physiology, 2007. **293**(3): p. H1937-H1946.
58. Hsu, S., et al., *Effects of shear stress on endothelial cell haptotaxis on micropatterned surfaces.* Biochemical and Biophysical Research Communications, 2005. **337**(1): p. 401-409.
59. Rainger, G.E., et al., *Neutrophils sense flow-generated stress and direct their migration through αvβ3-integrin.* American Journal of Physiology-Heart and Circulatory Physiology, 1999. **276**(3): p. H858-H864.
60. Sheikh, S., et al., *Exposure to fluid shear stress modulates the ability of endothelial cells to recruit neutrophils in response to tumor necrosis factor-α: a basis for local variations in vascular sensitivity to inflammation.* Blood, 2003. **102**(8): p. 2828-2834.
61. Valignat, M.-P., et al., *T lymphocytes orient against the direction of fluid flow during LFA-1-mediated migration.* Biophysical Journal, 2013. **104**(2): p. 322-331.
62. Diao, J., et al., *A three-channel microfluidic device for generating static linear gradients and its application to the quantitative analysis of bacterial chemotaxis.* Lab on a Chip, 2006. **6**(3): p. 381-388.
63. Cheng, S.-Y., et al., *A hydrogel-based microfluidic device for the studies of directed cell migration.* Lab on a Chip, 2007. **7**(6): p. 763-769.
64. Shamloo, A., et al., *Endothelial cell polarization and chemotaxis in a microfluidic device.* Lab on a Chip, 2008. **8**(8): p. 1292-1299.

65. Kim, T., M. Pinelis, and M.M. Maharbiz, *Generating steep, shear-free gradients of small molecules for cell culture.* Biomedical Microdevices, 2009. **11**(1): p. 65-73.
66. Bhattacharjee, N., et al., *A neuron-benign microfluidic gradient generator for studying the response of mammalian neurons towards axon guidance factors.* Integrative Biology, 2010. **2**(11-12): p. 669-679.
67. VanDersarl, J.J., A.M. Xu, and N.A. Melosh, *Rapid spatial and temporal controlled signal delivery over large cell culture areas.* Lab on a Chip, 2011. **11**(18): p. 3057-3063.
68. Keenan, T.M., C.-H. Hsu, and A. Folch, *Microfluidic "jets" for generating steady-state gradients of soluble molecules on open surfaces.* Applied Physics Letters, 2006. **89**(11): p. 114103.
69. Taylor, A.M., et al., *Microfluidic multicompartment device for neuroscience research.* Langmuir, 2003. **19**(5): p. 1551-1556.
70. Paliwal, S., et al., *MAPK-mediated bimodal gene expression and adaptive gradient sensing in yeast.* Nature, 2007. **446**(7131): p. 46-51.
71. Li, C.-W., R. Chen, and M. Yang, *Generation of linear and non-linear concentration gradients along microfluidic channel by microtunnel controlled stepwise addition of sample solution.* Lab on a Chip, 2007. **7**(10): p. 1371-1373.
72. Striemer, C.C., et al., *Charge-and size-based separation of macromolecules using ultrathin silicon membranes.* Nature, 2007. **445**(7129): p. 749-753.
73. Sumagin, R. and I.H. Sarelius, *Intercellular adhesion molecule-1 enrichment near tricellular endothelial junctions is preferentially associated with leukocyte transmigration and signals for reorganization of these junctions to accommodate leukocyte passage.* The Journal of Immunology, 2010. **184**(9): p. 5242-5252.
74. DiVietro, J.A., et al., *Immobilized IL-8 triggers progressive activation of neutrophils rolling in vitro on P-selectin and intercellular adhesion molecule-1.* The Journal of Immunology, 2001. **167**(7): p. 4017-4025.
75. Webster, R.O., B. Zanolari, and P.M. Henson, *Neutrophil chemotaxis in response to surface-bound C5a.* Experimental Cell Research, 1980. **129**(1): p. 55-62.
76. Rot, A., *Neutrophil attractant/activation protein-1 (interleukin-8) induces in vitro neutrophil migration by haptotactic mechanism.* European Journal of Immunology, 1993. **23**(1): p. 303-306.
77. Santos-de-Oliveira, R., et al., *A neutrophil migration-inducing lectin from Artocarpus integrifolia.* The Journal of Immunology, 1994. **153**(4): p. 1798-1807.
78. McCarthy, J.B., S.L. Palm, and L.T. Furcht, *Migration by haptotaxis of a Schwann cell tumor line to the basement membrane glycoprotein laminin.* The Journal of Cell Biology, 1983. **97**(3): p. 772-777.
79. Rhoads, D.S. and J.-L. Guan, *Analysis of directional cell migration on defined FN gradients: role of intracellular signaling molecules.* Experimental Cell Research, 2007. **313**(18): p. 3859-3867.
80. Thibault, M.M., C.D. Hoemann, and M.D. Buschmann, *Fibronectin, vitronectin, and collagen I induce chemotaxis and haptotaxis of human and rabbit*

mesenchymal stem cells in a standardized transmembrane assay. Stem Cells and Development, 2007. **16**(3): p. 489-502.
81. Brandley, B.K. and R.L. Schnaar, *Tumor cell haptotaxis on covalently immobilized linear and exponential gradients of a cell adhesion peptide.* Developmental Biology, 1989. **135**(1): p. 74-86.
82. Van Zee, K.J., et al., *IL-8 in septic shock, endotoxemia, and after IL-1 administration.* The Journal of Immunology, 1991. **146**(10): p. 3478-3482.
83. Martich, G.D., et al., *Detection of interleukin 8 and tumor necrosis factor in normal humans after intravenous endotoxin: the effect of antiinflammatory agents.* The Journal of Experimental Medicine, 1991. **173**(4): p. 1021-1024.
84. DeForge, L.E., et al., *Biphasic production of IL-8 in lipopolysaccharide (LPS)-stimulated human whole blood. Separation of LPS-and cytokine-stimulated components using anti-tumor necrosis factor and anti-IL-1 antibodies.* The Journal of Immunology, 1992. **148**(7): p. 2133-2141.
85. Ferguson, S.S.G., et al., *Molecular mechanisms of G protein-coupled receptor desensitization and resensitization.* Life Sciences, 1998. **62**(17): p. 1561-1565.
86. Rot, A., *Binding of neutrophil attractant/activation protein-1 (interleukin 8) to resident dermal cells.* Cytokine, 1992. **4**(5): p. 347-352.
87. Rot, A., *Endothelial cell binding of NAP-1/IL-8: role in neutrophil emigration.* Immunology Today, 1992. **13**(8): p. 291-294.
88. Middleton, J., et al., *Transcytosis and surface presentation of IL-8 by venular endothelial cells.* Cell, 1997. **91**(3): p. 385-395.
89. Rot, A., et al., *Some aspects of IL-8 pathophysiology. III: Chemokine interaction with endothelial cells.* Journal of Leukocyte Biology, 1996. **59**(1): p. 39-44.
90. Webb, L., et al., *Binding to heparan sulfate or heparin enhances neutrophil responses to interleukin 8.* Proceedings of the National Academy of Sciences, 1993. **90**(15): p. 7158-7162.
91. Witt, D.P. and A.D. Lander, *Differential binding of chemokines to glycosaminoglycan subpopulations.* Current Biology, 1994. **4**(5): p. 394-400.
92. Kuschert, G.S.V., et al., *Identification of a glycosaminoglycan binding surface on human interleukin-8.* Biochemistry, 1998. **37**(32): p. 11193-11201.
93. Möbius, K., et al., *Investigation of lysine side chain interactions of interleukin-8 with heparin and other glycosaminoglycans studied by a methylation-NMR approach.* Glycobiology, 2013. **23**(11): p. 1260-1269.
94. Wolff, B., et al., *Endothelial cell "memory" of inflammatory stimulation: human venular endothelial cells store interleukin 8 in Weibel-Palade bodies.* The Journal of Experimental Medicine, 1998. **188**(9): p. 1757-1762.
95. Tonetti, M.S., M.A. Imboden, and N.P. Lang, *Neutrophil Migration Into the Gingival Sulcus Is Associated With Transepithelial Gradients of Interleukin-8 and ICAM-1*.* Journal of Periodontology, 1998. **69**(10): p. 1139-1147.

Chapter 2
Shear-Free Chemotaxis[†]

2.1 Abstract

Microfluidic systems are powerful tools for cell studies because they enable the precise addition and removal of solutes to control a microenvironment. However, the fluid forces inherent in the use of microfluidics for cell studies are sometimes undesirable. An important example is chemotaxis systems where fluid flow creates well-defined and steady chemotactic gradients but also pushes cells downstream. Here we demonstrate a chemotaxis system in which two compartments are separated by a molecularly thin (15 nm), transparent, and nanoporous silicon membrane. One compartment is a microfluidic channel that carries a flow-generated gradient, while the other compartment is a shear-free environment for cell observation. The thin membranes provide effectively no resistance to molecular diffusion between the two compartments, making them ideal elements for creating flow-free compartments in microfluidic systems. We show that the membranes maintained pure diffusion of nanoparticles in the cell

[†] Adapted from H.H. Chung, C.K. Chan, T.S. Khire, G.A. Marsh, A. Clark Jr., R.E. Waugh, and J.L. McGrath. (2014) "Highly permeable silicon membranes for shear free chemotaxis and rapid cell labeling", *Lab Chip*, **14**, 2456-2468.

compartment despite high input flow (45 mm/min) in the flow compartment only 15 nm away. Using total internal reflection fluorescence (TIRF) microscopy, we show that a flow-generated molecular gradient will pass through the membrane into the quiescent cell compartment. Finally, we demonstrate that our device allows us to expose migrating neutrophils to a chemotactic gradient or fluorescent label without influence from flow.

2.2 Introduction

Cells exhibit many responses to fluid shear stress, including gene regulation [1-3], protein production and trafficking [2, 3], surface receptor presentation [4], morphology changes [1, 5], growth [5, 6], and migration [7-9]. Devices that control the magnitude of shear stress in cell cultures date back three decades and have been instrumental in elucidating physiological responses to shear [10]. Fluid forces can also be unwanted in cell studies when they confound the interpretation of responses to other cellular activators or because they simply push loosely bound cells out of a region of observation. An example where shear stress confounds measurement of cell behavior is in chemotaxis systems that use fluid flow to establish steady gradients of chemoattractants. In these systems, cells experience both the lateral push of fluid flow and the orthogonal influence of a chemical gradient, and consequently crawl diagonally in the field of observation [11, 12]. We correct this problem with a microfluidic system that employs a transparent and highly permeable silicon nanomembrane that allows solutes to be rapidly delivered to cells while reducing shear stress by five orders of magnitude.

Classical chemotaxis systems include the under-agarose migration assay [13] and the Boyden [14], Zigmond [15], and Dunn [16] chambers. Since these devices rely on the passive diffusion of molecules from a source to generate gradients, it is impossible to actively control the formed gradient. Inadvertent convection, such as from evaporation or during the addition of reagents and cells, cannot be rectified [17]. Consequently, these diffusion-based systems offer poor gradient reproducibility.

Later systems by Jeon et al. and Kamholz et al. combine flow streams with different concentration of chemotactic factors to establish gradients [11, 18]. Since the fluid flow continuously supplies and takes away chemotactic factors, a time-invariant concentration profile can be maintained in space. These systems also allow real time control over the concentration profiles to investigate transient cell responses. However, because the cells in these devices are placed directly in the flow channel, they are pushed downstream at the same time as they crawl across the channel in response to the gradient. A simple strategy to decrease the shear stress seen by the cells is to make the cell compartment as a depression in floor of the flow channel [19]. The shear reduction achieved this way, however, is limited because of direct fluid coupling.

Thus in recent years, a number of "shear-free" chemotaxis systems have been developed that maintain steady, well-defined gradients while isolating the cell compartment from the flow in microfluidic channels [20-22]. The general strategy is to incorporate flow resistive elements between flow channels and cell compartments that still permit the exchange of chemotactic factors *via* diffusion. One popular example is the three-compartment system, in which two flanking compartments serve as a source and a

sink to establish a gradient of chemotactic factor across the middle compartment where the cells are located [20-22]. Since the cell compartment must be sufficiently wide (~1 mm) for a meaningful cell observation, ~30 min or more is required to establish a gradient *via* diffusion. The three-compartment system therefore cannot be used to efficiently examine the turning and the repolarization of fast migrating cells in response to the changes in gradient characteristic. The microjet system of Keenan et al., which also consists of three compartments, can establish a gradient in the middle cell compartment within 4 minutes through fast mixing of jets emitted from the source and the sink channel [23-25]. However, in this system cells near the jet output are temporarily exposed to shear stress as high as 0.7 dyn/cm^2.

Recent systems developed by Kim et al. and VanDersarl et al. use polymer membranes (~10-24 μm thick) to separate the flow and the cell compartment [26, 27], both of which are aligned along the imaging axis of an upright microscope. In this way, the rapidly formed lateral gradients only have to diffuse a short distance vertically through the membrane to the cell compartment. The time to establish a chemical equilibrium between the flow and the cell compartment is a function of the membrane thickness and permeability [27], and is generally within 5 min. Ideally, these membranes must be optically transparent to allow high fidelity imaging, and must also be sufficiently thin and porous to allow fast propagation of gradients to the cells by diffusion. The polymer membranes used, however, are optically opaque and tend to confer high background fluorescence.

Here we describe the use of a porous nanocrystalline silicon (pnc-Si) membrane for

shear-free chemotaxis studies. In contrast to the polymer membrane previously used [26, 27], the pnc-Si membrane is optically transparent, three orders of magnitude thinner (15nm), and ten-fold more porous.

These membranes are so highly permeable that they offer effectively no resistance to the diffusion of molecules significantly smaller than their pore sizes (~30 nm) [28, 29]. The combination of dramatic shear reduction with no diffusive resistance makes the membranes ideal for rapid but shear-free delivery of solutes to cells. The membranes also have excellent optical properties for phase and fluorescence microscopy [30].

2.3 Materials and Methods

2.3.1 Silicon Nanomembranes

The fabrication of ultrathin porous nano-crystalline silicon membranes (pnc-Si) has been described previously [31-33]. For the current work, membranes were manufactured on 300 μm thick silicon wafers, in a 13 mm by 31 mm chip format. The membranes were freestanding over a rectangular area of 450 μm by 4 mm, with a thickness of 15 nm, average pore diameter of 30 nm, and a porosity of 10%. A 120 nm thick silicon nitride (SiN) scaffold was overlaid onto the pnc-Si membrane to enhance its mechanical strength, as previously described [34]. The scaffold openings were either tessellated hexagons or circles arranged in hexagonal close packing. For hexagonal openings, each of the six sides measured 62.5 μm and the encasing SiN frame measured 8.5 μm wide (Fig. 2.1). For the circular openings, both the diameter and the edge-to-edge distance

between pores measured 3 μm.

2.3.2 Device Assembly

The chemotaxis system consisted of three main components: 1) the flow compartment, 2) a pnc-Si/SiN hybrid membrane, and 3) the cell compartment (Fig. 2.1). The flow compartment (Fig. 2.1a) is covalently bonded to the membrane (Fig. 2.1b) using ultraviolet-ozone treatment, while the attachment of the flow chamber/hybrid membrane complex to the cell compartment (Fig. 2.1c) is reversible through a simple conformal contact. The flow compartment, which is also the gradient generator in our system [11], is made with Sylgard 184 PDMS (Dow Corning, Midland, MI) patterned and cured on a custom-ordered SU-8 mold with a feature height of 50 μm (Stanford Microfluidics Foundry, Stanford, CA). Holes for the inlets and outlets were punched into the cured PDMS using a blunt 20-gauge needle (Small Parts Inc., Logansport, IN). The cell compartment is made from a 100 μm thick silicone gasket custom-cut using the Silhouette CAMEO cutter (Silhouette America, Oren, UT). The gasket, which forms the walls of the cell compartment, is covalently bonded via ultraviolet-ozone treatment to either a glass slide or a coverslip, which forms the floor of the cell compartment. Two additional openings were patterned into the chip and aligned with glass microcapillaries (ID/OD 500 μm /900 μm; Friedrich & Dimmock, Inc., Millville, NJ) that serve as adaptors for tubing to bring fluid into and out of the cell compartment (Fig. 2.1). Tygon tubing with ID/OD of 1/32" / 3/32" (Saint-Gobain Performance Plastics Corporation) was used to connect the microcapillaries to syringe pump (NE-1800; New Era Pump Systems,

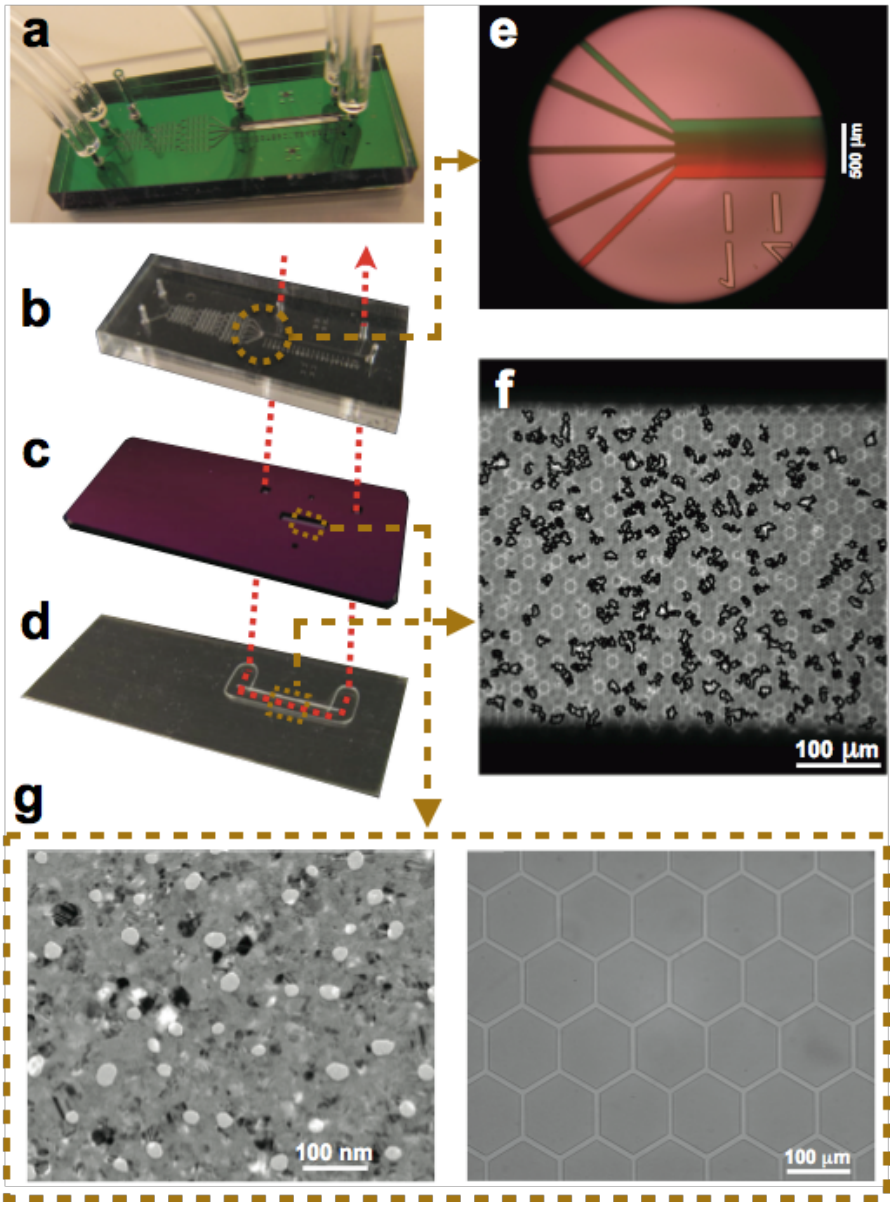

Figure 2.1: Shear-free Chemotaxis Chamber. a. The assembled system (width × height ~1.3 cm × 3.1 cm.). **b.** The flow compartment, which is also a gradient generator. **c.** The hybrid membrane chip. **d.** The silicone gasket that forms the cell compartment. The red dashed arrow passing through (b), (c), and (d) indicates the flow path for cell seeding. **e.** Magnified view of the gradient generator, featuring the five microchannels that converge the flow to form a gradient. **f.** Magnified view featuring migrating human neutrophils in the cell compartment, with cell edges enhanced for cell tracking. **g.** Magnified views featuring the pnc-Si membrane (left) and the SiN scaffold (right). The SiN scaffold in this case is a honeycomb. The white objects in the pnc-Si are the nanopores and the black objects are silicon nanocrystals.

Inc., Farmingdale, NY].

2.3.1 Nanoparticle Tracking

We used particle tracking [35] of green fluorescent polystyrene particles (210 nm; Bangs Laboratories, Inc., Fisher, IN) to measure cross-flow between the cell and flow compartment. To obtain reference motions, we first forced fluid through the cell compartment at fixed rates of 0.1 or 0.5 μL/min (v_{avg} ~720 or ~3600 μm/min, respectively). The flow was then stopped completely with all access fluid ports closed, and the thermal motions of the particles were tracked. Flow rates of 10, 50, and 100 μL/min were then applied to the flow compartment (v_{avg} of ~45, 225, and 450 mm/min, respectively) and the motions of the nanoparticles were again tracked. The nanoparticle motion was recorded at 10 frames per min (10 fpm) in an epifluorescence microscope at a total magnification of 200X. The average speed of each nanoparticle was obtained by dividing the total path length traveled by the respective duration of tracking. We defined the system to be shear-free if the average speed of the nanoparticles is not statistically different from zero under the two-tailed student's *T*-test at the alpha level of 0.05. We also performed an analysis where we assume the nanoparticle motion to be a combination of both convection and diffusion. For each nanoparticle, we performed a linear regression on the x- and the y- coordinates with respect to time to obtain the underlying convection. We then subtracted the convection component in each direction from the particle positions and calculated the mean squared displacements (MSDs). The MSDs were then used to calculate the diffusion coefficients of each particle [106]. By this method, we

defined the system to be shear-free when the average speed of the nanoparticles was not statistically significantly different from zero under the two-tailed student's *T*-test at an alpha level of 0.05.

2.3.2 Total Internal Reflection (TIRF) Microscopy

We used TIRF microscopy [36], a technique that specifically excites fluorescent molecules within ~140 nm of a substrate surface, to confirm that the molecular gradient generated in the flow compartment propagates through the membrane and preserves its linear profile near the floor of the cell compartment. The fluorescent gradient was generated by flowing 2 μM of fluorescein isothiocyanate (FITC) against phosphate-buffered saline (PBS) in the gradient mixing segment of the flow compartment. Each solution was pushed at a flow rate of 0.25 μL/min. TIRF was performed under a Nikon TE2000 microscope with an argon-ion illumination laser and a 100X oil objective (NA 1.45). At the end of the TIRF experiment, we used the fluorescence of 0 or 2 μM FITC in the cell compartment as reference values to calibrate measured fluorescence to interpolated concentrations.

2.3.3 Demonstration of Shear-free Chemotaxis and Cell Labeling

Primary human neutrophils were isolated from whole blood by density separation over a solution of 1-Step™ Polymorph (Accurate Chemical & Scientific Co., Westbury, NY), then washed and stored in pH 7.4 HBSS−− buffer, made with calcium- and magnesium-free Hank's balanced salt solution (Gibco, Grand Island, NY) supplemented with 10 mM

HEPES (Sigma-Aldrich, St. Louis, MO) for extra pH buffering and 4% volume ratio of heat-inactivated fetal calf serum (FCS) to prevent non-specific adhesion of neutrophils to container walls. Thereafter, and throughout migration experiments, neutrophils were suspended in pH 7.4 HBSS++ (HBSS buffer supplemented with the calcium (1.26 mM) and the magnesium (0.9 mM) needed for facilitating activation and integrin-mediated adhesion). The channel walls of the entire microfluidic system were incubation-coated with 2 mg/mL bovine serum albumin (BSA) (CalBiochem, La Jolla, CA), a known adhesion molecule that allows Mac-1 integrin ($\alpha_M\beta_2$) binding during cell migration. After washing the BSA off with HBSS++, cells were introduced into the cell compartment at a flow rate of 50 μL/min. Once a significant number of neutrophils were observed under the hybrid membrane, the flow was stopped and the neutrophils were allowed to adhere to the BSA-coated substrate. To create the chemoattractant gradient to direct neutrophil migration, the bacterial peptide N-formylmethionine-leucyl-phenylalanine (fMLP) and pure HBSS++ buffer were each injected with a syringe into the flow compartment at a flow rate of 0.25 μL/min (Fig. 2.1a & Fig. 2.1e). Prior to the injection, the hydrophobic fMLP was solubilized with DMSO (dimethyl sulfoxide) into PBS in the volume ratio of 0.01%, then further diluted to 40 nM in HBSS++. After the chemotaxis experiment, we labeled the neutrophils with a fluorescent gradient by perfusing 1 mM of rhodamine 6 G (R6G) through the flow compartment instead of fMLP.

2.3.4 Measurement and Analysis of Cell Migration

Cell migration was recorded at 4 frames per minute (4 fpm) under a phase contrast microscope at a total magnification of 200X. Most cells were tracked automatically but occasionally with a custom-written MATLAB program (MathWorks, Inc., Natick, MA). All cells that traveled for less than 12 frames (3 min) and less than 30 μm in displacement (~3 cell body lengths) were considered inactive and excluded from the analysis. Inactive cells generally accounted for less than 5% of the total population. Each data set consisted of all the cells tracked in a microscopic field of view (~150-400 cells depending on the seeding). The starting and the ending positions of a cell trajectory were used to define the migration direction vector. The polar plane (see Fig. 2.4) was divided into twelve sectors, with spans of 30°. The migration direction vectors falling within each sector were counted to determine the general directionality of the whole population. To illustrate how the presence of flow can influence cell migration, control experiments were performed with cells in the flow compartment, with or without the 0.5 μL/min input flow, with the cells exposed to either 10 nM of uniformly distributed fMLP or a linear fMLP gradient that ramped from 0 to 40 nM over a 450 μm span. In these control experiments, the flow-based chemotaxis chamber that generates the gradient was bonded to glass instead of the hybrid membrane chip. The inner walls of the entire system were also coated with BSA as in the case of the shear-free chemotaxis system. The 0.5 μL/min input flow was chosen to generate a corresponding wall shear stress of 0.4 dyn/cm^2, a value at the low end of the physiological range and used by other investigators in their chemotaxis studies with neutrophils [9, 11, 12, 37-41].

2.4 Results and Discussion

2.4.1 Nanoparticle Tracking in the Cell Compartment

To test the membrane's ability to create a shear-free microenvironment, we tracked the motion of nanoparticles (210 nm) in the cell compartment over 3 minutes with different flow rates in the flow and the cell compartment (Fig. 2.2). As reference conditions, we examined the motion of nanoparticles with no flow in the system and with 0.1 μL/min applied directly to the cell compartment (v_{avg} of ~720 μm/min). The first reference condition resulted in purely diffusive motion (Fig. 2.2a). The second reference condition produced ballistic particle trajectories and an average particle velocity of 588 μm/min (Fig. 2.2b). When a flow rate of 10 μL/min is applied to the flow compartment (v_{avg} of ~45 mm/min), nanoparticle motions in the cell compartment are purely diffusive (Fig. 2.2c). At 50 μL/min (v_{avg} of ~225 mm/min), a slow drift of the nanoparticles in the cell compartment could be detected (~13 μm/min). Increasing the flow rate in the flow compartment to 100 μL/min (v_{avg} ~450 mm/min) resulted in more obvious convection (Fig. 2.2d) and a measured particle velocity of 19 μm/min. Note that the particle velocity under these conditions was ~30-fold lower than the convection reference case (flow of 0.1 μL/min in the cell compartment), despite the fact that the input flow rate was 1000-fold higher.

The particle tracking experiments suggest that an input flow rate of 50 μL/min is an upper threshold for the maintenance of shear-free conditions. This result is supported by a simple analysis of the excursion expected for diffusive vs. convective nanoparticles in

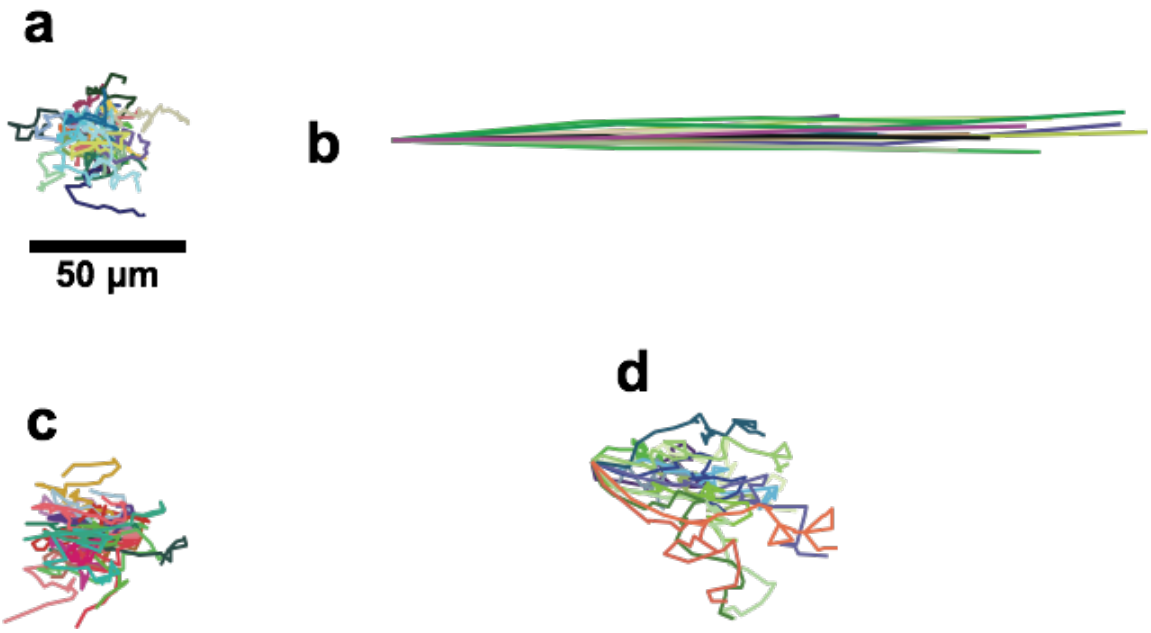

Figure 2.2: Nanoparticle tracking demonstrating shear-free conditions. Particles with diameter of 210 nm were tracked at the mid-height of the cell compartment at the center of the membrane where the flow velocity is the highest. **a.** Particles tracked in the absence of any system flow. **b.** Particles tracked with a flow rate of 0.10 µL/min applied directly to the cell compartment as a reference for convection. **c.** Particles tracked with 10 µL/min in the flow compartment. **d.** With the flow input increased to 100 µL/min, particle drift was observed. Particles were tracked for 3 min except for case (b), where the particles were tracked for 2.5 sec.

our system. The Stokes-Einstein equation gives a theoretical diffusion coefficient D = 124 µm/min for a 210 nm particle in water. Experimentally, we determined a similar value for D (107 µm^2/min) using a mean-square-displacement analysis of nanoparticle trajectories in the 10 µL/min flow case. Employing the theoretical value of 124 µm^2/min, the excursion expected for a purely diffusive particle in T = 3 minutes of observation is:

$$L_d = \sqrt{4DT} = 38\ \mu m$$

Thus a particle requires a drift velocity exceeding L_d/T = 13 µm/min for convective

motion to be comparable to simple Brownian motion during the tracking experiment. Since this value aligns with the 13 μm/min drift detected in the 50 μL/min, we conclude that input flows less than 50 μL/min give "shear-free" conditions in the cell compartment.

Although there have been several prior attempts to create microfluidic systems with 'shear-free' compartments [19-23, 26, 27], none have defined 'shear-free' conditions, nor have they measured the degree of fluidic coupling with the flow compartment to show that they meet the definition. Here we define a 'shear-free' environment to be one where the Brownian motion of a 210 nm particle in the cell compartment is equal or greater than any measurable convection during 3 minutes of observation. It is necessary to create such a particular definition because there will always be some fluidic coupling between the compartments. The practical questions are what is measurable and what is tolerable. In our case, with longer observation times or larger particles, convective motion could likely be detected at 50 μL/min over 3 minutes of observation. For the purpose of delivering solutes to crawling neutrophils however, the criterion we put forth is highly conservative. Even if these experiments were conducted with an input flow rate of 50 μL/min, the shear stress experience by neutrophils in the cell compartment would be less than 4×10^{-5} dyn/cm^2 (4×10^{-6} Pa). The levels of wall shear stress that are known to bias neutrophil migration in conventional microfluidic assays [9, 11, 12, 37-41] are 5 orders higher than this value (0.4 dyn/cm^2).

While a high flow rate is desirable for the rapid delivery of solutes, the rate of solute arrival to the cell compartment also depends on the diffusion time across the membrane.

Therefore the ideal membrane for creating shear-free compartments is one that offers a high resistance to transmembrane fluid flow, but a low resistance to transmembrane diffusion. The ultrathin membranes used here have a negligible transmembrane resistance to the diffusion of molecules smaller than ~30% of the pore size [28, 29]. The high fluid resistance for these membranes derives primarily from the low average pore size of the pnc-Si membrane (~30 nm) and takes advantage of the 3rd order dependence of fluid resistance on pore radius (for a thin membrane where the pore radius and thickness are comparable), as indicated by the Dagan equation (Eqn 3.3.12 of Chapter 3) [42]. By contrast, the polymer membranes used by others have 10× larger pore sizes, 100× larger thicknesses, and a 10× lower porosity [26, 27]. Increasing thickness and lowering porosity increase fluid and diffusive resistances to the same degree. Only by employing an ultrathin membrane can the fluidic resistance be increased through smaller pore sizes without simultaneously increasing the diffusive resistance. To illustrate, the diffusion times for a ~1 nm molecule to transit the membrane will be < 10 μs for our ultrathin membranes compared to ~60s for the membranes used by VanDersarl et al. (thickness = 24 μm; porosity = 0.44%; pore diameter = 750 nm), while the hydraulic resistances of these membranes are of the same order.

2.4.2 TIRF Visualization of Gradient in the Cell Compartment

We used TIRF microscopy to demonstrate that a chemical gradient can be transferred from the flow compartment to the cell compartment (Fig. 2.3). Running FITC dye against PBS buffer in the gradient generator, we created a steady linear gradient over the

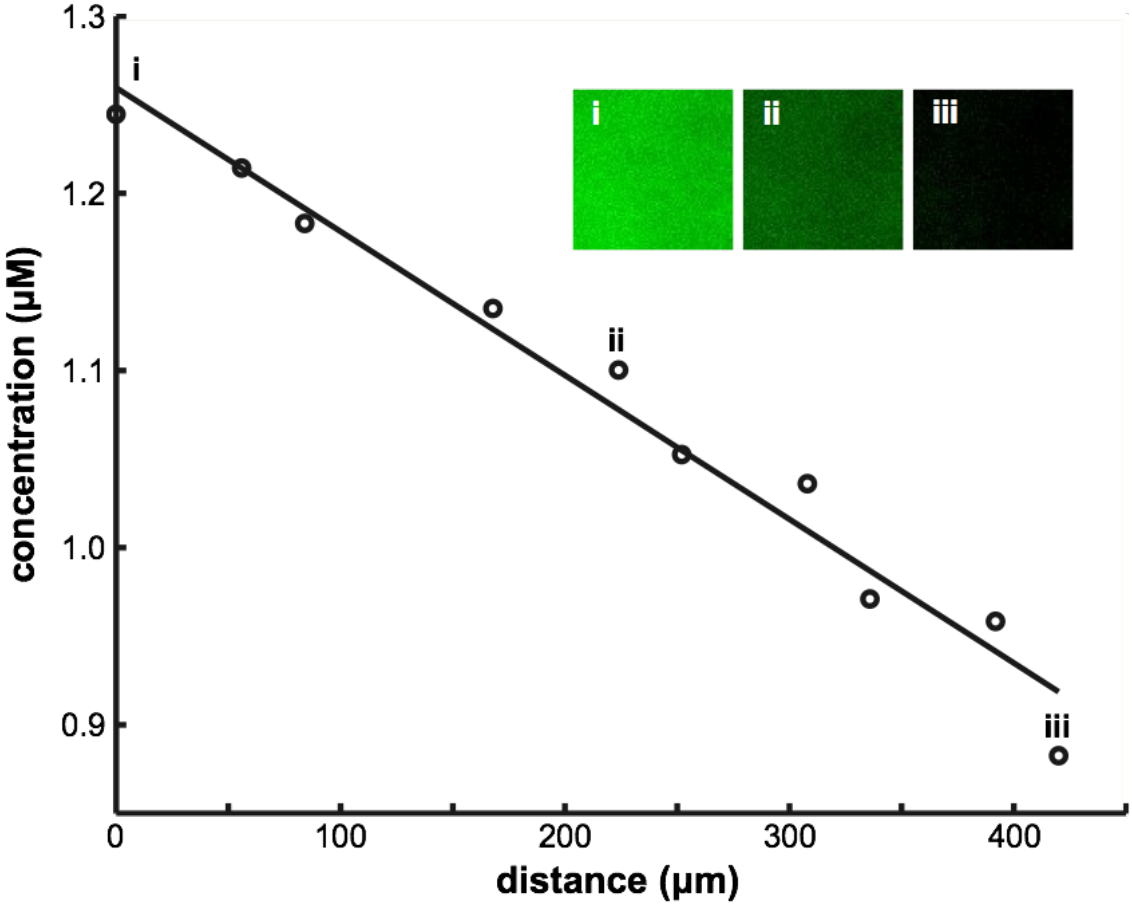

Figure 2.3: Total internal reflection fluorescence (TIRF) microscopy of a gradient at the cell compartment surface. A gradient of FITC dye (0 μM - 2 μM) was visualized via TIRF to ensure that the gradient reaches the bottom of the cell compartment. At the high magnification required by TIRF microscopy, it is necessary to take sequential TIRF images at regular spacings to evaluate the gradient. The insets show images taken at ~50 μm (i), ~225 μm (ii), and, ~425 μm (iii) away from the edge of the membrane with the higher FITC concentration.

membrane in the flow compartment. Using TIRF microscopy, we imaged the bottom ~0.2 μm of the cell compartment (below the center of the membrane) and confirmed the presence of a linear gradient. Across the 450 μm width of the membrane, a normalized

concentration difference of ~27% is observed, with a peak concentration at ~60% of the input FITC concentration (Fig. 2.3). The decrease in both the steepness and the peak concentration of the linear gradient is consistent with Monte Carlo simulation of pure diffusion and indicates that lateral diffusion in the flow compartment and cell compartment tends to homogenize the sample before it reaches the bottom of the cell compartment. At the beginning section of the cell compartment (closer to the merging flow streams that form the gradient), a much steeper gradient would be observed.

2.4.3. Shear-free Chemotaxis and Labeling of Cells

To demonstrate the utility of the membrane-integrated system, we tracked the movement of neutrophils in response to a chemotactic gradient of fMLP. This experiment was selected because the flow required to generate the chemotactic gradient in the flow-based systems [11, 18] has been seen to bias neutrophil migration in the direction of flow (at shear stress as low as 0.23, 0.6, and 1.2 dyn/cm^2) [11, 12, 41]. In control experiments with uniform fMLP and no flow, a similar percentage of cells migrated into each sector of a radial plot indicating random migration (Fig. 2.4a). With the addition of flow but a uniform distribution of fMLP (0.50 μL/min, wall shear stress ~0.4 dyn/cm^2), cell trajectories were clearly biased toward the flow direction (Fig. 2.4b). Consistent with prior work, flow and chemotaxis both influenced cell migration in a system without a membrane to buffer shear (Fig. 2.4c). The same conditions in the membrane-based system however, resulted in ~80% of ~400 tracked cells migrating directionally toward

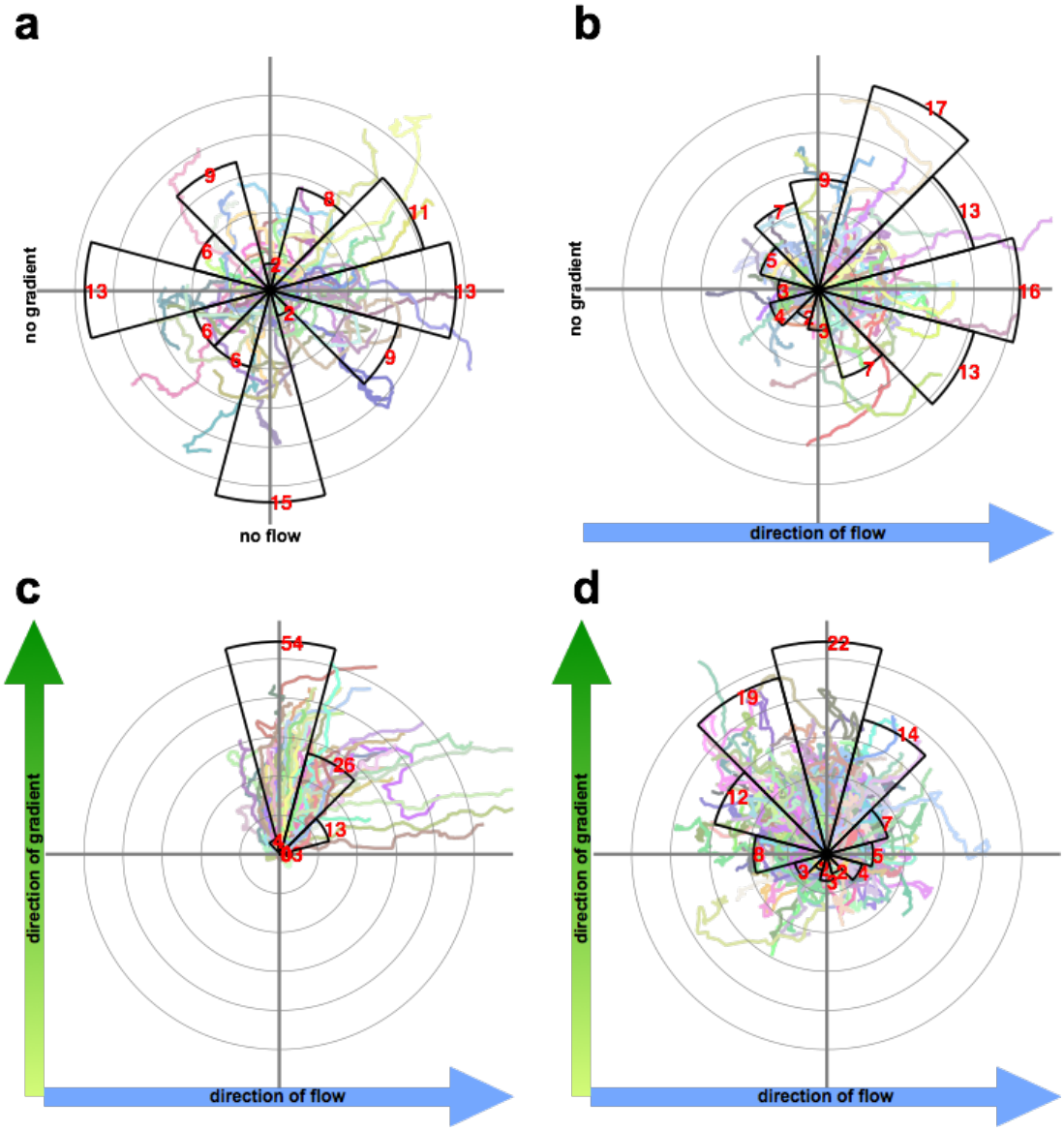

Figure 2.4: Radial histograms of neutrophil migration. Each sector spans 30°, and the distance between each pair of successive concentric rings is 50 μm. The red number and the length span of each sector represent the percentage of cells (n > 150) that migrated into each sector. Superimposed on the radial histogram are the actual trajectories of the migrating neutrophils, each with the starting position centered at the origin of the radial histogram. **a.** Uniform fMLP (10 nM) stimulation and no flow; **b.** Uniform fMLP (10 nM) stimulation with left-to-right flow; **c.** System without membrane, bottom-to-top fMLP gradient (0 nM – 40 nM over 450 μm), and left-to-right flow. Downstream bias of cell migration is evident. **d.** System with membrane, bottom-to-top fMLP gradient (0 nM – 40 nM over 450 μm), and left-to-right flow. In (b), (c), and (d), an input flow rate of 0.50 μL/min was used.

the higher fMLP concentration without any detectable bias in the flow direction (Fig. 2.4d). Despite being biased downstream, cells appear more persistent in the presence of shear (Fig. 2.4c) than in the shear free system (Fig. 2.4d). We suspect that the lower persistence is caused by the shallower chemotactic gradient in the cell compartment of the shear-free system.

To illustrate the use of our shear-free device for fluorescent labeling, we replaced the fMLP gradient with the fluorescent molecule rhodamine 6G (R6G) at the conclusion of a migration study. R6G is a general stain of cell membranes. After maintaining a gradient of R6G for several minutes, we flushed the system with HBSS++ to reveal the labeled cells. As a result of prolonged exposure to the R6G gradient, most cells, especially those situated at the top portion of the cell compartment where the R6G concentrations were higher, were saturated with R6G labeling (Fig. 2.5a). Most importantly, the cell positions appeared undisturbed by the labeling and washing flows of 20 μL/min.

Measuring the fluorescence at the midspan of the cell compartment during this experiment established that the time scale required to form a steady concentration at the membrane is less than 5 minutes at 20 μL/min (Fig. 2.5b), a time scale on par with the 4-6 min response times by Keenan et al., Wang et al., and VanDesarl et al. in their gradient generators [19, 23, 37]. While 5 minutes is a short time to establish a steady gradient compared to traditional chemotaxis systems, much faster times are needed to understand the fastest temporal response of cells to activating solutes. To improve on the temporal response of these systems it is important to recognize that the majority of the 5 minute response was attributed to fluid transport time through the inlet tubing, the mixer, and the

upstream sections of the flow compartment. Additional device miniaturization and control from on-chip chemical reservoirs [19], in-line micropumps [43], pneumatic valves [44], and voltage gated membranes [45] would allow chemical microenvironments to be changed in seconds rather than minutes and would take full advantage of the rapid diffusion enabled by ultrathin silicon nanomembranes.

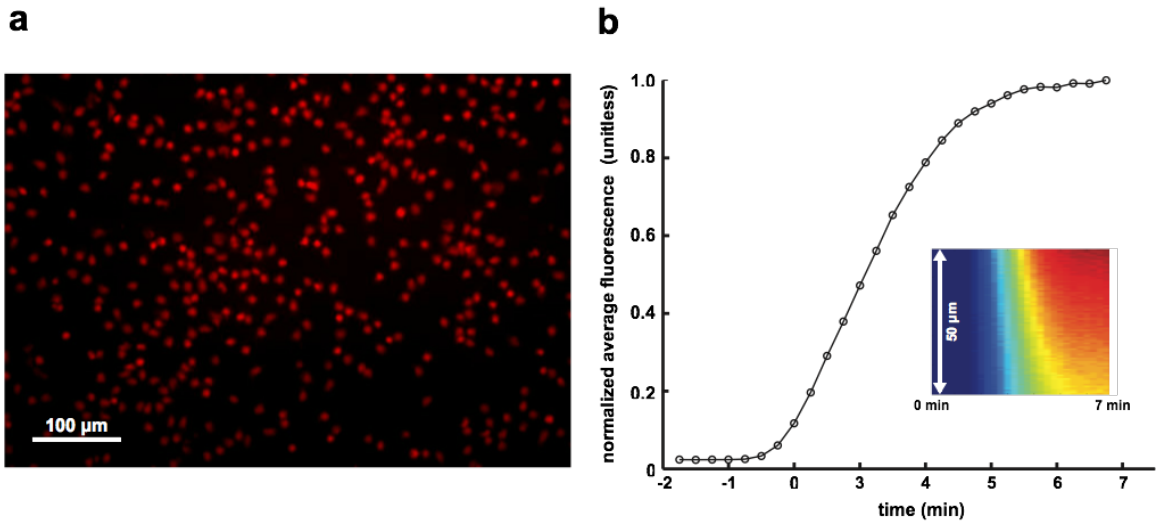

Figure 2.5: Rapid labeling of cells in the absence of flow. a. Image of cells labeled after exposure to a rhodamine gradient. Most cells were saturated with the rhodamine labeling after prolonged exposure, especially those on the top region of the cell compartment where the rhodamine concentrations were higher. **b.** Response time of gradient establishment. Line-scans of fluorescence intensity over a 50 µm span were monitored over a duration of 7 min, starting from the onset of the flow to establish the gradient (kymograph inset). The average intensity of each line-scan was calculated and normalized by that of the 7 min time point and plotted against time. As expected, a steep increase was seen within 2 min, corresponding to the transit time of a 20 µL/min flow through the inlet tubing with inner volume of ~50 µL. The subsequent plateau in fluorescence suggests a system response time of ~3 min for the establishment of a steady state gradient.

2.5 Summary and Conclusions

While microfluidics devices are powerful tools for the culture and study of cells, fluid forces can cause unwanted cellular responses or simply wash cells out of regions of observation or culture. Shear-free microfluidic systems allow efficient handling of cells while eliminating these complications of fluid flow. The fastest responding shear-free systems use a porous membrane to protect cells from high shear forces in an adjacent flow chamber. Here we contribute to the design of these systems by introducing porous nanocrystalline silicon (pnc-Si) as an ideal membrane for shear-free microfluidics. Ultrathin (15 nm) pnc-Si membranes are ideal because of their transparency and their extraordinary permeability to the diffusion of small molecules despite attenuating fluid forces by 5 orders-of-magnitude. We are the first to quantify shear reduction in a shear-free microfluidic system. Using highly sensitive nanoparticle tracking, we show that nanoparticles remain purely diffusive in the cell compartment with input flow rates as high as 50 μL/min (v_{avg} of ~225 mm/min) in the flow compartment.

We employ our shear reduction system in combination with a rapid gradient mixer to create an improved chemotaxis chamber for use with shear-sensitive cells. We demonstrate the successful passage of a chemical gradient from the flow compartment to the floor of the cell compartment where neutrophils are seeded. We use neutrophils because their migration is known to be biased by flow in microfluidic systems that do not employ shear reduction. We demonstrate that this bias is completely eliminated in our device so that neutrophils migration is determined only by a chemoatractant gradient. While ultrathin membranes should enable excellent temporal resolution for studying

transient cell responses such as cell activation or re-polarization to suddenly introduced soluble factors, a highly permeable membrane is only one component needed for a fast-responding shear-free system. Currenty the large fluidic paths and resevoirs in our microfluidic system are rate limiting. Advanced systems that use on-chip pumps, resevoirs, and valves in conjuction with ultrathin membranes for shear reduction should be able to alter the microchemical environment of a cell in seconds instead of minutes.

2.6 References

1. Malek, A.M., et al., *Fluid shear stress differentially modulates expression of genes encoding basic fibroblast growth factor and platelet-derived growth factor B chain in vascular endothelium.* Journal of Clinical Investigation, 1993. **92**(4): p. 2013.
2. Duan, Y., et al., *Shear stress-induced changes of membrane transporter localization and expression in mouse proximal tubule cells.* Proceedings of the National Academy of Sciences, 2010. **107**(50): p. 21860-21865.
3. Flores, D., et al., *Fluid shear stress induces renal epithelial gene expression through polycystin-2-dependent trafficking of extracellular regulated kinase.* Nephron Physiology, 2010. **117**(4): p. p27-p36.
4. Mitchell, M.J. and M.R. King, *Shear-induced resistance to neutrophil activation via the formyl peptide receptor.* Biophysical Journal, 2012. **102**(8): p. 1804-1814.
5. Simmers, M.B., A.W. Pryor, and B.R. Blackman, *Arterial shear stress regulates endothelial cell-directed migration, polarity, and morphology in confluent monolayers.* American Journal of Physiology-Heart and Circulatory Physiology, 2007. **293**(3): p. H1937-H1946.
6. Hsu, S., et al., *Effects of shear stress on endothelial cell haptotaxis on micropatterned surfaces.* Biochemical and Biophysical Research Communications, 2005. **337**(1): p. 401-409.
7. Rainger, G.E., et al., *Neutrophils sense flow-generated stress and direct their migration through αvβ3-integrin.* American Journal of Physiology-Heart and Circulatory Physiology, 1999. **276**(3): p. H858-H864.
8. Sheikh, S., et al., *Exposure to fluid shear stress modulates the ability of endothelial cells to recruit neutrophils in response to tumor necrosis factor-α: a basis for local variations in vascular sensitivity to inflammation.* Blood, 2003. **102**(8): p. 2828-2834.
9. Valignat, M.-P., et al., *T Lymphocytes Orient against the Direction of Fluid Flow during LFA-1-Mediated Migration.* Biophysical Journal, 2013. **104**(2): p. 322-331.
10. Dewey Jr, C.F., et al., *The dynamic response of vascular endothelial cells to fluid shear stress.* Journal of Biomechanical Engineering, 1981. **103**(3): p. 177-185.
11. Jeon, N.L., et al., *Neutrophil chemotaxis in linear and complex gradients of interleukin-8 formed in a microfabricated device.* Nature Biotechnology, 2002. **20**(8): p. 826-830.
12. Walker, G.M., et al., *Effects of flow and diffusion on chemotaxis studies in a microfabricated gradient generator.* Lab on a Chip, 2005. **5**(6): p. 611-618.
13. Nelson, R.D., P.G. Quie, and R.L. Simmons, *Chemotaxis under agarose: a new and simple method for measuring chemotaxis and spontaneous migration of human polymorphonuclear leukocytes and monocytes.* The Journal of Immunology, 1975. **115**(6): p. 1650-1656.

14. Boyden, S., *The chemotactic effect of mixtures of antibody and antigen on polymorphonuclear leucocytes.* The Journal of Experimental Medicine, 1962. **115**(3): p. 453-466.
15. Zigmond, S.H., *Ability of polymorphonuclear leukocytes to orient in gradients of chemotactic factors.* The Journal of Cell Biology, 1977. **75**(2): p. 606-616.
16. Zicha, D., G.A. Dunn, and A.F. Brown, *A new direct-viewing chemotaxis chamber.* Journal of Cell Science, 1991. **99**(4): p. 769-775.
17. Keenan, T.M. and A. Folch, *Biomolecular gradients in cell culture systems.* Lab on a Chip, 2007. **8**(1): p. 34-57.
18. Kamholz, A.E., et al., *Quantitative analysis of molecular interaction in a microfluidic channel: the T-sensor.* Analytical Chemistry, 1999. **71**(23): p. 5340-5347.
19. Wang, C.J., et al., *A microfluidics-based turning assay reveals complex growth cone responses to integrated gradients of substrate-bound ECM molecules and diffusible guidance cues.* Lab on a Chip, 2008. **8**(2): p. 227-237.
20. Diao, J., et al., *A three-channel microfluidic device for generating static linear gradients and its application to the quantitative analysis of bacterial chemotaxis.* Lab on a Chip, 2006. **6**(3): p. 381-388.
21. Cheng, S.-Y., et al., *A hydrogel-based microfluidic device for the studies of directed cell migration.* Lab on a Chip, 2007. **7**(6): p. 763-769.
22. Shamloo, A., et al., *Endothelial cell polarization and chemotaxis in a microfluidic device.* Lab on a Chip, 2008. **8**(8): p. 1292-1299.
23. Keenan, T.M., C.-H. Hsu, and A. Folch, *Microfluidic "jets" for generating steady-state gradients of soluble molecules on open surfaces.* Applied Physics Letters, 2006. **89**(11): p. 114103-114103-3.
24. Keenan, T.M., et al., *A new method for studying gradient-induced neutrophil desensitization based on an open microfluidic chamber.* Lab on a Chip, 2010. **10**(1): p. 116-122.
25. Bhattacharjee, N., et al., *A neuron-benign microfluidic gradient generator for studying the response of mammalian neurons towards axon guidance factors.* Integrative Biology, 2010. **2**(11-12): p. 669-679.
26. Kim, T., M. Pinelis, and M.M. Maharbiz, *Generating steep, shear-free gradients of small molecules for cell culture.* Biomedical Microdevices, 2009. **11**(1): p. 65-73.
27. VanDersarl, J.J., A.M. Xu, and N.A. Melosh, *Rapid spatial and temporal controlled signal delivery over large cell culture areas.* Lab on a Chip, 2011. **11**(18): p. 3057-3063.
28. Snyder, J.L., et al., *An experimental and theoretical analysis of molecular separations by diffusion through ultrathin nanoporous membranes.* Journal of Membrane Science, 2011. **369**(1): p. 119-129.
29. Ishimatsu, R., et al., *Ion-selective permeability of an ultrathin nanoporous silicon membrane as probed by scanning electrochemical microscopy using micropipet-supported ITIES tips.* Analytical Chemistry, 2010. **82**(17): p. 7127-7134.

30. Agrawal, A.A., et al., *Porous nanocrystalline silicon membranes as highly permeable and molecularly thin substrates for cell culture.* Biomaterials, 2010. **31**(20): p. 5408-5417.
31. Striemer, C.C., et al., *Charge-and size-based separation of macromolecules using ultrathin silicon membranes.* Nature, 2007. **445**(7129): p. 749-753.
32. Fang, D.Z., et al., *Pore size control of ultrathin silicon membranes by rapid thermal carbonization.* Nano Letters, 2010. **10**(10): p. 3904-3908.
33. Fang, D.Z., et al., *Methods for controlling the pore properties of ultra-thin nanocrystalline silicon membranes.* Journal of Physics: Condensed Matter, 2010. **22**(45): p. 454134.
34. Johnson, D.G., et al., *Ultrathin Silicon Membranes for Wearable Dialysis.* Advances in chronic kidney disease, 2013. **20**(6): p. 508-515.
35. Ehrenberg, M. and J.L. McGrath, *Binding between particles and proteins in extracts: implications for microrheology and toxicity.* Acta Biomaterialia, 2005. **1**(3): p. 305-315.
36. Hocdé, S.A., O. Hyrien, and R.E. Waugh, *Cell adhesion molecule distribution relative to neutrophil surface topography assessed by TIRFM.* Biophysical Journal, 2009. **97**(1): p. 379-387.
37. Granger, D.N. and P. Kubes, *The microcirculation and inflammation: modulation of leukocyte-endothelial cell adhesion.* Journal of Leukocyte Biology, 1994. **55**(5): p. 662-675.
38. Cinamon, G. and R. Alon, *A real time in vitro assay for studying leukocyte transendothelial migration under physiological flow conditions.* Journal of Immunological Methods, 2003. **273**(1): p. 53-62.
39. Koutsiaris, A.G., et al., *Volume flow and wall shear stress quantification in the human conjunctival capillaries and post-capillary venules in vivo.* Biorheology, 2007. **44**(5): p. 375-386.
40. Toetsch, S., et al., *The evolution of chemotaxis assays from static models to physiologically relevant platforms.* Integrative Biology, 2009. **1**(2): p. 170-181.
41. Lin, F., et al., *Effective neutrophil chemotaxis is strongly influenced by mean IL-8 concentration.* Biochemical and Biophysical Research Communications, 2004. **319**(2): p. 576-581.
42. Dagan, Z., S. Weinbaum, and R. Pfeffer, *Theory and experiment on the three-dimensional motion of a freely suspended spherical particle at the entrance to a pore at low Reynolds number.* Chemical Engineering Science, 1983. **38**(4): p. 583-596.
43. Snyder, J.L., et al., *High-performance, low-voltage electroosmotic pumps with molecularly thin silicon nanomembranes.* Proceedings of the National Academy of Sciences, 2013. **110**(46): p. 18425-18430.
44. Unger, M.A., et al., *Monolithic microfabricated valves and pumps by multilayer soft lithography.* Science, 2000. **288**(5463): p. 113-116.
45. Paik, K.-H., et al., *Control of DNA capture by nanofluidic transistors.* ACS Nano, 2012. **6**(8): p. 6767-6775.

Chapter 3
Modeling Fluidic Coupling Between Microfluidic Compartments Separated by a Porous Membrane[†]

3.1 Abstract

In the past decade a number of microfluidic devices have been developed for cell studies. Many such devices are designed to host a range of flow forces that are physiological to the cell types of interest. However, prediction of flow in microfluidic systems with multiple channels and complex geometry can be difficult. Consequently, some researchers resort to computational fluid mechanics (CFM) to assess the distribution of flow in their systems. CFM, however, requires heavy computational power and can be time-consuming when there exist large differences in system dimensions (for instance, when a large flow channel splits into several smaller manifolds). In this chapter, we structured an analytical model to predict the flow in the microfluidic device showcased in Chapter 2. Not only does the model allow a quick estimate of flow magnitudes, it helps one build an intuition about how the variation of device geometry

[†] Adapted from H.H. Chung, C.K. Chan, T.S. Khire, G.A. Marsh, A. Clark Jr., R.E. Waugh, and J.L. McGrath. (2014) "Highly permeable silicon membranes for shear free chemotaxis and rapid cell labeling", *Lab Chip*, **14**, 2456-2468.

dictates the distribution of flow. Because of its simplicity and structural analogy to many other devices, the analytical model has many applications. To verify the predictive power of the analytical model, we compared the model solution to both empirical data and CFM simulations for different sets of system parameters. In all instances, we observed a similar velocity profile and volumetric flow rates.

3.2 Introduction

The in- and out- flow of solutes in small volumes enables the precise control of a microenvironment for cell studies. The presence of flow, however, can be fatal to shear-sensitive cells [1-3] and sweep non-adherent cells out of a field of observation [4, 5]. Starting around 2005, a number of flow-based devices have emerged that place a strong emphasis on being shear-free [6]. These devices generally consist of at least two compartments, some used as the conduits for fluid flow, while others provide the space for cell-hosting.

In all these devices, permeable yet flow-resisting components are incorporated to allow the exchange of solutes between the compartments. The internal structure of these "flow dampers" typically consists of an array of parallel flow channels or a network of tortuous and interconnected flow paths (see Section 1.2.6 – 1.2.8). Examples of the former include track-etched polycarbonate membrane [7, 8] and microfabricated polydimethlsiloxane (PDMS) flow channels [9]; while examples of the latter include nitrocellulose membrane [5] and agarose hydrogel [10].

Since coupling of fluid still exists in the flow dampers, a transmission of flow occurs between the compartments. For a system to be "shear-free", the flow dampers must confer a sufficiently high flow resistance such that the flow propagating into the cell-hosting space is physiologically negligible. Many reports in the literature, however, implicitly assume that the cell-hosting compartment of devices are completely free of flow [5, 7, 8]. Consequently, none of these groups formally defined a threshold of shear stress below which they considered their systems as shear-free.

If we idealize the flow network of a microfluidic device to be interconnected resistors, the ratio of flow resistances between the adjoining channels dictates the proportion of flow through these channels. According to empirical observations and the works of Hagen and Poiseuille, the resistance of a flow channel is a function of the channel geometry [11]. Thus the propagation of flow through the flow dampers ultimately depends on the internal structure of the flow dampers and the geometry of the adjoining compartments.

While a few groups did perform computational fluid mechanics (CFM) simulations to predict the distribution of flow rates in their devices [2, 3, 9, 12], physical insights about the parameters that determine the distribution of flows are often elusive. Furthermore, the CFM simulations are often time-consuming to perform because many finite elements must be used to represent the numerous fine internal features of the flow dampers. By considering the extreme scenario where the flow damper is a homogeneous medium with a well-defined flow resistance (dimensions of $N \cdot sec/m^5$), the propagation of flow through the flow damper can be quickly estimated. Instead of solving the flow

through each internal flow path, only the bulk flow through the entire damper needs to be considered. The assumption of homogeneity is warranted as long as there are enough flow paths within the flow damper. Such is the case with most shear-free microfluidic systems because the length scale of the systems (mm) is several orders higher than the feature dimensions of the flow dampers (μm) [2, 6-9, 13]. The crux therefore lies in how one can assign an apparent resistance to the flow damper based on the spacings and the dimensions of the internal flow paths.

In the following sections, we present an analytical framework that allows the modelling of many membrane-based microfluidic devices. We represent each channel in the flow network as a resistor, each with a resistance defined by its channel geometry. We consider the basic network configuration of two horizontal resistors joined by an array of vertical resistors in between. Since this configuration is basic and seen in many shear-free devices, the proposed analytical framework is easy to generalize and widely applicable. We also present a method to assign an apparent resistance to the flow damper to expedite the CFM simulations. The flow damper is idealized to be composed of repeating unit cells, each containing a flow path at its center. Under such a scheme, the apparent resistance of the whole flow damper can be obtained by scaling the resistance of the unit cell by the number of unit cells.

Lastly, we demonstrate that both the analytical model and the idealization of the flow damper as a homogeneous medium yield flow predictions that are consistent with empirical data, a feat that has not yet been demonstrated in the existing body of literature.

3.3 Materials and Methods

3.3.1. Analytical Model

Without the loss of generality, we developed the analytical model in 2D to predict the amount of convective cross-talk between the flow and the cell compartments. The model considers an idealized membrane with pores arranged in hexagonal packing, and rows of pores aligned along the direction of flow (Fig. 3.1). Under such a idealization, all pores are distributed an equal distance away from each other.

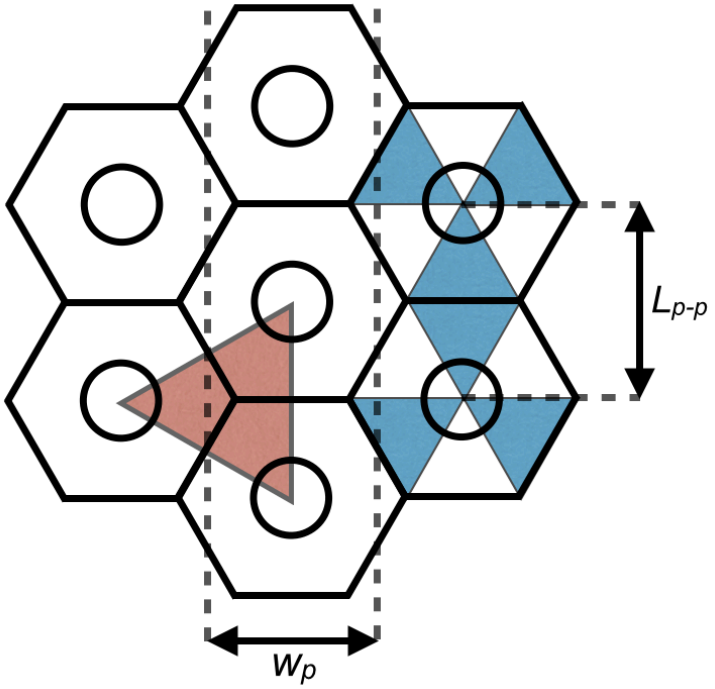

Figure 3.1: Pore arrangement in hexagonal packing. The membrane area is divided into tessellated hexagons, each containing a circular pore at its center. Under such arrangement, all pores are distributed in equal distance away from one other. Each hexagon can be divided into six identical equilateral triangles (blue). The center-to-center distance between any two neighboring pores ($L_{p\text{-}p}$) is twice the height of the blue triangle. The $L_{p\text{-}p}$ of any three neighboring pores also form an equilateral triangle (red). The width associated with each row of pores (w_p) is the height of the red triangle.

The porosity p, defined as the area of pores to the total membrane area, can be obtained by dividing the area of each circular pore (πR^2) by the area of each tessellated hexagon (A_{hex}). Thus:

$$p = \frac{\pi r^2}{A_{hex}} \qquad (3.3.1)$$

If each side of the hexagon has a length s, then

$$A_{hex} = 3\sin(60)\cdot s^2 \qquad (3.3.2)$$

Substitute Eqn. 3.3.2 into Eqn. 3.3.1 and rearrange, we have

$$s = \sqrt{\frac{\pi r^2}{3\sin(60)\cdot p}} \qquad (3.3.3)$$

As seen in Fig. 3.1, each hexagon can be divided equally into six identical equilateral triangles (denoted by the blue color). The pore-to-pore distance ($L_{p\text{-}p}$) is twice the height of each such triangle. Thus:

$$L_{p-p} = 2\sin(60)\cdot s = \sqrt{\frac{\pi r^2}{\sin(60)\cdot p}} \qquad (3.3.4)$$

If we connect the centers of any three neighboring pores, a larger equilateral triangle is formed (denoted by the red color in Fig. 3.1). The width associated with each row of pores, w_p, is the height of the formed triangle:

$$w_p = L_{p-p}\cdot\sin(60) \qquad (3.3.5)$$

The connection of pores to the flow and the cell compartments is idealized in Fig. 3.2 below:

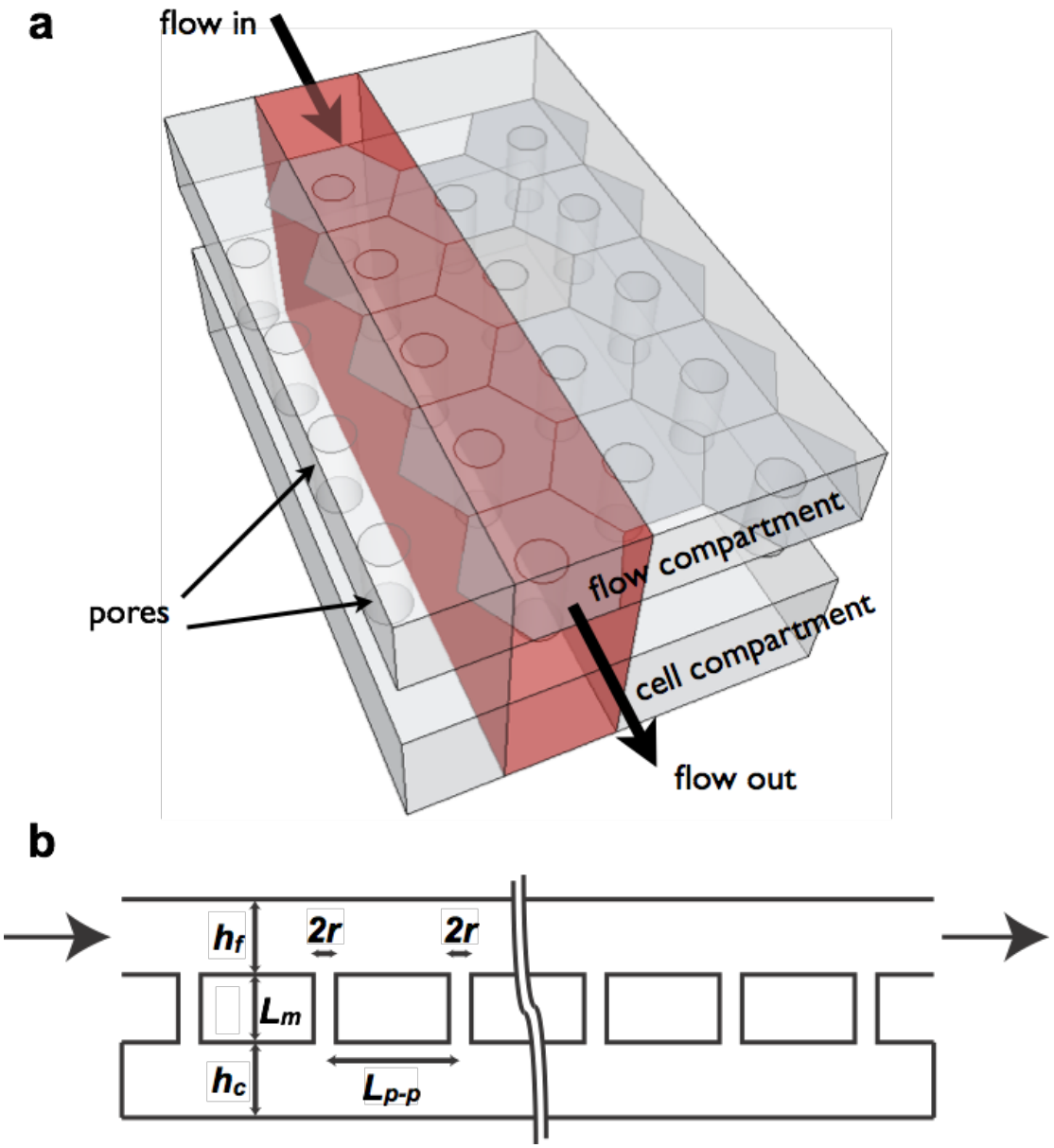

Figure 3.2: Idealized coupling of pores to the flow and the cell compartments. a. Idealized model geometry. Along the direction of flow, the pores are connected in parallel to the flow compartment at the top and the cell compartment at the bottom. **b**. A simplified 2D cross section, with key dimensions labeled: r is the pore radius, L_m is the membrane thickness, $L_{p\text{-}p}$ is the pore-to-pore spacing, and h is the chamber height. The subscripts f and c denote the flow and the cell compartments, respectively.

We solve the flow in the compartments and the pores using an electrical circuit analogy (Fig. 3.3). Each flow path is assigned a resistance, and is connected to one another either in series or in parallel:

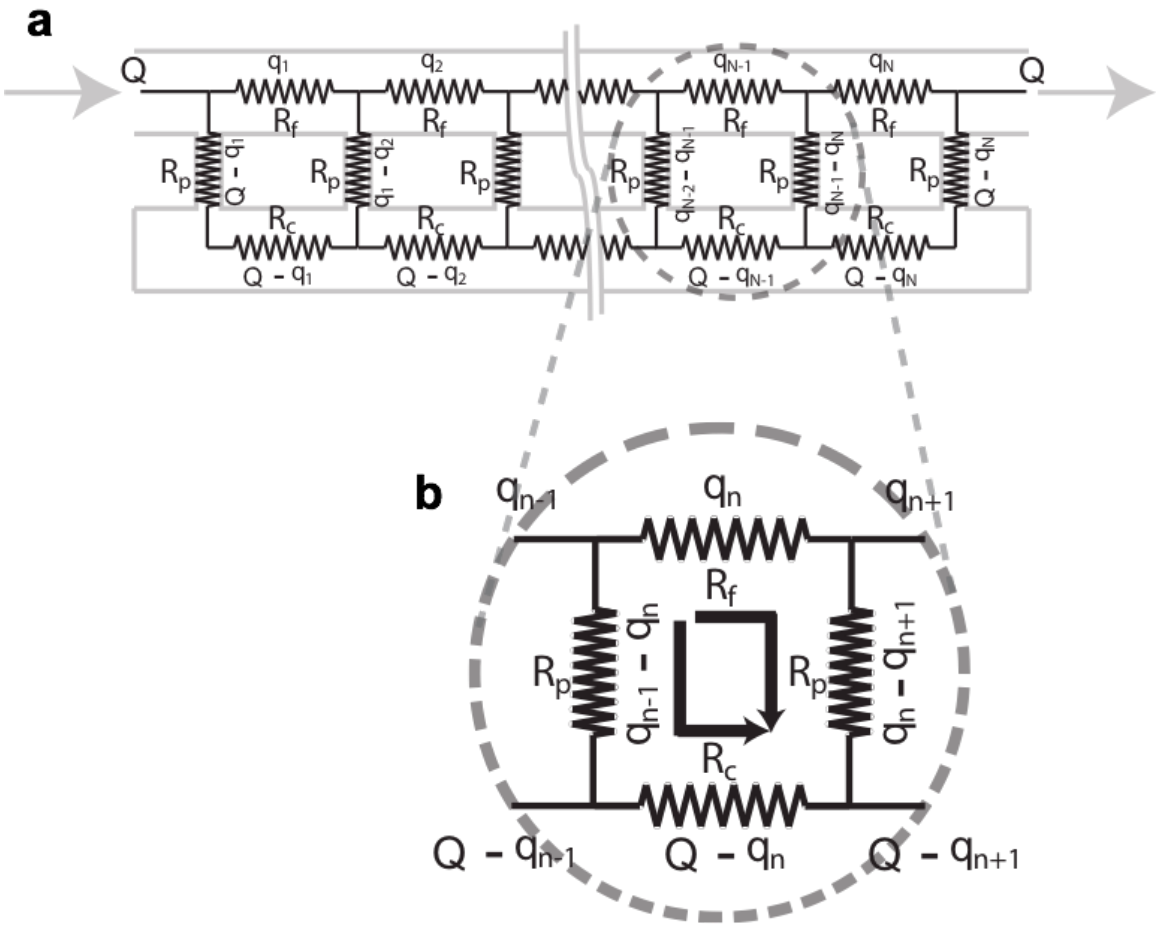

Figure 3.3: Electric circuit representation of network flow. a. A circuit representation of the idealized network of flow. The subscript n indexed each repeating segment of the circuit loop, and N is the total number of segments. Q is the input flow rate, and the q_n's are the flow rate through each segment of the flow compartment. R_p, R_f, and R_c are the resistances of the pore, the flow compartment, and the cell compartment, respectively. **b.** A unit circuit loop used to generalize the network flow. The pressure drops along the two flow paths (indicated by the arrows) are equal. This equality forms the recurrence relation that is solved to find the flow rate through any channel in the network.

By indexing the flow compartment flow rate (q_1, q_2, … , q_N in Fig. 3.3a) within a unit segment of length $L_{p\text{-}p}$, and taking into account that the pressure drops along the two indicated flow paths within a unit flow loop are equal (Fig. 3.3b), we obtain a generalized recurrence relation that allows us to solve the flow rates throughout the entire network. The full derivation is given in the Supplementary Information Section (Section 3.7).

The flow rate in the n^{th} segment of the cell compartment, $q_c(n)$, is given by:

$$q_c(n) = Q\left(\frac{R_f}{R_f + R_c}\right)\left[1 - \omega(n)\right] \qquad (3.3.6)$$

where $$\omega(n) = \frac{e^{\beta \cdot n}}{e^{\beta} + e^{\beta \cdot N}} + \frac{e^{-\beta \cdot n}}{e^{-\beta} + e^{-\beta \cdot N}} \qquad (3.3.7)$$

and $$\beta = \cosh^{-1}\left(\frac{2R_p + R_f + R_c}{2R_p}\right) \qquad (3.3.8)$$

N is the total number of segments. Q is the input flow rate. R_p, R_f, and R_c are the resistance of the pore, the flow compartment, and the cell compartment in each flow loop, respectively (Fig. 3.3b).

R_p, R_f, and R_c can be calculated using the Hagen-Poiseuille equation, which describes flow resistance as a function of channel geometry and fluid viscosity:

$$R_{rec} = \frac{12\mu L}{wh^3} \quad \text{and} \quad R_{cyl} = \frac{8\mu L}{\pi r^4} \qquad (3.3.10 \ \& \ 3.3.11)$$

the subscripts *rec* and *cyl* denote channels with rectangular and cylindrical cross section, respectively; μ is the fluid viscosity, L is the channel length, w and h are the rectangular channel width and height, and r is the cylinder radius. For each flow loop (Fig. 3.2b and Fig. 3.3b), the flow and cell compartment channel length is $L_{p\text{-}p}$, and the length of pore is the thickness of the membrane (L_m).

Since the membrane is thin, entrance/exit effects have a strong influence on the flow through the pore. The work of Dagan et al. [14] described the flow resistance of a short through pore (L/r ~ 1) as:

$$R_{pore} = \frac{\mu}{r^3}\left[3 + \frac{8}{\pi}\left(\frac{L}{r}\right)\right] \qquad (3.3.12)$$

Note that for $L >> r$, $R_{pore} \approx R_{cyl}$.

The resistances defined in Eqn. 3.3.10 and Eqn. 3.3.12 are readily applicable to Eqn. 3.3.6, from which the cell compartment flow rates are solved for a volume defined by a single row of pores (Fig. 3.2a). To scale the solution for a volume consisting of multiple such rows, we divide the pore and compartment resistances by the total number of rows:

$$R_{f,full} = \frac{w_p}{W} R_f \qquad R_{c,full} = \frac{w_p}{W} R_c \qquad R_{p,full} = \frac{w_p}{W} R_p \qquad (3.3.12,\ 3.3.13, \&\ 3.3.14)$$

$R_{p,full}$, $R_{f,full}$, and $R_{c,full}$ are the full pore and compartment resistances along the entire membrane width; w_p is the associated width of each row (Eqn. 3.3.5), and W is the full membrane width. In essence, the rows of pores are treated as resistors that are connected

in parallel to form the full volume of the shear-free system. Table 3.3 below summarizes the modeling parameters and their values in our shear-free system.

Table 3.1: List of System Parameters and Their Values

μ	viscosity of water	10^{-3} Pa·sec
p	membrane porosity	6.9 % (69% SiN grid × 10% pnc-Si)
L	membrane length	4 mm
W	membrane width	500 μm
L_m	membrane thickness	15 nm
$L_{p\text{-}p}$	length per unit segment	108 nm (Eqn. 3.3.4)
w_p	width per row of pores	94 nm (Eqn. 3.3.5)
N	number of pores along length	36896 (= $L/L_{p\text{-}p}$)
W/w_p	number of rows of pores	5325

single pore

r_p	average pore radius	15 nm
L_p	pore length	15 nm (L_m)
R_p	flow resistance per pore	1.64×10^{21} N·sec/m^5 (Eqn. 3.3.12)

flow compartment (per unit segment)		cell compartment (per unit segment)	
L_f	108 nm (= $L_{p\text{-}p}$)	L_c	108 nm (= $L_{p\text{-}p}$)
h_f	350 μm (Fig. 3.2b)	h_c	100 μm (Fig. 3.2b)
w_f	94 nm (= w_p)	w_c	94 nm (= w_p)
R_f	3.23×10^8 N·sec /m^5 (Eqn. 3.3.10)	R_c	1.39×10^9 N·sec/m^5 (Eqn. 3.3.10)

3.3.2 Finite Element Model

We calculated the flow rate expected in the cell compartment using a commercial finite element analysis package (COMSOL, Stockholm, Sweden). For ease of computation and quickness of assessment, we created initial models with few very large pores. To relieve the computational strain in modeling micron-sized compartments and the numerous nanometer-sized pores with a single continuous mesh, we created simplified models where the membrane is treated as one continuous porous medium. The Darcy permeability (K) of the porous medium is determined by:

$$K = \frac{\mu L_m p}{\pi r^2 R_{pore}} \qquad (3.3.15)$$

The complete derivation of Eqn. 3.3.15 is given in Section 3.7. The flow field before and after the flow through the membrane is determined with the steady-state Navier-Stokes equation. To further relieve the computational challenges, we assumed a microscale membrane thickness, found trends as a function of thickness, and extrapolated results to the nanoscale. We created a baseline case in which the membrane is 2 mm long by 500 μm wide and 30 μm thick. We then simulated different membrane lengths, thicknesses, porosities, and pore sizes to determine trends in the amount of fluid cross talk between compartments. Lastly, we extrapolated results to the actual membrane: length (4 mm), thickness (15 nm), porosity (6.9%), and pore radius (15 nm).

3.4 Results and Discussion

3.4.1 Analytical Model of Flow Reduction

The solution for cell compartment flow rate (Eqn. 3.3.6), given the parameters listed in Table 3.3, indicates that flow distribution is symmetric along the membrane length, varying from zero to zero with the maximum at mid-distance (Fig. 3.4). Such behavior is intuitively sound — as fluid passes by each pore, a small amount seeps into the cell compartment, slowly building up the flow magnitude. After the midway point, however, the cell compartment flow diminishes as the fluid returns to the flow compartment to conserve the total mass of fluid in the cell compartment.

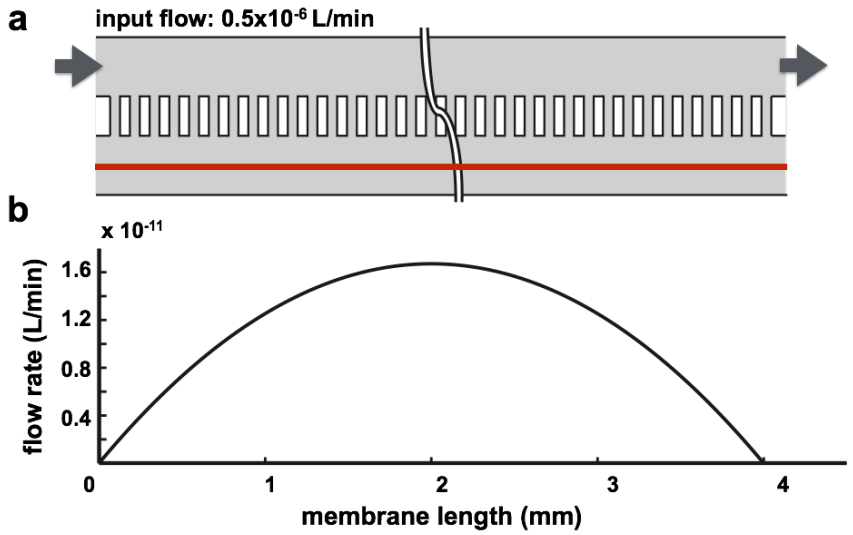

Figure 3.4: Analytical solution of cell compartment flow. a. A graphical representation of the 2D system. The arrows indicate the input and exit flow (0.50 μL/min for the chemotaxis experiment). The red line denotes a line-scan of the cell compartment. **b.** Volumetric rate of cell compartment flow along the length of the membrane. A symmetry is observed, which varies from zero to zero with the maximum at mid-distance. Note that the flow rate maximum is ~1.7×10^{-11} L/min, more than 10^4-fold less than the flow rate into the flow compartment.

The existence of peak volumetric flow at the midpoint of the cell compartment can also be appreciated by the analytical model by taking the derivative of ω (Eqn. 3.3.7) with respect to n to locate the maximum at $n = N/2$ (see Section 3.7).

The analytical model further provides insight into the conditions that produce flow reduction in the cell compartment. By Eqn. 3.3.6, the maximum possible flow rate in the cell compartment occurs when $\omega = 0$. Under this condition, the membrane is of no consequence and the flow simply splits between the flow and the cell compartments according to their relative resistances so that the maximum cell compartment flow rate becomes $Q \cdot Rf/(Rf+Rc)$. We abbreviate this membrane-independent flow rate as Q^*.

In essence, ω in Eqn. 3.3.6 describes the competition between pore resistance and pore number in delaying the onset of Q^*. The pore resistance, normalized with respect to the compartment resistances, is described by the β term (Eqn. 3.3.8) in ω. Because the pore resistance is much higher than the compartment resistances in our shear-free system, $\cosh(\beta) \sim 1$ and $\beta << 1$, a condition which tends to keep $\omega \sim 1$.

With the porosity fixed, the length of the membrane determines how many pores are encountered by the flow before exiting the device. Fig. 3.5 below clearly shows the benefit of using a nanoporous (pore size < 100 nm) membrane for flow reduction as it allows much longer membranes to be used while keeping the cell compartment shear-free. For instance, for the 4 mm membrane span of our shear-free system, ~80% of Q^* would already be reached if the pore radius were 15 μm. With the actual pore radius of 15 nm, however, only ~0.15% of Q^* is reached (Fig. 3.5). Ultimately, flow is significant in the cell compartment only when the number of pores along the channel length, N,

becomes large enough that the product $\beta \cdot N$ is sizable (see ω in Eqn. 3.3.7).

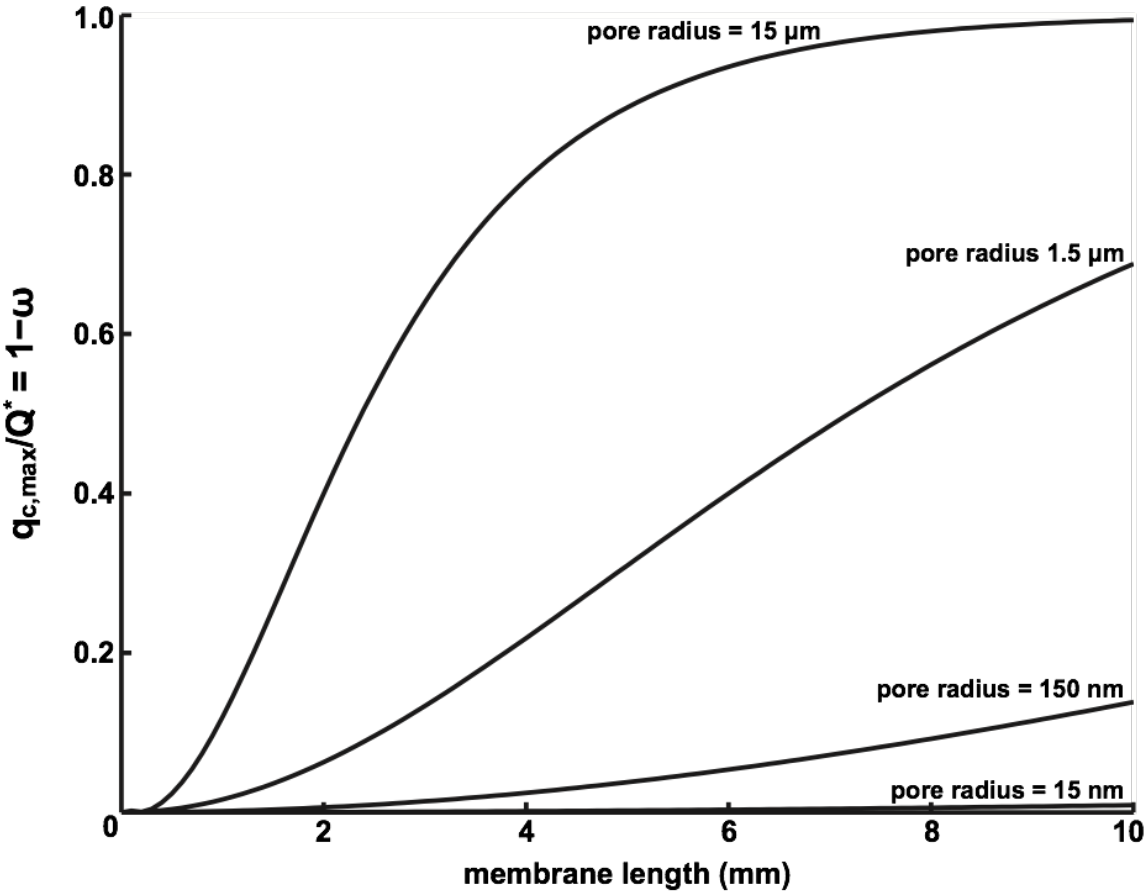

Figure 3.5: Impact of membrane pore size on cell compartment flow rate. The term $1 - \omega$ in Eqn. 3.3.6 describes the membrane's contribution to flow reduction. It is also equal to the ratio of the maximum flow rate in the cell compartment ($q_{c,max}$) to the membrane independent flow rate (Q^*). The figure demonstrates the advantages of using a nanoporous membrane over a microporous one for reducing the fluidic coupling between compartments (membrane thickness = 15 nm and porosity = 6.9%).

The strong influence of the $\beta \cdot N$ term on ω allows us to construct the non-dimensional curves shown in Fig. 3.6 to describe the partition of flow between compartments. Because pore sizes lower than 15 nm have only a small influence on the value of ω, the curves nearly all collapse to a 'universal' curve (Fig. 3.6).

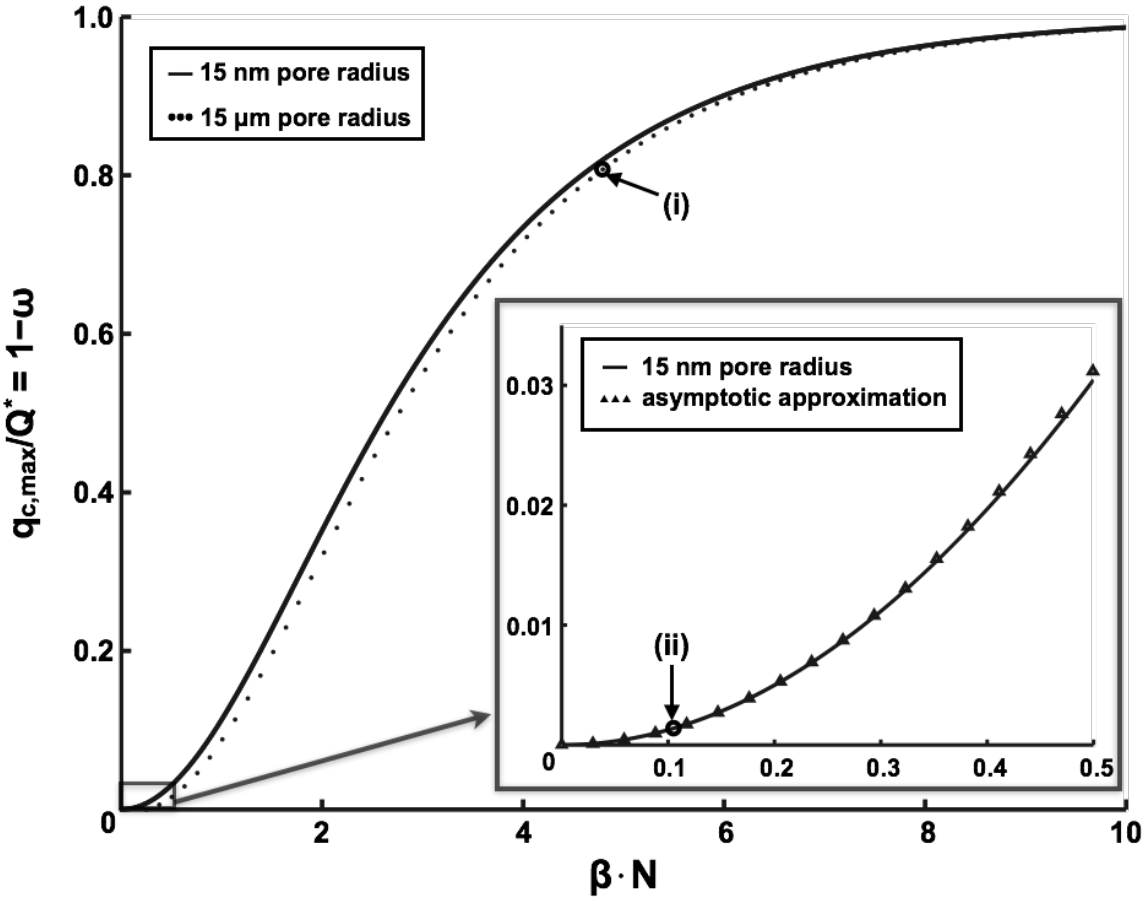

Figure 3.6: Competition of pore resistance and pore number in modulating the cell compartment flow rate maximum. Plotting $1 - \omega$ vs $\beta \cdot N$ for the case of small β results in a nearly universal curve for flow reduction. While the pore size has a minimal impact on the curve, it does impact the value of $\beta \cdot N$. Examples: (i) average pore radius = 15 µm, 4 mm long membrane, p = 6.9%, $\beta \cdot N$ = ~4.6, flow reduction = ~0.8; (ii) average pore radius = 15 nm, 4 mm long membrane, p = 6.9%, $\beta \cdot N$ is ~0.11, flow reduction = ~0.0015.

To approximate the characteristic profile of this universal curve, we make use of the fact that when the number of pores is large, $\beta << \beta \cdot N$. In this case, we can construct a Taylor expansion of Eqn. 3.3.6 to obtain the following asymptotic approximation (see Section 3.7):

$$q_{c,\max} = Q\left(\frac{R_f}{R_f + R_c}\right)\left[\frac{1}{8}(\beta \cdot N)^2\right] \qquad (3.3.16)$$

As long as $\beta < 1\times10^{-5}$ and $\beta \cdot N < 1/2$, a close agreement is found between the approximation above and the analytical solution in Eqn 3.3.6 (< 3% error), and the asymptotic approximation of $q_{c,max}$ is nearly identical to the solid line depicted in Fig. 3.6. For the membranes used in our work, we are at least 4-fold below these thresholds ($\beta \approx 2.94\times10^{-6}$ and $\beta \cdot N \approx 0.11$).

3.4.2 Computational Model of Flow Reduction

For initial assessment of network flow, we performed a finite element (COMSOL) simulation for an artificially short system with a few very large pores. The simulated flow distribution is consistent with that predicted by the analytical model (Fig. 3.7a). In addition to matching the symmetry of cell compartment flow, the COMSOL simulation also indicates that a plateau of flow rate maximum (Q^*) is quickly reached as the membrane doubles in length (Fig. 3.7b).

We also performed COMSOL simulations while varying the different membrane parameters (length, thickness, pore radius, and porosity) and found good agreement between the simulated flow rate maxima ($q_{c,max}$) and those solved using the analytical

model (Fig. 3.8). Furthermore, both models indicate that $q_{c,max}$ is quadratically-dependent on membrane length and pore radius, inversely proportional to membrane thickness, and linearly proportional to porosity. The nature of these dependences can be appreciated from the equation of membrane permeability (Eqn. 3.3.15) and the asymptotic approximation of cell compartment flow (Eqn. 3.3.16).

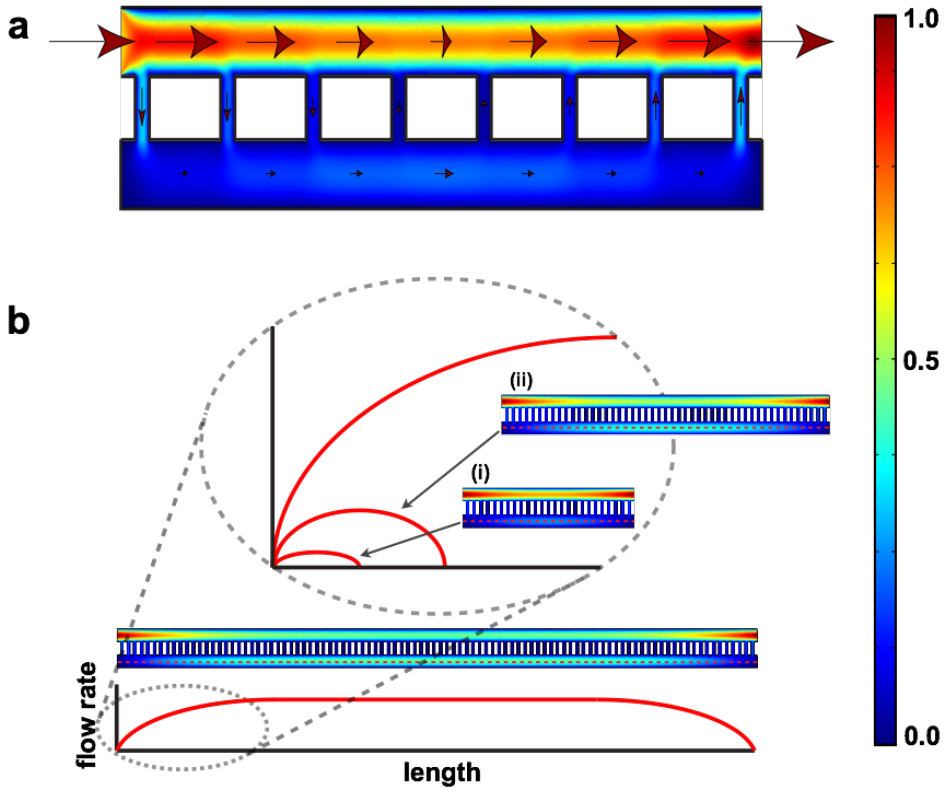

Figure 3.7: Flow rate distribution predicted from COMSOL simulation. a. Simulation of a system with short membrane span. The arrows indicate the directions of flow and the size of the arrows represents the magnitude of flow rate (not drawn to scale). The heat map reference to the far right indicates the magnitude of flow rate, with the red and blue representing the normalized maximum and minimum. **b.** Given a system with sufficiently long span of membrane, the flow rate in the cell compartment reaches a plateau value that is independent of the membrane. The key to achieving a shear-free condition is to use membranes that are much shorter than the length required to reach this plateau value.

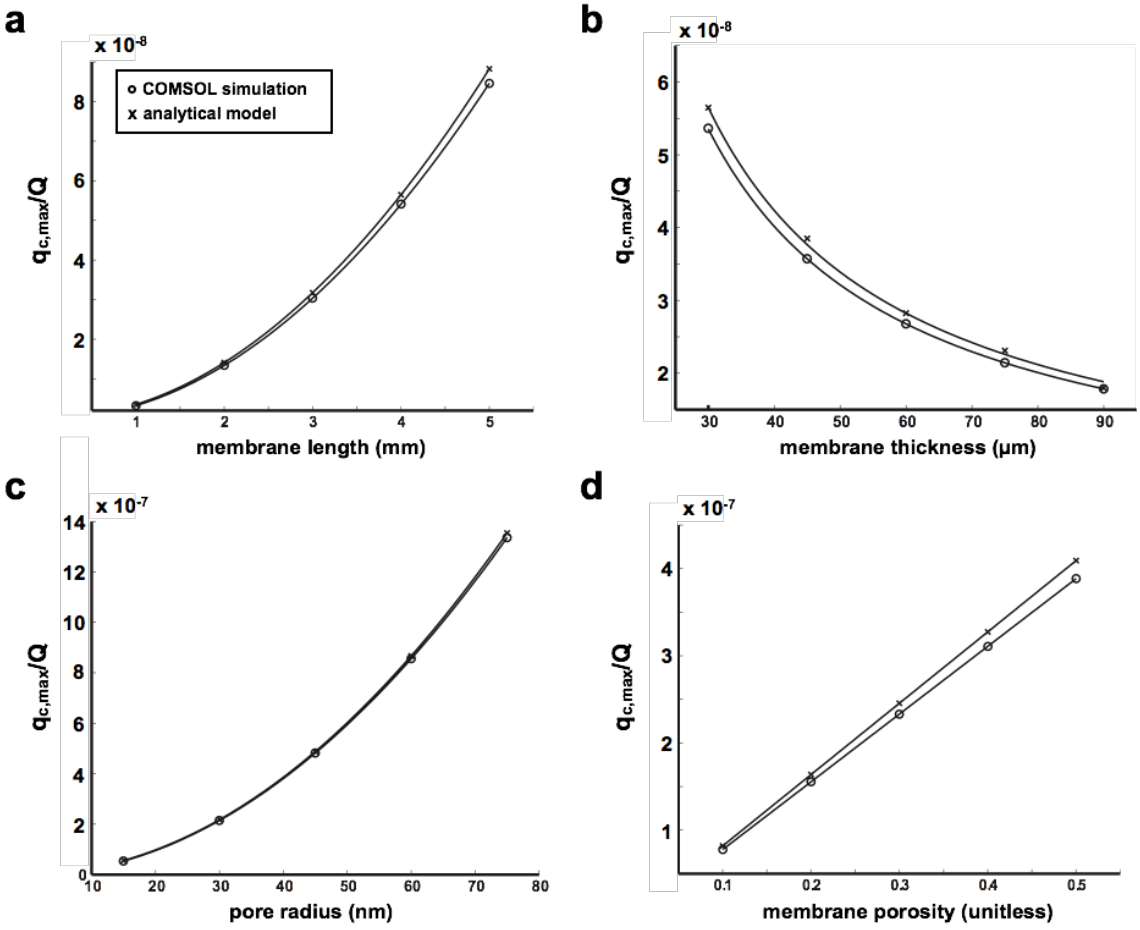

Figure 3.8: Comparison of flow reduction predicted by the analytical solutions and COMSOL simulations. The comparisons were made while varying different membrane parameters: **a.** membrane length, **b.** membrane thickness, **c.** average pore radius in the membrane, and **d.** membrane porosity. The cell compartment flow rate maxima $q_{c,max}$ were normalized by the input flow rate Q in the flow compartment to indicate flow reduction. The analytical solutions and COMSOL simulations both showed close agreement and predicted that flow reduction in the cell compartment is quadratically-dependent on membrane length (a) and pore radius (c), inversely proportional to membrane thickness (b), and linearly proportional to membrane porosity (d).

3.4.3 Comparison of Flow Prediction to Nanoparticle Tracking

To test the accuracy with which the analytical model predicts cell compartment flow, we compared the predicted $q_{c.max}$ to that measured through nanoparticle tracking (Chapter 2). Given an input flow rate of 100 μL/min in the flow compartment, particle tracking measured an average flow speed of 19 μm/min at the center of the membrane at the cell compartment mid-height where the flow is the fastest. In comparison, the analytical model predicted a maximum flow speed of 67 μm/min. While not an exact match, the analytical prediction is accurate to within the same order of magnitude. One immediate explanation for the overestimate is that we did make a few geometrical simplifications of our system to allow the flow rate prediction with our 2D analytical model, and these simplifications are intended to account for the highest cell compartment flow possible.

As seen in Fig. 3.9, the geometry of the flow and the cell compartments were both idealized to be perfectly rectangular. However, the true channel cross sections of the flow compartment differ from the idealized rectangle because the silicon wafer etches at an angle of 54.7° to expose a free-standing membrane (see section 2.3.1 in Chapter 2). The 54.7° angle corresponds to the crystal plane alignment of silicon and is a result of standard silicon wafer fabrication.

To avoid the possibility that during device assembly, the membrane would break on contact with the cell compartment gasket in the event of a misalignment, the cell compartment width (1400 μm) is purposely designed to be much larger than the 500 μm width of the membrane (see section 2.3.2 in Chapter 2). For the 2D analytical model, however, the cell compartment width is idealized to match the membrane width.

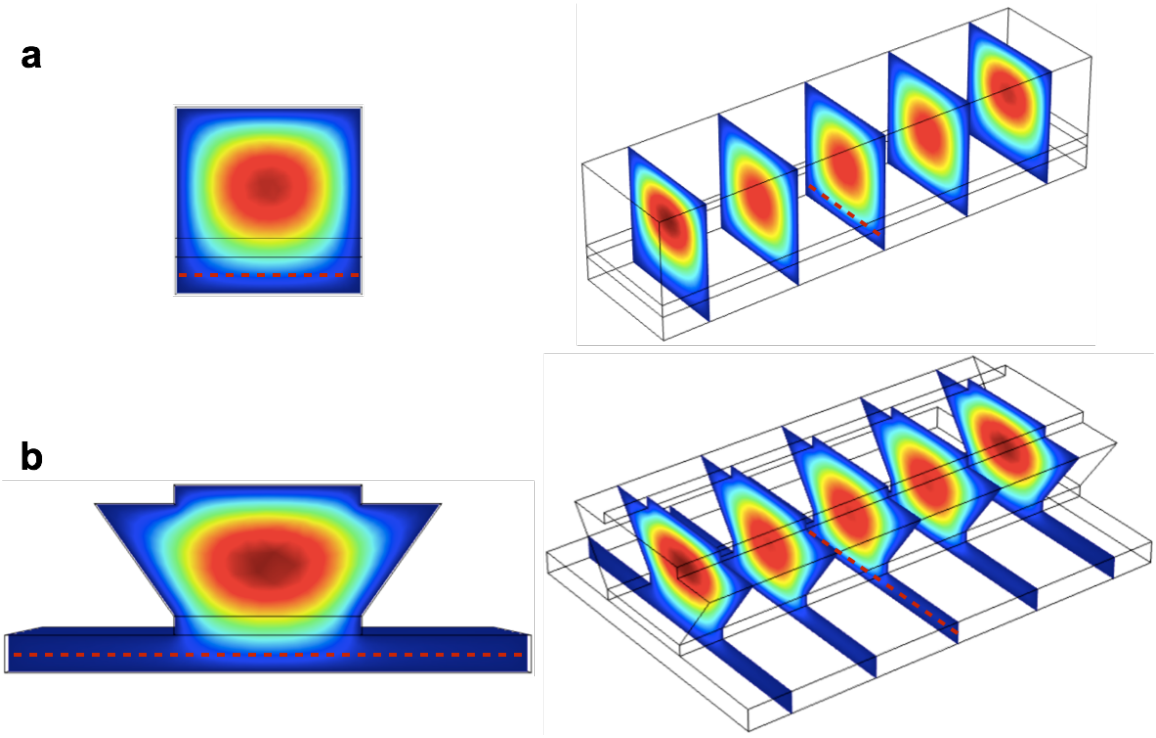

Figure 3.9: 3D COMSOL simulations of fluid flow for the idealized and the true system geometry. a. Idealized system geometry for the analytical modeling. **b.** True system geometry. The flow compartment has angular features that differ from the idealized rectangular cross section. The cell compartment below is also wider than the membrane. The dashed line denotes the cell compartment mid-height where the flow rates were obtained and compared. The predicted $q_{c,max}$ in the idealized system geometry is ~1.30 times higher than that of the true system geometry.

We performed 3D COMSOL simulations to assess how the maximum cell compartment flow would differ between the idealized and the true system geometries and obtained a correction factor of 0.76 (true:idealized), which lowers the predicted $q_{c,max}$ from 67 μm/min to 51 μm/min. While we assumed identical pore size in the membrane, in reality a distribution of the pore sizes exists. Accounting for the variability in pore size, we obtained a membrane permeability that is 1.8 times higher, thereby correcting the predicted $q_{c,max}$ from 51 μm/min to 92 μm/min (more details given in Section 3.7.5).

Additional discrepancy from the particle tracking can be accounted by the fact that not all particles tracked are in exact focus at the cell compartment mid-height, and not all particles are flowing along the center line of membrane width. Since the maximum flow speed is 1.5 times that of the average flow speed, we correct the predicted flow speed from 92 μm/min to 61 μm/min. While student's *T*-test at an alpha level of 0.05 indicated that the flow speeds measured from particle tracking (Section 2.4.1) have a mean (20 μm/min) that is different from the predicted value of 61 μm/min, the analytical prediction is nevertheless accurate to within the same order of magnitude.

We did not interrogate the predictive power of the analytical model at the higher input flow rates because the membranes start to exhibit periodic deflections and higher instances of membrane breakage. The periodic deflections occur due to the inability of the syringe pump to thread smoothly with the use of stepper motor [15], while the membrane breakages occur simply due to the higher pressure exerted on the membranes. At the lower input flow rates (<100 μL/min), an accurate verification of the analytical model is not possible because the flow reduction is sufficiently high that thermal fluctuations substantially influence nanoparticle motions (see Fig. 2.2).

3.4.4 Extension of the Analytical Model to Other Shear-free Microfluidic Systems

The analytical model presented in this chapter also provides insights to the distribution of flow in other microfluidic systems. For instance, the analytical model directly applies to the chemotaxis systems of VanderSarl et al. [8] because they are analogous in geometry and boundary conditions. The prediction of flow in the three-

compartment systems, such as those of Diao et al., Cheng et al., and Shamloo et al. [5, 9, 10], is also possible by applying the principle of axisymmetry to the analytical model.

As seen Fig. 3.10, the three-compartment system is composed of the mirror images of the analytical model. In each mirror image, the velocity profiles are identical. Consequently, we only need to solve the velocity profile for one of the images to which the analytical model readily applies. We summarized the $q_{c,max}$ predicted by the analytical model for the different systems in Table 3.4 below. To our knowledge, only Shamloo et al. had performed COMSOL simulations to estimate the flow reduction enabled by their three-compartment system [9]. The maximum flow speed of 1.5 μm/min that Shamloo et al. simulated, however, differs from the 1.21 nm/min predicted by our analytical model by three orders of magnitude. We believe the COMSOL simulation performed by Shamloo et al. is erroneous because their simulated $q_{c,max}$ is only ten-fold lower than the theoretical maximum possible in the cell compartment. Furthermore, our iteration of COMSOL simulation yielded a maximum flow speed of 0.54 nm/min, at the same order of magnitude as our model prediction. As expected, the COMSOL simulated $q_{c,max}$ is less than our model prediction because the arrays of manifolds that connect to the cell compartment are situated at the bottom of the flow compartments where the flow magnitudes are lower, whereas in the analytical model these arrays are situated at the flow compartment mid-height where the flows are maximal.

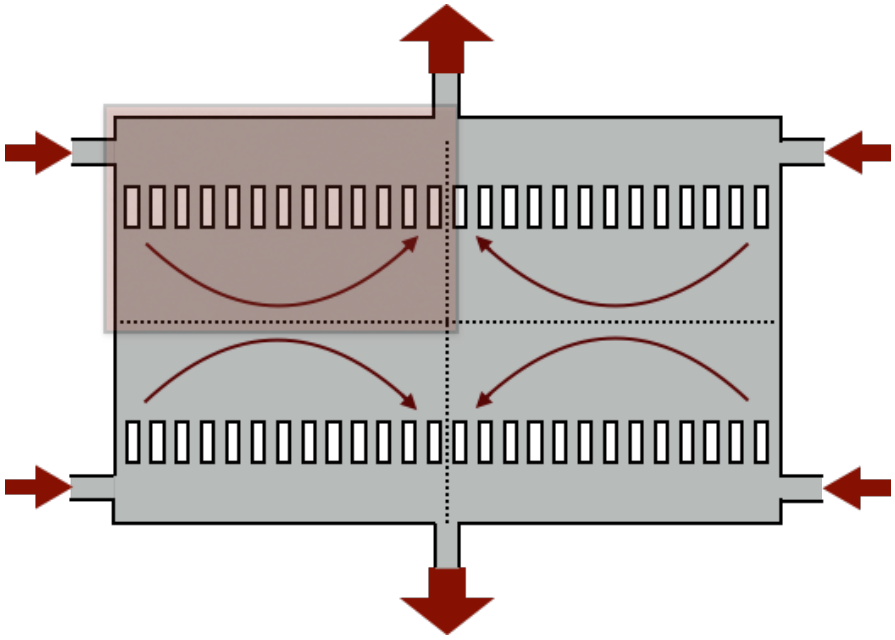

Figure 3.10: Three-compartment system represented as mirror images of the analytical model. The geometry of the three-channel system, such as the one showcased by Shamloo et al., is composed of four mirror images of the analytical model (demarcated by the dash lines, with one high-lighted in red). Flows enter the four inlets on the left and right and exit through the outlets on the top and bottom. The arrows indicate the directions of flow, with the magnitude represented by the arrow size. As a consequence of axisymmetry, the distributions of flow magnitudes are identical for each of the four mirror images.

Table 3.2: Prediction of Flow Reduction for Different Shear-free Systems

	Q_{in}	$q_{c,max}$	*flow reduction*
Shamloo et al.	8.0 nL/min	72 fL/min	2.76×10^4
Kim et al.	0.2 μL/min	2.4 pL/min	6.85×10^4
VanderSarl et al.	2.0 μL/min	21 pL/min	9.70×10^4
Chung et al.	0.5 μL/min	17 pL/min	2.99×10^4

The analytical model also allows flow rate estimates for each manifold in the array. For instance, in the work of VanderSarl et al., the cells are seeded directly on top of a membrane where flow forces are exerted through the pores [8]. These pores are analogous to the arrays of manifolds. Based on the flow rate predicted by the analytical model, the maximum force exerting through a single pore is 0.69 pN. Since there are < 5 pores at the basal size of the neutrophil [7, 8], the total normal force acting on the neutrophil (through the pores) is negligible compared to the average traction force that neutrophils generate during their migration (~30-70 nN) [16].

The analytical model can be further generalized to include the following boundary conditions: 1. Input flow in the flow compartment only, while the opposite ends of the flow and the cell compartment are open to atmosphere (Fig. 3.11a). 2. Unidirectional flows are given in both the flow and the cell compartment, while the other ends of the compartments are open to atmosphere (Fig. 3.11b). These two sets of boundary conditions can be considered as special cases of the analytical model that already had the absolute flow rate maximum (Q^*) attainted in the cell compartment (Fig. 3.11a & 3.11b), and the same solutions (Eqn. 3.7.17 & Eqn. 3.7.18) immediately apply for the prediction of system flow.

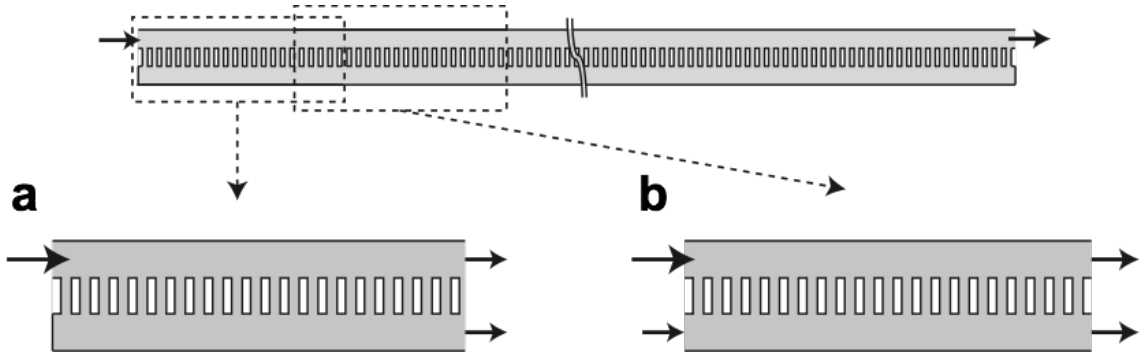

Figure 3.11: Special cases of the analytical model. a. The flow and the cell compartment are both opened to atmosphere. In this case the flow rates at the two open ends are dependent on the length of the system. **b.** When input flows are given in both the flow and the cell compartment, and the two other ends of the compartments are open to atmosphere. The solutions to case (a) and case (b) are already obtained if we solve the flow rates for a system so sufficiently long that the absolute flow rate maximum (Q^*) is already attainted in the cell compartment.

3.5 Summary and Conclusions

While microfluidic devices are powerful tools for the study and culturing of cells, the associated flow forces can promote unintended cellular response. In this chapter, we structured an analytical model to predict the flow in microfluidic systems that have the popular configuration of two compartments separated by a semipermeable medium. The semipermeable medium allows diffusive exchange of soluble factors while conferring a high resistance to flow, thereby reducing the propagation of flow forces between the compartments. The analytical model allows quick assessment of whether or not the level of flow forces propagated to the cells is physiological, and aid in the engineering design of the device to redistribute flow forces. The model solution has a physically meaningful form that is simple to follow, and can be further generalized to predict the distribution of flow in other microfluidic devices.

3.6 References

1. Dertinger, S.K.W., et al., *Gradients of substrate-bound laminin orient axonal specification of neurons.* Proceedings of the National Academy of Sciences, 2002. **99**(20): p. 12542-12547.
2. Bhattacharjee, N., et al., *A neuron-benign microfluidic gradient generator for studying the response of mammalian neurons towards axon guidance factors.* Integrative Biology, 2010. **2**(11-12): p. 669-679.
3. Wang, C.J., et al., *A microfluidics-based turning assay reveals complex growth cone responses to integrated gradients of substrate-bound ECM molecules and diffusible guidance cues.* Lab on a Chip, 2008. **8**(2): p. 227-237.
4. Abhyankar, V.V., et al., *Characterization of a membrane-based gradient generator for use in cell-signaling studies.* Lab on a Chip, 2006. **6**(3): p. 389-393.
5. Diao, J., et al., *A three-channel microfluidic device for generating static linear gradients and its application to the quantitative analysis of bacterial chemotaxis.* Lab on a Chip, 2006. **6**(3): p. 381-388.
6. Keenan, T.M. and A. Folch, *Biomolecular gradients in cell culture systems.* Lab on a Chip, 2007. **8**(1): p. 34-57.
7. Kim, T., M. Pinelis, and M.M. Maharbiz, *Generating steep, shear-free gradients of small molecules for cell culture.* Biomedical microdevices, 2009. **11**(1): p. 65-73.
8. VanDersarl, J.J., A.M. Xu, and N.A. Melosh, *Rapid spatial and temporal controlled signal delivery over large cell culture areas.* Lab on a Chip, 2011. **11**(18): p. 3057-3063.
9. Shamloo, A., et al., *Endothelial cell polarization and chemotaxis in a microfluidic device.* Lab on a Chip, 2008. **8**(8): p. 1292-1299.
10. Cheng, S.-Y., et al., *A hydrogel-based microfluidic device for the studies of directed cell migration.* Lab on a Chip, 2007. **7**(6): p. 763-769.
11. Whitaker, S., *Introduction to fluid mechanics*. 1981: Krieger.
12. Keenan, T.M., C.-H. Hsu, and A. Folch, *Microfluidic "jets" for generating steady-state gradients of soluble molecules on open surfaces.* Applied Physics Letters, 2006. **89**(11): p. 114103-114103-3.
13. Keenan, T.M., et al., *A new method for studying gradient-induced neutrophil desensitization based on an open microfluidic chamber.* Lab on a Chip, 2010. **10**(1): p. 116-122.
14. Dagan, Z., S. Weinbaum, and R. Pfeffer, *Theory and experiment on the three-dimensional motion of a freely suspended spherical particle at the entrance to a pore at low Reynolds number.* Chemical Engineering Science, 1983. **38**(4): p. 583-596.
15. Li, Z., et al., *Syringe-pump-induced fluctuation in all-aqueous microfluidic system implications for flow rate accuracy.* Lab on a Chip, 2014. **14**(4): p. 744-749.
16. Smith, Lee A., et al. *Neutrophil traction stresses are concentrated in the uropod during migration*. Biophysical Journal, 2007, **92**(7): L58-L60.

3.7 Supplementary Information Section (SIS§)

3.7.1. Analytical Solution of Network Flow in the Shear-free System

By taking a longitudinal cross-section of the shear-free system we obtained the idealized flow network depicted in Fig. 3.2b, and its circuit representation in Fig. 3.3. The pressure drops along the two indicated flow paths are equal and form the basis of the recurrence relation below:

$$R_p\left(q_{n-1}-q_n\right)+R_c\left(Q-q_n\right)=R_f\left(q_n\right)+R_p\left(q_n-q_{n+1}\right) \qquad (3.7.1)$$

After expanding, grouping the flow rate terms with the same indices together, and rearranging terms, we obtain a 2nd order recurrence relation that describes the flow across the n^{th} unit circuit loop of the flow chamber:

$$q_n=\hat{R}_m\cdot q_{n-1}+\hat{R}_m\cdot q_{n+1}+\hat{R}_c\cdot Q \qquad (3.7.2)$$

with $\hat{R}_m=\dfrac{R_p}{2R_p+R_f+R_c}$ and $\hat{R}_c=\dfrac{R_c}{2R_p+R_f+R_c}$ (3.7.3 & 3.7.4)

The two dimensionless terms above can be thought of as normalized resistances of the membrane and the cell compartment, respectively.

Due to the last constant term, the 2nd order recurrence relation in Eqn. 3.7.2 is inhomogeneous with constant coefficients (that are independent of n). The closed form solution to Eqn. 3.7.2 will be a sum of a homogeneous and a particular solution.

Before solving Eqn. 3.7.2, we perform the following scaling transformation to simplify subsequent calculations:

$$\alpha = \frac{1}{2\hat{R}_m} \qquad \text{and} \qquad \hat{q} = \frac{\hat{R}_c \cdot Q}{\hat{R}_m} \qquad (3.7.5 \ \& \ 3.7.6)$$

Thus Eqn. 3.7.2 transforms to:

$$q_{n+1} - 2\alpha \cdot q_n + q_{n-1} = -\hat{q} \qquad (3.7.7)$$

Since R_p, R_f, and R_c are all positive, $\alpha > 1$.

Particular Solution:

The inhomogeneous term $\hat{q}$ does not depend on n, so we seek out a particular solution that is constant. Substituting $q_n = q^{(p)}$ into Eqn 3.7.7, we obtain:

$$q^{(P)} = \frac{\hat{q}}{2(\alpha - 1)} \qquad (3.7.8)$$

Homogeneous Solution:

Any solution to the homogeneous equation satisfies

$$q_{n+1} - 2\alpha \cdot q_n + q_{n-1} = 0 \qquad (3.7.9)$$

We try solution of the form

$$q_n = \mu^n \qquad (3.7.10)$$

Substituting Eqn.3.7.10 into Eqn. 3.7.9, we have:

$$\mu^2 - 2\alpha \cdot \mu + 1 = 0 \qquad (3.7.11)$$

which has the solution

$$\mu = \alpha \pm \sqrt{\alpha^2 - 1} \qquad (3.7.12)$$

We make one more transformation to simplify the calculations, let

$$\alpha = cosh(\beta) \qquad (3.7.13)$$

The above transformation is well-defined because for $\alpha > 1$, there is always a unique positive value of β that satisfies Eqn. 3.7.13.

After substituting Eqn. 3.7.13 into Eqn. 3.7.12, we have

$$\mu = cosh(\beta) \pm sinh(\beta) = e^{\beta}, e^{-\beta} \qquad (3.7.14)$$

The homogeneous solution is thus:

$$q_n^{(H)} = c_1 \cdot e^{\beta \cdot n} + c_2 \cdot e^{-\beta \cdot n} \qquad (3.7.15)$$

And the full solution to Eqn. 3.7.2 is

$$q_n = q_n^{(H)} + q_n^{(P)} = c_1 \cdot e^{\beta \cdot n} + c_2 \cdot e^{-\beta \cdot n} + \frac{\hat{q}}{2\left[cosh(\beta) - 1\right]} \qquad (3.7.16)$$

Applying the Boundary Conditions (B.C.):

We know that the entrance flow rate at $n = 1$ and the exit flow rate at $n = N$ are both equal to the input flow rate Q. We therefore have two equations for the two unknown constants c_1 and c_2 in Eqn. 3.7.16, giving us the final solution:

$$q_n = Q\left[\left(\frac{R_f}{R_f + R_c}\right)\left(\frac{e^{\beta \cdot n}}{e^{\beta} + e^{\beta \cdot N}} + \frac{e^{-\beta \cdot n}}{e^{-\beta} + e^{-\beta \cdot N}}\right) + \frac{R_c}{R_f + R_c}\right] \qquad (3.7.17)$$

The cell compartment flow rate at the n^{th} unit circuit, $q_c(n)$, is given by $Q - q_n$:

$$q_c(n) = Q\left(\frac{R_f}{R_f + R_c}\right)\left[1 - \left(\frac{e^{\beta \cdot n}}{e^{\beta} + e^{\beta \cdot N}} + \frac{e^{-\beta \cdot n}}{e^{-\beta} + e^{-\beta \cdot N}}\right)\right] \qquad (3.7.18)$$

At last, we let

$$\omega(n) = \frac{e^{\beta \cdot n}}{e^{\beta} + e^{\beta \cdot N}} + \frac{e^{-\beta \cdot n}}{e^{-\beta} + e^{-\beta \cdot N}} = \frac{e^{\beta(n-1)} + e^{-\beta(N-n)} + e^{-\beta(n-1)} + e^{\beta(N-n)}}{2 + e^{\beta(N-1)} + e^{-\beta(N-1)}}$$
$$= \frac{\cosh\left[\beta(n-1)\right] + \cosh\left[\beta(N-n)\right]}{1 + \cosh\left[\beta(N-1)\right]} \qquad (3.7.19)$$

which simplifies Eqn 3.7.18 to

$$q_c(n) = Q\left(\frac{R_f}{R_f + R_c}\right)\left[1 - \omega(n)\right] \qquad (3.7.20)$$

which is the solution described in the main text.

The solution is physically meaningful — the term $R_f/(R_f+R_c)$ describes the reduction of flow in the cell compartment as the ratio of flow compartment resistance to the total, and the term $1 - \omega(n)$ describes the flow reduction enabled by the membrane.

3.7.2. Assignment of Bulk Permeability to a Porous Medium

Darcy's Law states that the volumetric flow rate (Q) through a porous medium with a known thickness (L) and cross sectional area (A) is related to fluid viscosity (μ), the

pressure differential that drives the flow (ΔP), and the permeability of the medium (k) in accordance to the following relation:

$$Q = \frac{kA}{\mu L}\Delta P \qquad (3.7.21)$$

k is sometimes referred to as Darcy's permeability, and has the unit of m^2. Note that the $kA/\mu L$ term represents the apparent permeability of the porous medium, and is equivalent to the reciprocal of the resistance term in the Ohm's law. Darcy's permeability is an intrinsic property of the porous medium, as it depends on neither the fluid viscosity (μ) nor the apparent geometry of the porous medium (A or L). However, as its units suggest, Darcy's permeability represents the effective cross sectional area available to flow, and is ultimately a function of the cross sectional ultrastructure of the porous medium — if the pore size and pore distribution of the medium is known, Darcy's permeability can be calculated.

We begin by dividing a given membrane area into tessellated hexagons, each of which has a circular pore positioned at its center (as in Fig. 3.1). In this manner, the pores are all distributed in equal distance away from each other, and the porosity p can be calculated with Eqn. 3.3.1. We know the flow resistance of a cylindrical pore is R_{cyl} (Eqn. 3.3.11), and that in its most general definition permeability is the reciprocal of resistance. Thus the apparent permeability of each tessellated hexagon is $1/R_{cyl}$:

$$\frac{kA_{hex}}{\mu L} = \frac{1}{R_{cyl}} \qquad (3.7.22)$$

Expressing the area of the hexagon in terms of porosity (Eqn 3.3.1) and substituting into

Eqn 3.7.22, we have:

$$k = \frac{\mu L}{R_{cyl}}\left(\frac{p}{\pi r^2}\right) \qquad (3.7.23)$$

which is the relation given in the main text. Note that the conversion to Darcy's permeability presented in this section is applicable to any membrane that contains evenly-distributed through-pores. Such conversion is particularly useful in CFM modeling because it allows the numerous smaller channels to be treated as one medium with an equivalent permeability. In so doing, the number of elements required for the CFM modeling can be substantially reduced.

3.7.3. Finding the Flow Rate Maxima and Minima in the Cell Compartment

The flow rate maxima and minima in the cell compartment occur when ω is at its minimum and maximum. Although the variable n takes on only integer values, the function $\omega(n)$ is defined for all n, so we may use basic calculus techniques to find the minima and maxima. We follow the usual procedure of checking the endpoint values and then looking for stationary points in the interior. It is easy to see from the final form in Eqn. 3.7.19 that ω is 1 for both $n = 1$ and $n = N$ (a value required by the boundary conditions we imposed earlier). To check the interior points we find the derivative of $\omega(n)$ with respect to n. The result is

$$\frac{d\omega(n)}{dn} = \beta\frac{sinh\left[\beta(n-1)\right] - sinh\left[\beta(N-n)\right]}{1+cosh\left[\beta(N-1)\right]} \qquad (3.7.24)$$

From Eqn. 3.7.24 and the monotonicity of the *sinh*, it is easy to show that the derivative is negative for $n < \frac{1}{2}(N+1)$ and positive for $n > \frac{1}{2}(N+1)$. Hence there is a zero derivative and a minimum at $n_{\min} = \frac{1}{2}(N+1)$. If N is odd, this gives the number of the cell for which the minimum occurs. If N is even, the minimum occurs on either side of the mid-point. For N large, we do not need to worry about the distinction. The value of the minimum is obtained by substituting $n_{\min}$ into the Eqn 3.7.19 for ω. The result, after we simplify using the double angle formula for the *cosh*, is

$$\omega_{\min} = \omega\left(n_{\min}\right) = sech\left[\frac{\beta}{2}\left(N-1\right)\right] \qquad (3.7.25)$$

3.7.4. Asymptotic Approximation for the Cell Compartment Flow Rate Maximum

For our situation, we are interested in very small values of β and very large values of N such that $\beta \cdot N$ is of order one. We temporarily let $z = \beta \cdot N$ and we seek an expansion of ω_{min} in powers of β at fixed values of z. Using Eqn. 3.7.25 we write ω_{min} as

$$\omega_{\min} = sech\left[\frac{1}{2}\left(z-\beta\right)\right] \qquad (3.7.26)$$

We now use a Taylor series in β about $\beta = 0$. The result is

$$\omega_{\min} = sech\left(\frac{1}{2}z\right)\left[1+\frac{1}{2}tanh\left(\frac{1}{2}z\right)\beta + O\left(\beta^2\right)\right] \qquad (3.7.27)$$

For a small value of β we keep only the first term, which gives

$$\omega_{\min} = sech\left(\frac{1}{2}z\right) \qquad (3.7.28)$$

For moderate values of z, we can carry the approximation further by expanding the hyperbolic secant. The first three terms are

$$\omega_{\min} = sech\left(\frac{1}{2}z\right) = 1 - \frac{z^2}{8} + \frac{5z^2}{384} + O\left(z^6\right) \qquad (3.7.29)$$

For $z = 0.5$, for example, the third term is less than 0.1% of the first term. For z-values in that range, we may approximate ω_{min} and the maximum q_c as

$$\omega_{\min} = 1 - \frac{\left(\beta \cdot N\right)^2}{8}, \quad \text{and} \quad q_{c,\max} = Q\left(\frac{R_f}{R_f + R_c}\right)\left[\frac{1}{8}\left(\beta \cdot N\right)^2\right] \qquad (3.7.30)$$

which is the approximation given in the main text.

3.7.5. Correcting membrane permeability for the variation in pore size

Assuming all the pores in the membrane are resistors connected in parallel, the permeability of the membrane can be calculated as:

$$P_{mem} = \frac{1}{R_{mem}} = \sum_{i=1}^{N} \frac{1}{R_i} \qquad (3.7.31)$$

where P_{mem} is the membrane permeability, R is the pore resistance determined using the Dagan's equation (Eqn 3.3.12), and i indexes each individual pore.

Evaluating the membrane permeability base on the distribution of pore size (Fig. 3.12), we obtained a permeability value of 5.30×10^{-18} m^5/ N·sec (given the pore length of 15 nm and the viscosity of 1.0×10^{-3} Pa·sec).

In our idealized framework of analytical model, however, we assumed all the pore diameters to be identical to the mean. Under this premise, Eqn. 3.7.31 becomes

$$P_{mem} = \frac{N}{R_{\bar{r}}} \qquad (3.7.32)$$

where N is the total number or pores (400 in the case of Fig. 3.12), and $R_{\bar{r}}$ (1.36×10^{20} N·sec/ m^5) is the pore resistance obtained using the mean pore diameter (31.44 nm).

The membrane permeability obtained through Eqn. 3.7.32 (2.95×10^{-18} m^5/ N·sec) underestimates the true membrane permeability (5.30×10^{-18} m^5/ N·sec) by a factor of 1.80.

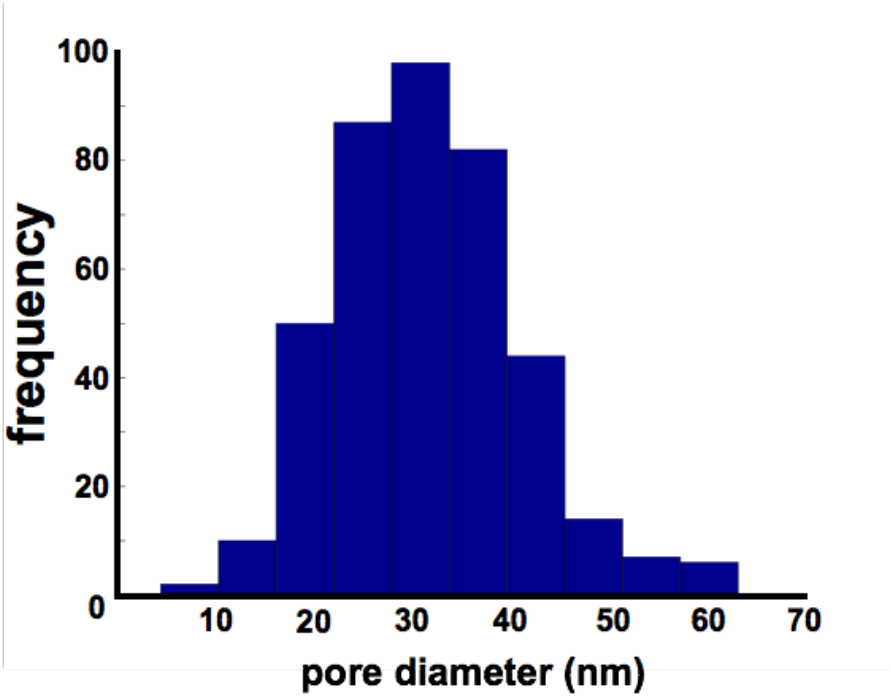

Figure 3.12: Representative distribution of pore diameter. The pore diameters, obtained from a scanning electron microscope (SEM) image, have the mean and the median of 31.44 nm and 31.48 nm, respectively.

Chapter 4
Neutrophil Haptotaxis

4.1 Abstract

During an immune response, circulating neutrophils attach to the vessel wall and laterally migrate before exiting to the surrounding tissue to seek out pathogens (as described in Section 1.1.1 and Fig.1.1 of Chapter 1). Throughout the entire process, neutrophils encounter numerous surface-presented signals, some of which activate the neutrophils, while others provide the foot-holds for the neutrophils to migrate. However, it is currently unclear if these molecules, when presented as a surface-bound gradient, can help in directing the migration of neutrophils to the pathogens.

In this study, we conducted neutrophil migration on immobilized gradients of an adhesion molecule (ICAM-1) and a chemoattractant (IL-8) to see if directed migration can be induced. ICAM-1 and IL-8 were chosen because both are highly involved in the activation and migration of neutrophils during an immune response. The immobilized gradients were created through either passive adsorption or linker-extension to mimic the glycocalyx that lines the vessel wall. We show through fluorescence labeling that the surface density of the immobilized IL-8 and ICAM-1 can be controlled to form different gradient profiles. We also show that the different immobilization procedures do not affect

the ability of the IL-8 and ICAM-1 to activate and bind to the neutrophils. However, of all the approaches taken, none were able to reproducibly promote directed migration. While it remains unclear if neutrophil haptotaxis can be promoted on IL-8 or ICAM-1, the protocol we established is applicable to other molecules for the guided migration of different cell types.

4.2 Introduction

Haptaotaxis is the directed migration of cells on an immobilized gradient of molecules or surface characteristic. While the first demonstration of haptotaxis dates back to the 1960's [1], there are still very few reports of haptotaxis in the literature. Whereas there are more than 33,000 chemotaxis-related publications in the PubMed archive, haptotaxis-related publications numbered less than 230, and of these, only twelve directly pertain to the primary human neutrophil. This large contrast in the number of publications may be due in part to the rarity with which haptotaxis is observed *in vivo* or the technical challenges involved in promoting haptotaxis *in vitro*.

Neutrophils encounter a number of surface-presented signals during the mediation of an immune response, and it is possible that a gradient of these signals helps induce the haptotaxis of neutrophils to locate the pathogens. The notion of haptotaxis is particularly appealing for the lateral migration of neutrophils on the vessel wall because the immobilized signals confer both site-specificity and robustness against the dilution of signals due to blood flow.

To identify if immune cells undergo hatpotaxis, we have used microfluidic approaches to generate immobilized gradients of intercellular adhesion molecule-1 (ICAM-1) and interleukin-8 (IL-8, CXCL-8), and then tested their effectiveness at inducing directed migration of human neutrophils. ICAM-1 is an adhesion molecule that binds integrin, and IL-8 is a well-known chemoattractant for neutrophils. Previous work in the literature has indicated that the "hot spots" of neutrophil recruitment are associated with high surface densities of IL-8 [2, 3] and ICAM-1 [2, 3]. While canonically, the recruitment of neutrophils to particular areas of the vascular wall is thought to be mediated by flow-assisted adhesion, we propose that ICAM-1- and IL-8- mediated haptotaxis is also a possible mechanism of neutrophil enrichment at particular locations along the vessel wall.

Since ICAM-1 is thought to function primarily as a mediator of cell adhesion, and not as a cell attractant, it is not surprising that currently there are no published works that specifically investigated ICAM-1-mediated neutrophil haptotaxis. While IL-8 is a neutrophil chemoattractant that is widely used in the literature, it is unclear if the immobilized form can direct migration. We do know, however, that soluble IL-8 (~17 pg/mL - 20 ng/mL) can be found in blood circulation in the instance of severe immune response or after the intravenous injection of endotoxin [4-7], and that IL-8 can also bind to the endothelial glycocalyx at specific binding sites [8-11].

To date, there was only one study that specifically examined IL-8-mediated neutrophil haptotaxis [12]. The study entailed an *in vitro* set up using the Boyden chamber. The immobilized IL-8 gradient was formed on the membrane inside the Boyden

chamber by incubating pure media on one side of the membrane and IL-8 (0.1, 1, or 1 μg/mL) on the other [12]. When the neutrophils are seeded on the side that was incubated with IL-8, the membrane is defined as "negatively haptotactic". When the neutrophils are seeded on the opposite side, the membrane is defined as "positively haptotactic". Since the membrane is typically ~10 μm thick, the formed gradient spanned no more than two cell body lengths (neutrophil averaged ~7-9 μm in diameter). Furthermore, the cell migration and the presence of the immobilized gradient could not be directly assessed because the membrane is opaque. The study, however, did find that the percentage of neutrophils that transmigrated through the positively haptotactic membrane (~50%) is higher than that counted from the negatively haptotactic membrane (~5%). While these data suggest that the presence of haptotaxis has occurred, confirmation of this would require direct observation of both guided migration and the presence of an immobilized gradient.

With recent advancements in microfluidic technology, immobilized gradients with different steepness and mean level of surface density can be more consistently created on glass substrates by manipulating the flow of solutes [13, 14]. We adopt the same technology to generate gradients of IL-8 and ICAM-1. To ensure that the molecules are accessible to the cell surface, the biologically active molecules are extended and oriented on the glass surface through the use of protein G and IgG. In this approach, protein G is first adsorbed onto the glass substrate through passive adsorption, then IgG that recognizes the specific ligand or receptor is introduced and is bound to protein G. The use of IgG as a linker is widely applicable for a number of different proteins. In addition, the

linker-extended IL-8 may better mimic the physiological representation of the IL-8 bound on the endothelial glycocalyx.

4.3 Materials and Methods

4.3.1 General Strategies for Immobilizing a Protein Gradient

We immobilized a gradient of protein onto glass substrates using different combinations of physicochemical linkages, including adsorption, protein/protein interaction, and covalent bonding. The key strategy is to first create a soluble gradient to bias the attachment of proteins onto the glass substrate. The protein of interest (IL-8 or ICAM-1) can be adsorbed directly or extended from the substrate using specific linkers. In the latter instance, a gradient of base proteins, such as protein G or avidin, was first immobilized onto the substrate through simple adsorption. Linkers that specifically bind to the base proteins, such as IgG chimera or biotinylated-polymer, were then introduced to bind IL-8 or ICAM-1.

4.3.2 Cleaning of Glass Substrate

We used 24 mm x 40 mm No 1.5 cover glasses (Corning Inc., Corning, NY) as the substrates for protein immobilization. First, organic residues on the cover glasses were removed through an immersion in Piranha solution (a 3:1 mixture of sulfuric acid (H_2SO_4) and hydrogen peroxide (H_2O_2)) for five minutes. The cover glasses were then washed with deionized water (DiH_2O) and sonicated for 30 min to remove macro- and micron-

sized debris in a bath ultrasonicator (Branson B5510, Branson Ultrasonics, Danbury, CT). To reduce the formation of water residues during drying, the sonicated cover glasses were rinsed in ethanol (70%) and shelved onto a stainless steel holder. The holder with the cover glasses was covered in aluminum foil and left to dry in a convection oven (75 °C) for at least 20 min.

4.3.3 Estimating the Protein Concentration Required for Surface Saturation

We approximated the adsorbed proteins as a monolayer of spheres in hexagonal close packing. As such, the maximum number of proteins that can be packed into an area A is:

$$N_{\max} = \frac{A}{2\sqrt{3}\cdot r^2} \qquad (4.3.1)$$

where r is the radius of the protein.

Given a rectangular channel with dimensions of l (length) × w (width) × h (height), the total surface area is:

$$A_{surf} = 2\left(lw + lh + wh\right) \qquad (4.3.2)$$

The total number of proteins that can be adsorbed onto the inner walls of the rectangular channel is obtained by substituting Eqn 4.3.2 into Eqn 4.3.1:

$$N_{surf,\max} = \frac{lw + lh + wh}{\sqrt{3}\cdot r^2} \qquad (4.3.3)$$

The total number of soluble proteins within the rectangular channel is:

$$N_{sol} = c_s \left(l \cdot w \cdot h \right) \qquad (4.3.4)$$

where c_s is the soluble concentration of protein in the unit of mol/L. Assuming the substrate is smooth and the surface binding is irreversivble, as long as $N_{sol} > N_{surf,max}$ the substrate will be fully occupied by the proteins given sufficient time (see Section 4.3.7).

4.3.4 Determining the Protein Concentration Required for Surface Saturation

We varied the incubation concentration of different proteins to assess their binding affinity to the glass substrate. Once the fluorescence of the labeled proteins no longer increases, we defined the level of protein saturation to be 100%. To ensure that the discontinued increase in fluorescence is not due to the lack of labeling antibody, we duplicate the substrate sample coated with the highest incubation concentration but labeled with twice the concentration of labeling antibody to insure that there is no further increase in fluorescence. In the case of IgG binding to protein G, we also determined the rate of binding directly using fluorescent IgG.

4.3.5 Creating a Soluble Protein Gradient

The flow-mixing gradient generator described in Chapter 1 and Chapter 2 [15] was used to generate the soluble gradient. Essentially two flow streams, each carrying a different solute concentration, were merged and split successively to form new flow streams that carry the intermediate concentrations. After the flow with the different solute concentrations merge in the main channel downstream, a soluble gradient that spans across several cell body lengths is formed. Details on the fabrication of the flow-mixing

gradient generator are described in Section 2.3.2 of Chapter 2.

4.3.6 Determining the Optimal Flow Rate for Gradient Immobilization

We tested flow rates of 0.25, 0.50, 1.0, and 2.0 μL min^{-1} (0.16, 0.33, 0.66, 1.33 mm/sec through the 500 μm x 50 μm channel) to fine-tune the steepness of the immobilized gradient. The density profiles of immobilized gradients were measured with either 20 or 50 μg/mL of fluorescent labeling antibody.

4.3.7 Modeling of Gradient Immobilization

We used the analytical model described by Jiang et al. to predict the time rate of gradient adsorption in the flow-mixing gradient generator [14]. In this model, protein adsorption is assumed to be purely reaction-limited and follows the governing kinetics of bimolecular reaction:

$$\frac{dc_s(t)}{dt} = k_f c\left[c_{s,sat} - c_s(t)\right] - k_r c_s(t) \qquad (4.3.8)$$

where c is the solute concentration. $c_s(t)$ and $c_{s,sat}$ are the surface density of bound protein and the maximal surface density that is obtained at surface saturation, respectively, and both have the unit of mol/m^2. The term $[c_{s,sat} - c_s(t)]$ represents the surface density still available for binding. k_f and k_r are the rate constant of adsorption and desorption, respectively.

After integrating Eqn. 4.3.8 and imposing the initial condition that the surface is completely unoccupied ($c_s(0) = 0$), we have:

$$c_s(t) = \frac{k_f c_{s,sat} c\left[1 - e^{-(k_f c + k_r)t}\right]}{k_f c + k_r} \qquad (4.3.9)$$

Since protein adsorption is generally irreversible cf [16], k_r reduces to zero:

$$c_s(t) = c_{s,sat}\left[1 - e^{-k_f ct}\right] \qquad (4.3.10)$$

Taking the natural logarithm of Eqn 4.3.10 on both sides and rearranging, an expression that allows the determination of k_f is obtained:

$$k_f = -\frac{ln\left[1 - c_s(t)/c_{s,sat}\right]}{ct} \qquad (4.3.11)$$

The flow-mixing gradient generator provides a convenient means to determine the value of k_f with just one substrate coating. Since a time-steady soluble gradient is created, a different part of the substrate would see a different solute concentration (c). At a properly chosen time point, part of the coated substrate will be at 100% surface saturation, and this allows us to determine the values of $c_s(t)/c_{s,sat}$. Since c, $c_s(t)/c_{s,sat}$, and t are known, k_f can be determined through least-square regression.

Since the protein of interest will eventually saturate the entire substrate, leading to a loss of the adsorbed gradient, the protein of interest is often competed against a non-interacting protein in the adsorption to the substrate. In this manner, an immobilized protein gradient will be maintained even at full surface saturation. Assuming the two competing protein species are comparable in size, their competitive bindings to the substrate can be generalized as:

$$\frac{dc_{s,A}(t)}{dt} = k_{f,A}c_A\left[c_{s,sat} - c_{s,A}(t)\right] - k_{r,A}c_{s,A}(t) \qquad (4.3.12)$$

$$\frac{dc_{s,B}(t)}{dt} = k_{f,B}c_B\left[c_{s,sat} - c_{s,B}(t)\right] - k_{r,B}c_{s,B}(t) \qquad (4.3.13)$$

which with irreversible adsorption (both $k_{r,A}$ and $k_{r,B} = 0$) reduces to:

$$\frac{dc_{s,A}(t)}{dt} = k_{f,A}c_A\left[c_{s,sat} - c_{s,A}(t) - c_{s,B}(t)\right] \qquad (4.3.14)$$

$$\frac{dc_{s,B}(t)}{dt} = k_{f,B}c_B\left[c_{s,sat} - c_{s,A}(t) - c_{s,B}(t)\right] \qquad (4.3.15)$$

Thus given the concentration profile of soluble gradient and known values of k_f for both protein species, the density profile of the adsorbed gradient can be predicted at different time points.

4.3.8 Immobilization of ICAM-1 Gradient via IgG Chimera

First, the inner walls of the microfluidic device were incubated with 100 μg/mL of protein G (CalBiochem, La Jolla, CA) for 30 min. Recombinant human ICAM-1 extended with the Fc segment of IgG (33 μg/mL) (R&D Systems, Minneapolis, MN), abbreviated as Fc-ICAM-1, was competed against 33 μg/mL of mouse IgG (Sigma-Aldrich, St. Louis, MO) for the binding to protein G in a flow of 0.17 mm/sec for 4 hr. When a shallower gradient of Fc-ICAM-1 is desired, we decreased the coating concentration of Fc-ICAM-1, but added more mouse IgG to maintain a total protein concentration of 33 μg/mL to compete against the 33 μg/mL of mouse IgG. Since the fluorescent antibody used to label the Fc-ICAM-1 will compete with the Fc-ICAM-1 in the binding to protein G, we covalently bond the Fc-ICAM-1 to protein G. This is achieved by introducing into the device 5.4

mg/mL of dimethyl pimelimidate (DMP), which is a homobifunctional crosslinker that binds the free amino groups. Between each coating incubation, the substrates were washed three times with PBS (pH 7.4) to remove remnant reagents. Prior to DMP crosslinking, the substrates were primed/washed with 200 mM triethanolamine. After DMP crosslinking, the substrates were washed three times with 50 mM Tris (pH of 7.5) to lower the pH, thereby terminating the DMP crosslinking. With the exception of DMP, which is diluted in 200 mM triethanolamine, all reagents were diluted in pH 7.4 PBS. All coating incubations were static (no flow) and performed at room temperature unless specified otherwise.

4.3.9 IL-8 Gradient Immobilization via Anti-histidine-tag IgG Linker

The protocol for immobilizing a gradient of IL-8 is similar to that for the ICAM-1 gradient described in Section 4.3.8. After 30 min of coating incubation with 100 μg/mL of protein G, 20 μg/mL of IgG with anti-histidine-tag (Merck KGaA, Darmstadt, Germany), abbreviated as α-ht-IgG, was competed against 20 μg/mL of Fc-ICAM-1 for the binding to protein G under flow (mean velocity = 0.17 mm/sec) for 4 hr. Sometimes DMP-crosslinking is performed to ensure the fixation of α-ht-IgG to protein G. Recombinant IL-8 with mucin-stalk extension and histidine-tag ending (R&D Systems, Minneapolis, MN), abbreviated as ht-IL-8, was then introduced at a concentration of 10 μg/mL for the binding to α-ht-IgG for 1 hr at room temperature, then continued overnight in 4°C. Prior to each neutrophil migration experiment, 2 mg/mL of BSA was introduced to block any potentially uncoated sites for at least 1 hr, followed by washing/priming

with HBSS++.

4.3.10 Immobilization of IL-8 Gradient via PEG Linker

Avidin (200 μg/mL) was competed against BSA (200 μg/mL) under flow (mean velocity = of 0.88 mm/sec) to form an immobilized avidin gradient. Polyethylene glycol (PEG) linker with biotin on one end and N-Hydroxysuccinimide (NHS) group on another (Nanocs Inc., Boston, MA), abbreviated as biotin-PEG-NHS, was then introduced at a concentration of 6 mg/mL for the binding to avidin for 30 min. IL-8 (10 μg/mL) (R&D Systems, Minneapolis, MN) was then introduced for the binding to biotin-PEG-NHS for 1 hr, and continued overnight in 4 °C. Prior to the introduction of biotin-PEG-NHS, the substrates were washed/primed three times with 50mM citrate phosphate buffer (pH of 4.9) to lower the pH of the system. The lowering of pH reduces the likelihood of NHS reacting directly with avidin and BSA. Likewise, the biotin-PEG-NHS is diluted in 50mM citrate phosphate buffer (pH 4.9). After the introduction of biotin-PEG-NHS, the substrates were washed/primed with pH 8.4 PBS to promote the reaction between NHS and the primary amines on IL-8. Likewise, the IL-8 to be covalently bound to the NHS was diluted in pH 8.4 PBS. Unless otherwise mentioned, all reagents were diluted in pH 7.4 PBS, and all substrates were washed three times with pH 7.4 PBS between different coating incubations. All coating incubations after the initial competition between avidin and BSA were static (no flow) and performed at room temperature.

4.3.11 Activation Control for Non-specific Cell Activation

To assess the specificity with which the different substrate coatings activate neutrophils,

we observe the morphology and the adhesion of the neutrophils on the coated substrates for at least five min under static incubation. This is performed for the substrate coatings with BSA, ICAM-1, or IL-8 alone or in combinations with protein G, avidin, IgG, α-ht-IgG, or biotin-PEG-NHS linker. Because non-specific activation occurs more frequently at 37°C, the neutrophil activation control experiments were all conducted at room temperature (~25°C).

4.3.12 Analysis of Cell Migration

Cell migrations were recorded at 4 frames per minutes (4 fpm) under a phase contrast microscope at a total magnification of 200X. The migratory paths of cells were either tracked manually or automatically with a custom-written MATLAB program (MathWorks, Inc., Natick, MA). The migration data from each experiment consisted of all cells tracked from a microscopic field of view (~100-300 cells depending on the cell seeding density). All cells that traveled for times less than 12 frames (3 min) or less than 30 μm in displacement (~3 cell body lengths) were considered non-active and excluded from the analysis. Base on the migratory paths, we determined the following metrics to characterize cell migration:

- *Displacement*: the direct distance between the starting and the ending position of a cell's migratory path.
- *Direction of migration*: the angle of the vector defined by the displacement of a cell, which ranges from 0° to 360°.
- *Pathlength*: the total distance traveled by a cell.

- *Speed*: the pathlength divided by the time the cell spent migrating.
- *Persistence Index* (PI): the ratio of displacement to pathlength.
- *Directionality Index* (DI): the ratio of the component of displacement along the principal axis of the density gradient to the pathlength. DI can be either positive or negative. We defined the DI to be positive if the cell migrated toward the direction of higher surface density.
- %+DI: the percentage of cells with positive DI.

We defined a cell population to be migrating directionally if its %+DI is statistically different from the %+DI of the control migration conducted on uniform substrates (using the two-tailed student's *T*-test at the alpha level of 0.05, assuming unequal variances).

4.4 Results and Discussion

4.4.1 Rate of Protein Binding to the Substrate and Full Surface Saturation

For all immobilization procedures, we use the ratio of N_{sol}:$N_{surf,max}$ (Eqn 4.3.3 and Eqn 4.3.4) to estimate the solute concentration required for a full surface saturation. Consistent with Eqn. 4.3.10, we noted that the time required for full surface saturation is inversely proportional to the solute concentration. For instance, when the solute concentration is halved, a doubling in the coating duration is necessary to achieve the same level of surface saturation. We also noted that the binding of the protein to the glass substrate or to the linker tends to be reaction-limited. We believe this is the case because for a period of one minute, most of the molecules had characteristic diffusion distances comparable to the height of the chamber (50 μm). A full surface saturation generally required ~30 min in our experiments, indicating that the process was not limited by diffusion (see Section 4.7). Based on a reaction-limited model (Eqn. 4.3.11), we found that the rates of protein binding onto the glass substrate are generally on the order of 10^4/M·sec, consistent with those reported by Jiang et al. [14]. Since the maximum intensity of the fluorescence labeling is quite consistent in all our experiments, we generally report surface density in terms of percentages (100% = maximum intensity) for easy comparison between studies.

4.4.2 Adjusting the Steepness of the Immobilized Gradient

We investigated the effects of different coating flow rates on the steepness of the adsorbed protein gradient and found that a flow of ~0.25-0.5 μL/min (mean velocity

~0.09-0.17 mm/sec through the 500 μm × 50 μm channel) allowed the formation of an adsorbed gradient that is mostly linear across the 500-μm span of the cell-hosting space (Fig. 4.1). At faster flow rates (1.0 μL/min or more), steeper gradients were formed, but flanked by notable plateaus of surface density minimum and maximum on both sides. The observation that faster flow rate increased the steepness of the immobilized gradient is in agreement with previous reports from the literature [15, 17].

4.4.3 Confirming that IgG Linkers do not Activate Neutrophils

To ensure that non-specific activation of the neutrophils on the coated substrates does not mitigate (or inhibit) haptotaxis, we monitored the morphology of the neutrophils that settled on the coated substrate for at least 5 min (Fig. 4.2). Since we always noted a small

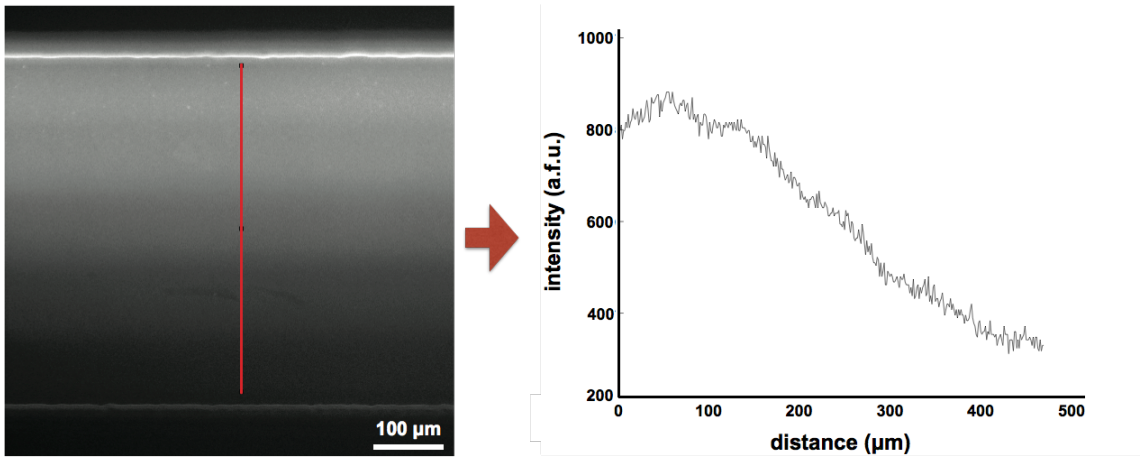

Figure 4.1: Example of the IgG gradient immobilized on protein G. The substrate was incubation coated with 100 μg/mL of protein G for 30 min, followed by the perfusion of soluble IgG gradient for 4-hr (fluorescent v.s. non-fluorescent IgG, both at 33 μg/mL). Left: The immobilized gradient. Right: Corresponding line-scan, which indicates a ramping of surface saturation from 0% to 100% over a 500-μm span.

basal level of nonspecific activation at 37 °C, we conducted this set of control experiments at room temperature to increase the contrast in cell state (activated vs unactivated). In all instances, only under the presence of ht-IL-8 (Fig. 4.2c & Fig. 4.2d) did the neutrophils assume their activated, spread-out morphology. These results indicate that the immobilized ht-IL-8 retained its ability to activate neutrophils, and that the presence of protein G and the bound IgG (Fc-ICAM-1 and α-ht-IgG) does not induce any nonspecific activation (Fig. 4.2b).

4.4.4 Determining the Optimal Surface Saturation of ICAM-1 for Haptotaxis

We first identified the level of ICAM-1 surface saturation that optimally supports neutrophil motility. While keeping the same total IgG concentration (33 μg/mL), we competed different concentrations of Fc-ICAM-1 against a mouse-derived IgG in the binding to protein G. Since the Fc-ICAM-1 and the mouse IgG bind with similar affinity to protein G, the percentage of ICAM-1 surface saturation can be estimated based on the fraction of Fc-ICAM-1 used (*e.g.*, 17 μg/mL of Fc-ICAM-1 and 17 μg/mL of mouse-IgG together produce a 50% ICAM-1 saturated substrate). We monitored neutrophil migrations on the substrate saturated with 0.5%, 5%, and 50% ICAM-1 under physiological flow (0.4 dyn/cm^2) and 10 nM fMLP (uniform) and statistically compared the motility parameters (Section 4.3.12) obtained from each substrate (Fig. 4.3) using student's *T*-test (two-tailed, alpha level of 0.05, assuming unequal variances). The presence of cell activator (*i.e.*, fMLP) is necessary because Fc-ICAM-1 alone does not induce any migration (cf. Fig. 4.2b). We also introduced flow to provide the

physiological shear stress that the neutrophils would normally experience during luminal migration. We observed that while there were no significant differences in the migration speed of the neutrophils on the different substrates, the start-to-end distances (displacements) traveled by the neutrophil were significantly higher on the 5% ICAM-1 saturated substrate (mean = 87 μm) in comparison to the 60 μm and 47 μm surveyed from the 0.5% and 50% ICAM-1 saturated substrates. These data indicate that a 5% surface saturation of ICAM-1 promoted higher migratory motility. We also created a reference for directed migration by conducting neutrophil migration in the presence of a soluble gradient of fMLP on the 5% ICAM-1 saturated substrate.

We defined the directionality index (DI) to indicate the faithfulness of each cell in migrating toward the higher surface density of ICAM-1 (Section 4.3.12). If a cell migrates toward the higher surface densities, we defined the DI to be positive. As expected, the percentage of neutrophils with positive DI (%+DI) in the control of directed migration (promoted under a soluble fMLP gradient, Fig. 4.4a) is significantly higher than those obtained from the migrations on uniform ICAM-1 (Fig. 4.3a, Fig. 4.3b, and Fig. 4.3c) under the evaluation of student's *T*-test (two-tailed, alpha level of 0.05, assuming unequal variances). Interestingly, there are no significant differences in migratory speed for all comparisons (Fig. 4.4b).

4.4.5 Neutrophil Migrations on the Immobilized ICAM-1 Gradients

As our first effort to promote an ICAM-1-mediated haptotaxis, we immobilized gradients that centered around the optimal ICAM-1 surface saturation (5%) across the

500-μm span of our cell-hosting space. We also performed control studies for "haptokinesis" on substrates that are coated uniformly with 5% ICAM-1. Both sets of migrations were subjected to flow that provide physiological shear stress (0.4 dyn/cm^2). Comparisons of all motility parameters from the gradient-coated (n = 7) and the uniformly-coated (n = 6) substrates indicate that there are no statistically significant differences (Fig. 4.5). The immobilized gradients (0-10%/500-μm) therefore did not promote any neutrophil haptotaxis, despite the fact that the mean level of 5% ICAM-1 surface saturation is optimal for neutrophil motility. A representative migration of the gradient-coated and the uniformly-coated substrates is also given in Fig. 4.6 for a visual appreciation of the cell tracking. In our subsequent efforts, we considered the scenario in which the ICAM-1 gradient is steep. We chose a characteristic distance based on the size of endothelial cells (length ~100 μm) and immobilized gradients that ramp from 0-100% over a 150-μm span at the center of the cell-hosting space (Fig. 4.7a). The cells that migrate on the steep gradient are categorized as the experimental group of interest. Flanking each side of the steep gradient is the plateau of surface density maximum (100% ICAM-1) and minimum (0% ICAM-1) (Fig. 4.7a). The cells that migrate on these plateaus serve as the built-in controls for haptokinesis. We compared the %+DI measured from the steep gradient (0-100%/150-μm, n = 4) and the haptokinesis controls (0% and 100% uniform pooled together, n = 4) and again did not detect any significant difference (Fig. 4.7b).

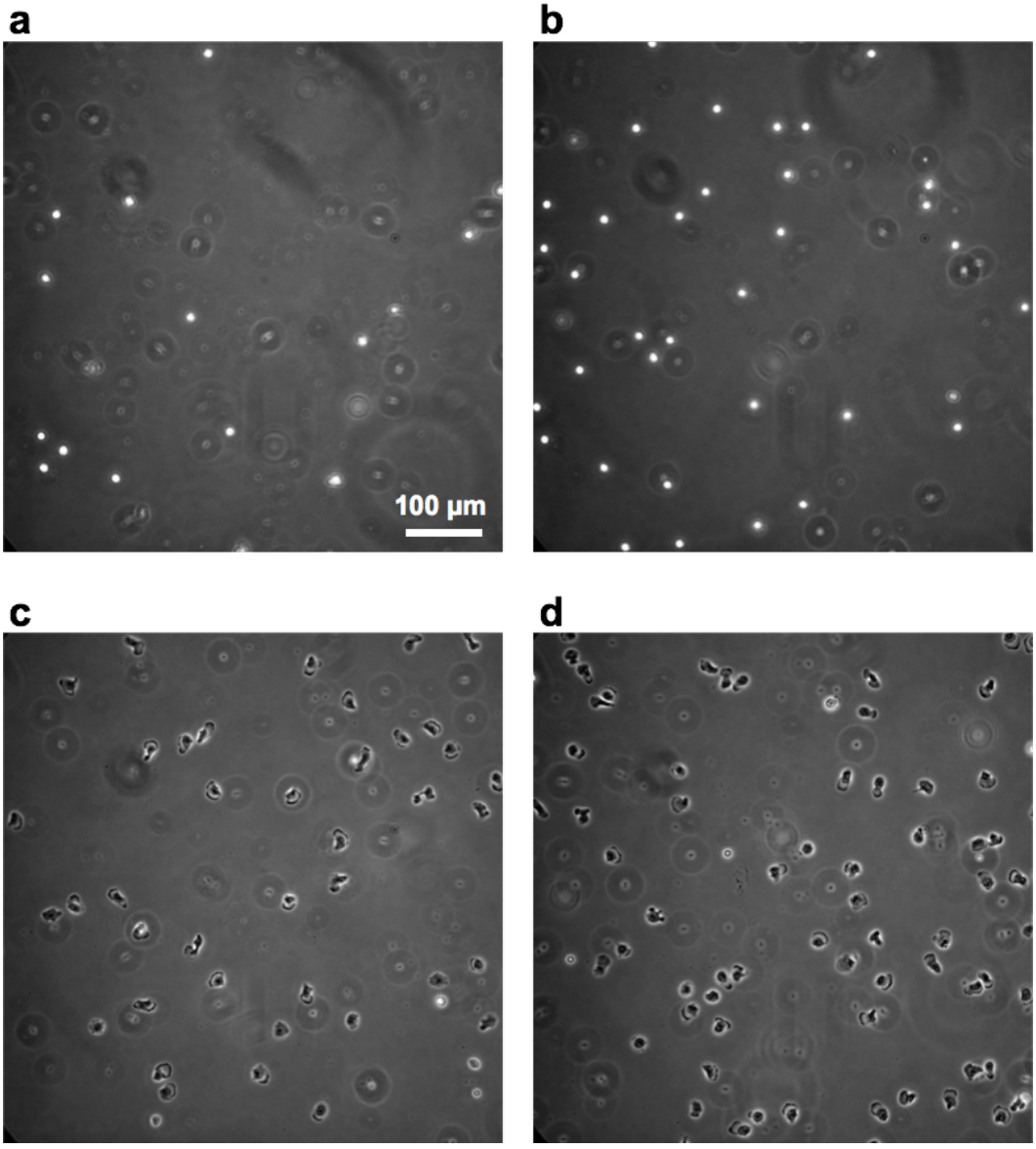

Figure 4.2: Neutrophil activation on substrates coated using the IgG linker. a. Simply adsorbed BSA. **b.** Protein G + Fc-ICAM-1+ α-ht-IgG. **c.** Protein G + α-ht-IgG + ht-IL-8. **d.** Protein G + Fc-ICAM-1 + α-ht-IgG + ht-IL-8. As expected, when the substrate is clean, the neutrophils do not activate on the adsorbed BSA (a). The neutrophils retained their unactivated, spherical morphology on the immobilized Fc-ICAM-1 (b), indicating that protein G and the bound IgG do not nonspecifically activate the neutrophils. Only when the ht-IL-8 was present, as in (c) and (d), did the neutrophils assume their activated, spread-out morphology. These activation controls also indicate that the IL-8 immobilized using the histidine-tag linkage retains its ability to activate the neutrophils.

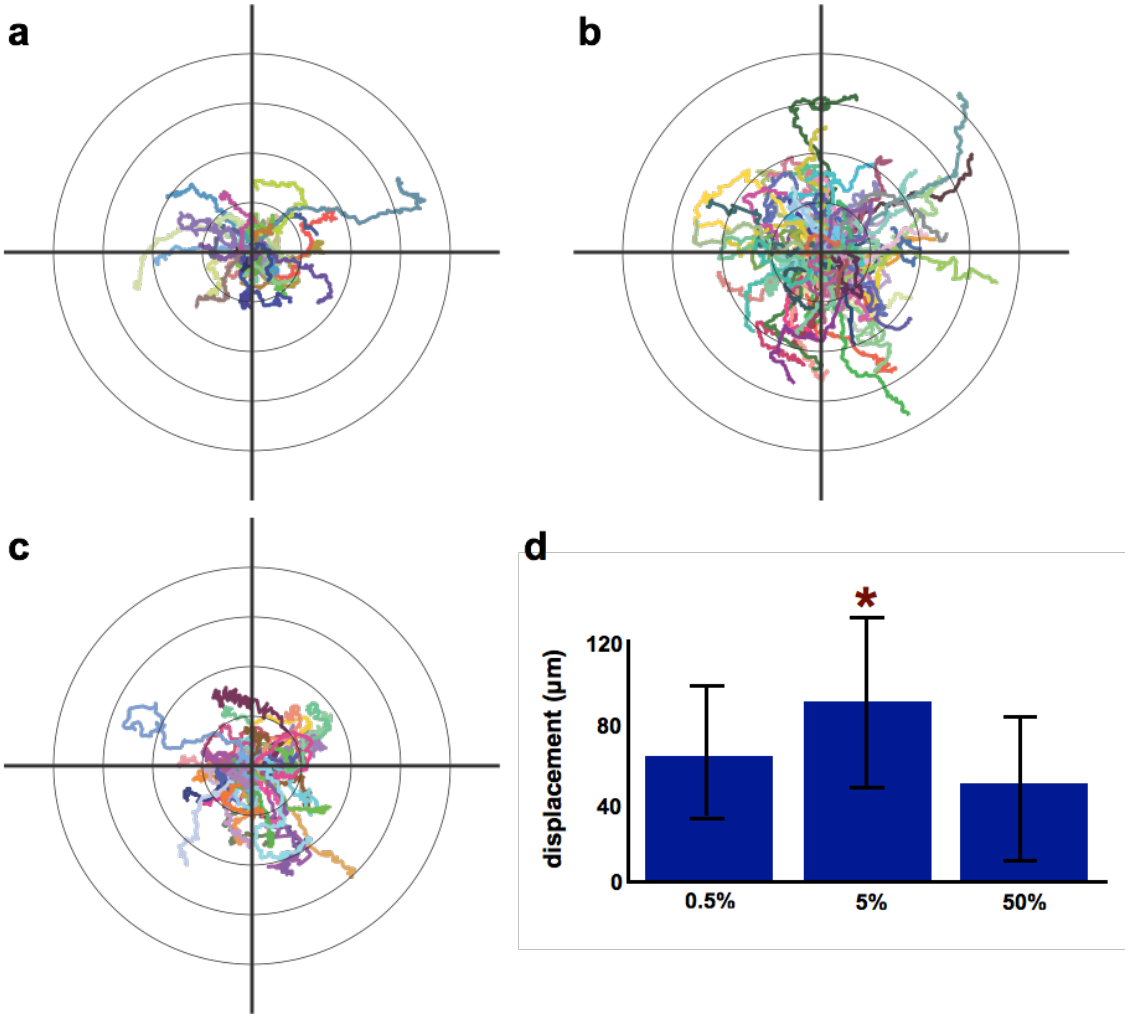

Figure 4.3: Neutrophil migrations on uniform ICAM-1. a. 0.5% saturated substrate, **b.** 5% saturated substrate, **c.** 50% saturated substrate. The starting point of the migratory path of each neutrophil is repositioned at the origin of the radial graph. The distance between the neighboring concentric rings is 50 µm. **d.** Comparison of neutrophil displacements on a, b, and c. Student's *T*-test (two-tailed, alpha level of 0.05, assuming unequal variances) indicates that the displacements of neutrophils on the 5% saturated substrate (b) is significantly different from those on the 0.5% (a) and 50% saturated substrates (c). The error bar represents the standard deviation.

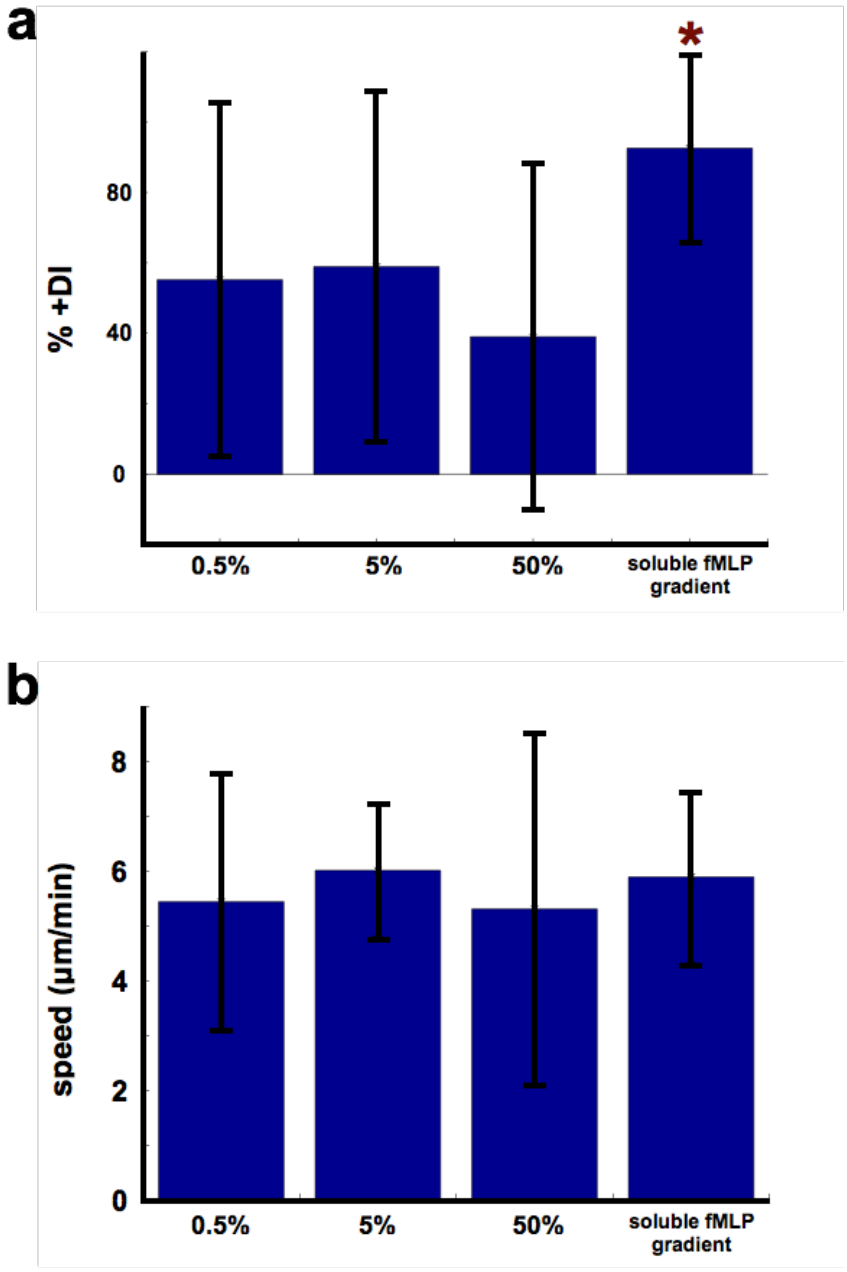

Figure 4.4: Comparison of chemotaxis and migrations on uniform ICAM-1. In terms of **a.** %+DI, and **b.** speed. While the chemotaxing neutrophils exhibited significantly higher values of %+DI (a) than the neutrophils migrating on 0.5%, 5%, and 50% ICAM-1 saturated substrate (uniform), no significant differences were found in the migration speed (b). The error bar represents the standard deviation. Student's *T*-test (two-tailed, alpha level of 0.05, assuming unequal variances) was used for the statistical comparisons.

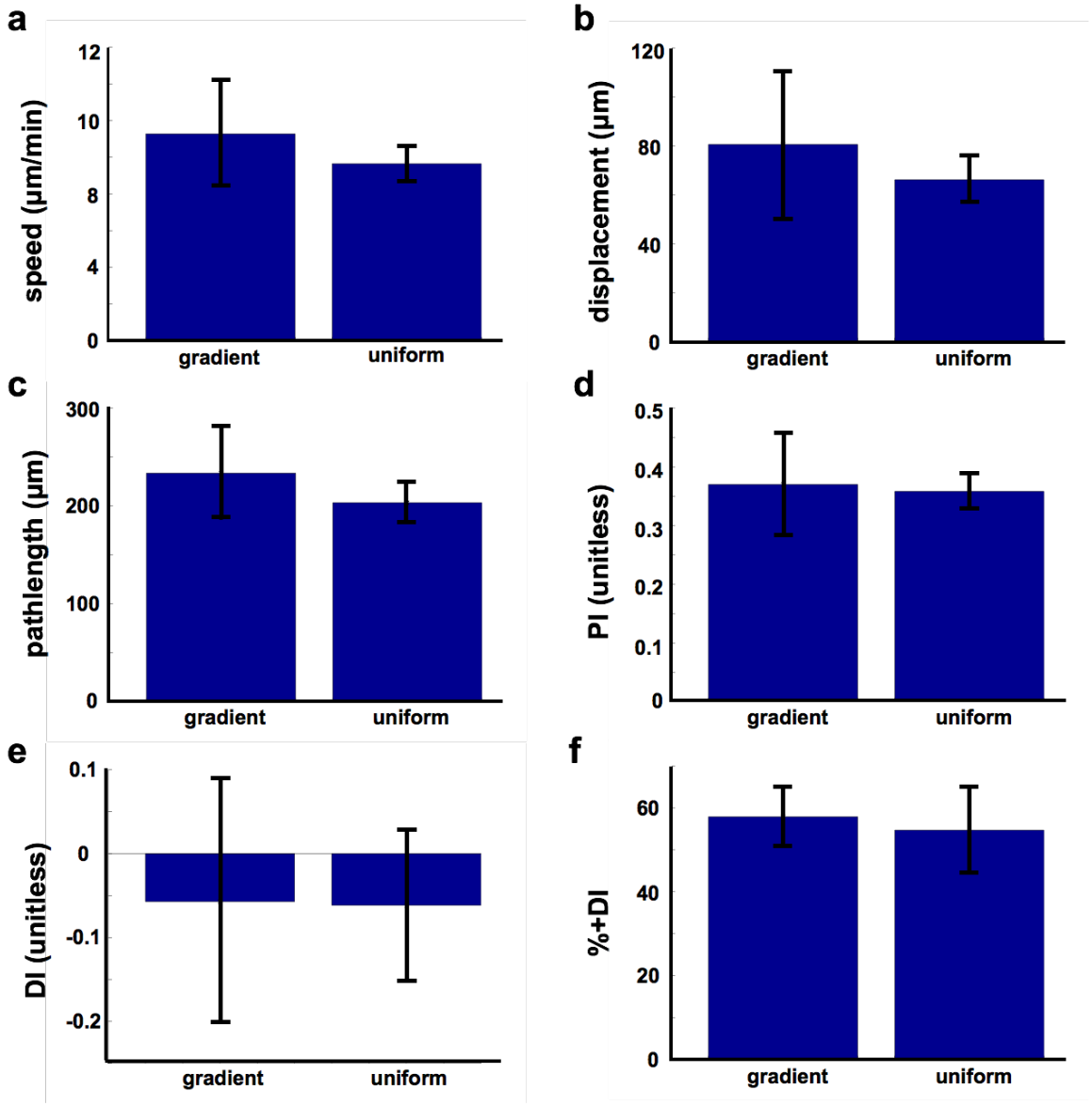

Figure 4.5: Comparison of neutrophil migration on ICAM-1 gradient (0-10%/500-μm) and uniform ICAM-1. In terms of of **a.** speed, **b.** displacement, **c.** pathlength, **d.** persistence index (PI), **e.** directional index (DI), **f.** percentage of cells that migrated in the direction of higher surface density (+%DI). No statistically significant differences were found between the gradient-coated (n = 7) and the uniformly-coated (n = 6) substrates for all the motility parameters tested (using two-tailed student's *T*-test at an alpha level of 0.05, assuming unequal variances). The error bar represents the standard deviation. These results, particularly the lack of difference in the %+DI, suggest that the immobilized ICAM-1 gradients (0-10%/500-μm) did not promote neutrophil haptotaxis.

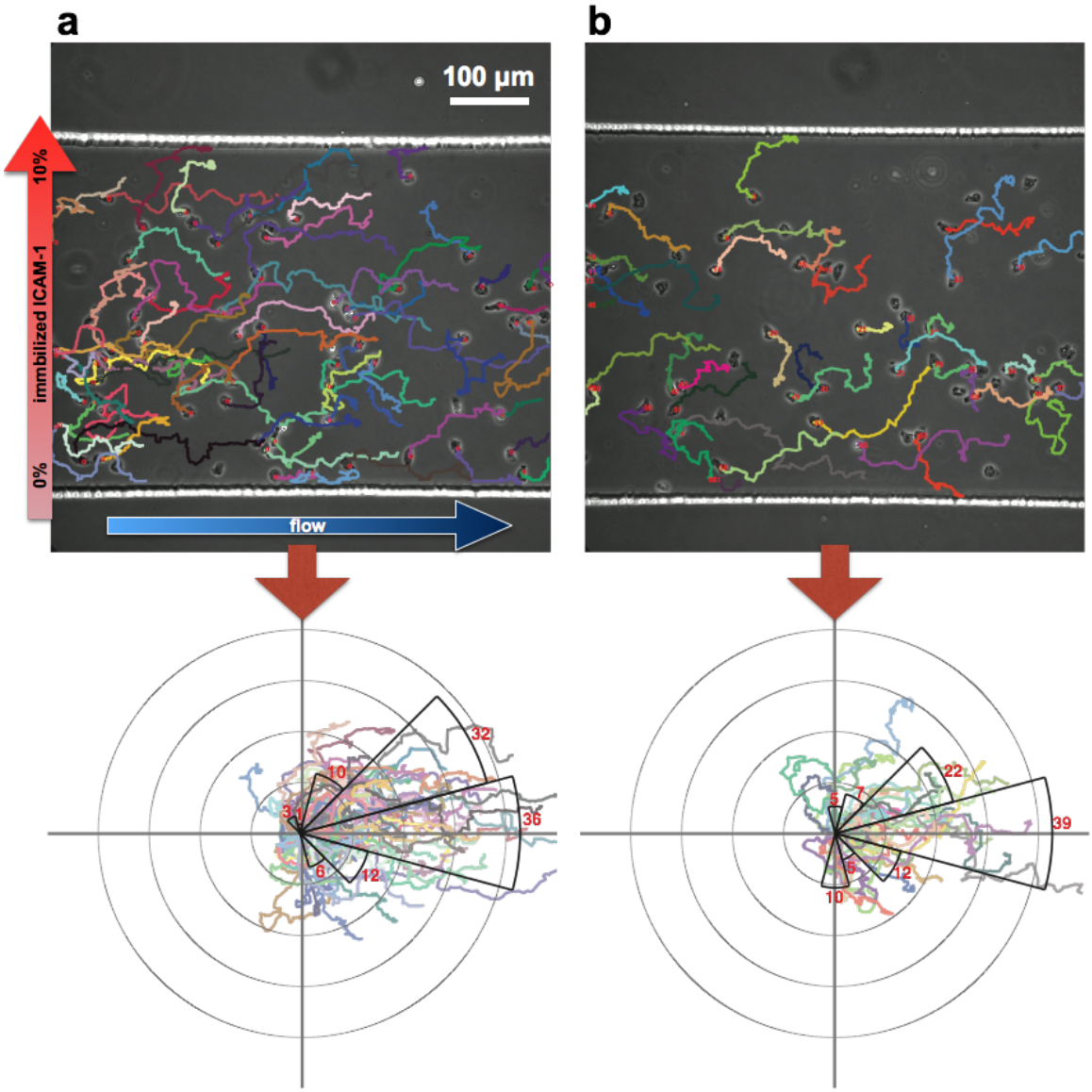

Figure 4.6: Representative neutrophil migrations on ICAM-1 gradient (0-10%/500-μm) and uniform ICAM-1. a. ICAM-1 gradient (0-10%/500-μm), **b.** uniform ICAM-1 (5%). The migratory path of each cell is assigned a random color, with the starting position denoted with a red open circle. Below each image of the cell tracking is a radial histogram that indicates the directionality of the migrating neutrophils. The red number and the size of the sector represent the percentage of cells that migrated into each sector on the polar plane. While the radial histogram in (a) did suggest that neutrophils exhibit a slight preference in the direction of the higher ICAM-1, no statistically significant difference is found when comparing the %+DI with the haptokinensis controls (Fig. 4.5f).

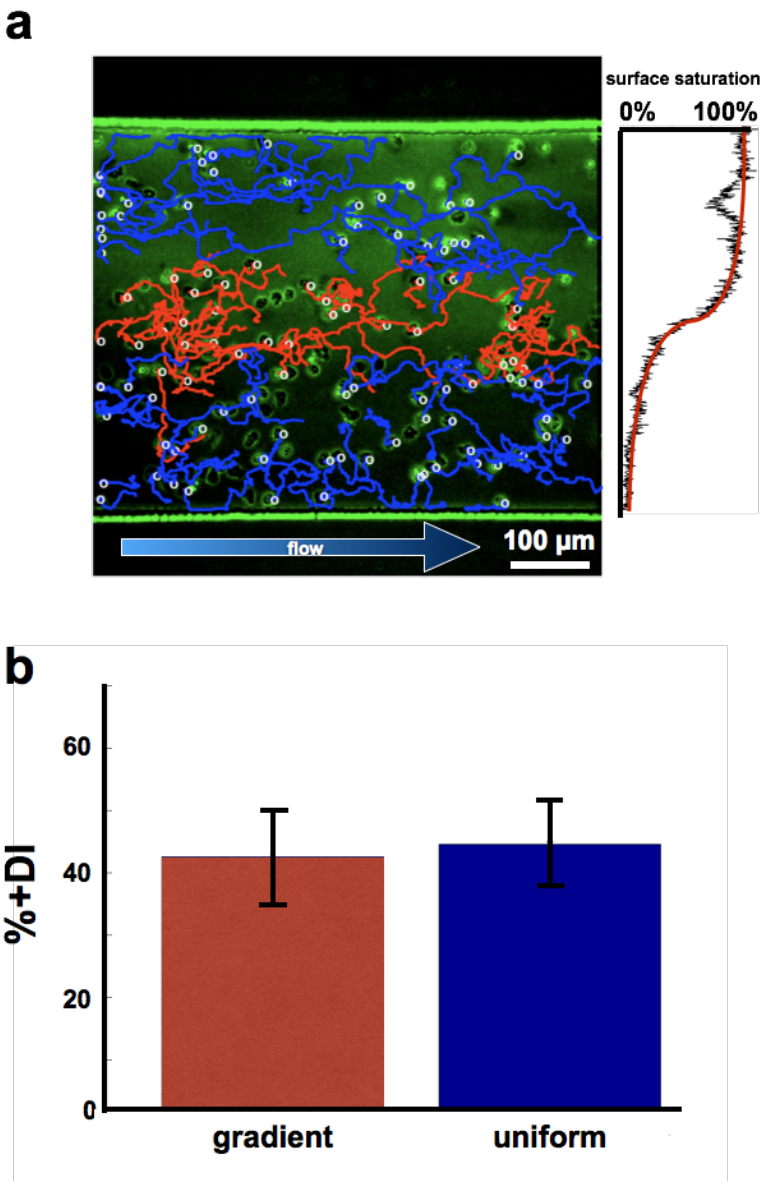

Figure 4.7: Neutrophil migrations on a steep ICAM-1 gradient (0-100%/150-μm). a. Representative cell trackings from one migration experiment, with the ICAM-1 labeling superimposed at the background. To the right is the line-scan showing the intensity profile of the labeled gradient. The tracks of cells that fall on the steep ICAM-1 gradient in the middle are marked in the red color. The tracks of cells that fall on the plateaus of surface density maximum at the top (100% ICAM-1) and the minimum at the bottom (0% ICAM-1) are pooled together to form the control group for haptokinesis, and marked in the blue color. **b.** Statistical comparison of the %+DI of the groups of cells that migrated on the steep ICAM-1 gradient (n = 4) and on the uniform ICAM-1 (n = 4) indicated that there is no significant difference. The error bar represents the standard deviation.

4.4.6 Detachment of immobilized ht-IL-8 at higher temperature

To immobilize IL-8 in a linker-extended form, we again used protein G as the base. While the IgG-conjugated form of IL-8 is not commercially available, the fractalkine-extended, histidine-tagged form of IL-8 (ht-IL-8) is. First, anti-histidine-tag IgG (α-ht-IgG) was competed against Fc-ICAM-1 in the binding to protein G to form an immobilized α-ht-IgG gradient (see Section 4.3.9). After cross-linking the bound IgG to protein G using DMP, the α-ht-IgG gradient was incubated with the ht-IL-8 to finalize an immobilized gradient of IL-8.

However, after conducting several migration experiments on the IL-8-coated substrates and failing to detect the presence of the IL-8 after labeling, we speculate that there is a detachment of the ht-IL-8 at 37°C (the temperature under which the migration experiments were conducted). To this end, we conducted control experiments using paired samples and varied the temperatures. Both samples are subjected to 45 min of 0.4 dyn/cm^2 flow to match the flow conditions of the migration experiments. Even after adding a burst (10 sec) of high flow (shear stress > 400 dyn/cm^2), a fluorescent gradient of the labeled IL-8 can be seen on the substrate kept at room temperature (Fig. 4.8a). However, for the substrate kept at 37°C, just the 45 min of 0.4 dyn/cm^2 flow alone led to the absence of a labeled gradient (Fig. 4.8b).

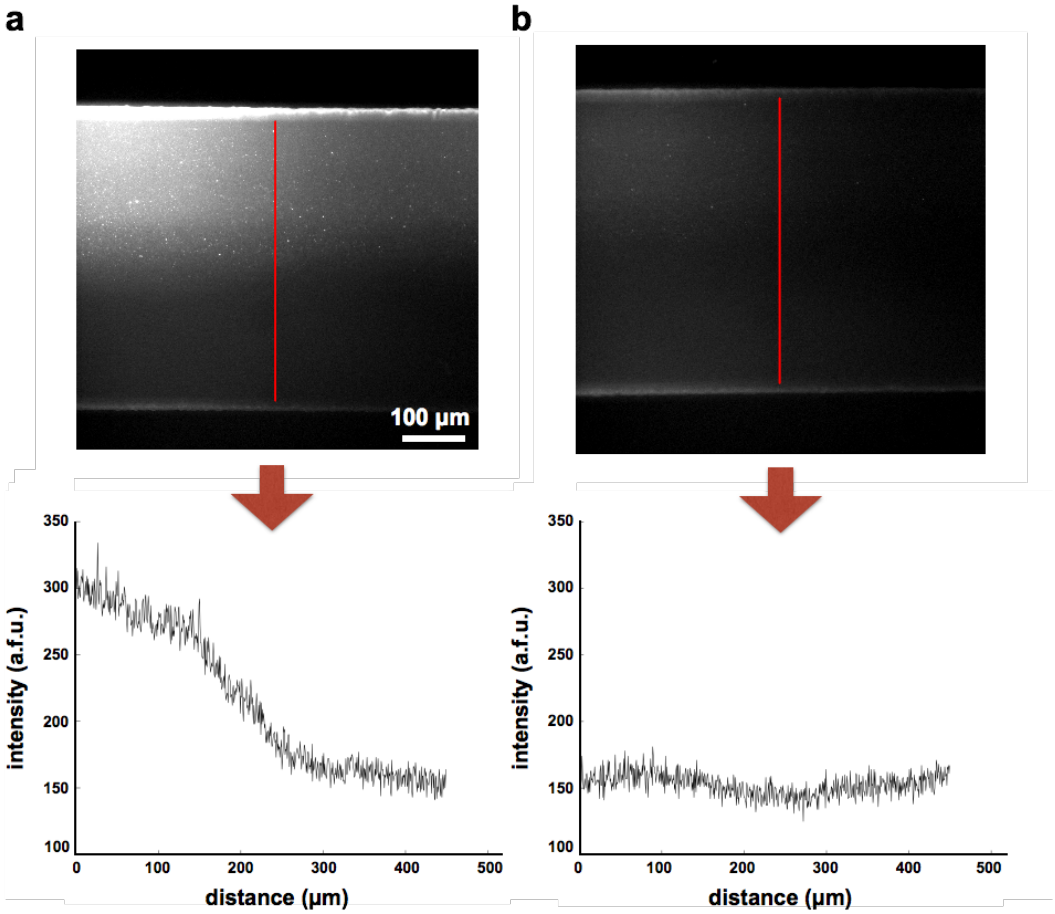

Figure 4.8: Detachment of ht-IL-8 at 37°C. The IL-8 gradients are immobilized using the histidine-tag, as described in Section 4.3.9. **a.** After 45 min of flow at 0.4 dyn/cm^2 at room temperature, followed by a burst (10 sec) of high shear (> 400 dyn/cm^2). **b.** After 45 min of 0.4 dyn/cm flow at 37°C. As indicated by the line-scans in the lower panels, an immobilized IL-8 gradient is retained in (a) but not in (b), suggesting that at 37°C, the ht-IL-8 detaches in the presence of flow.

4.4.7 Immobilization of IL-8 via biotin-PEG-NHS linker

As an initial work-around, we examined neutrophil migration on the IL-8 coated substrates at room temperature. However, in addition to the lack of directed migration, the neutrophils exhibited a substantial decrease in motility even in the presence of a

soluble fMLP gradient. Speculating that the higher thermokinetics at 37°C is conducive to directed migration, we devised an alternative, covalent bond-based linker chemistry to immobilize the IL-8 gradient. We replaced α-ht-IgG with biotin-PEG-NHS as the linker to bind IL-8 (Fig. 4.9). The biotin-PEG-NHS linker we used consists of a 37 nm-long polyethylene glycol (PEG) chain, with biotin on one end and N-Hydroxysuccinimide (NHS) group on another.

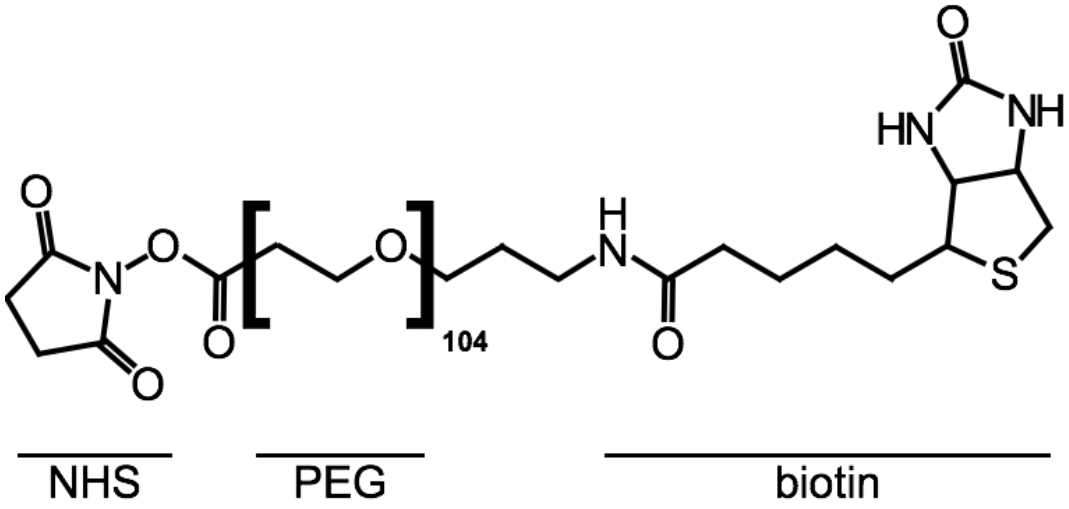

Figure 4.9: Molecular structure of the biotin-PEG-NHS linker (MW = 5 kDa). Conferred from the specifications provided by Thermo Fisher Scientific Inc., the length of each PEG monomer is 3.375 Å (MW = 44.0525 Da), and the combined length of the NHS-group and the biotin is 15.5 Å (MW = 412.46 Da). The 5 kDa biotin-PEG-NHS linker that we use therefore consists of ~104 monomers and ~37 nm in length.

Biotin binds specifically to the protein avidin, and the NHS will form a covalent bond with any primary amine ($-NH_2$) on a protein at a pH 8.5. A gradient of avidin was first immobilized through the competition against BSA in the binding to the glass substrate, followed by the coating incubation with biotin-PEG-NHS to create a gradient of NHS. Since it is possible that NHS will bond covalently to avidin and BSA, we

reduced the pH of the system by placing the biotin-PEG-NHS in a pH 4.9 citrate phosphate buffer (50 mM). The lower pH promotes the binding of biotin to avidin. Lastly, we hosted the covalent bonding of IL-8 to NHS in pH 8.5 PBS to finalize an immobilized gradient of IL-8.

4.4.8 Cell Activation and Surface Density Profiling of the PEG-linked IL-8

We noted that in comparison to the IL-8 immobilized using the IgG linker (cf. Fig 4.1), the IL-8 immobilized using the biotin-PEG-NHS linker exhibited lower mean level and steepness of fluorescence after labeling (Fig. 4.10). This is expected because depending on which primary amines on the IL-8 are covalently engaged by the NHS, the spatial orientation and the binding affinity of the labeling sites on the PEG-ylated IL-8 may differ. Despite the lower level of surface density and adhesion, we found that the PEG-ylated IL-8 activated all the neutrophils seeded (Fig. 4.11a). In contrast, all neutrophils maintained their unactivated morphology on BSA PEG-ylated using the same biotin-PEG-NHS linker chemistry (Fig. 4.11b). We also noted that in contrast to the gradients immobilized using the IgG linker, those immobilized using the biotin-PEG-NHS linker were less consistent in reproducing the same gradient profile (Fig. 4.10). Punctate spots of fluorescence aggregation were also frequently observed. To account for these inconsistencies, we always label the gradients after each migration experiment. In this way, we were able to pool samples with similar gradients profiles as a group to boost statistical power, and also retain the option to correlate the migration pattern to the local density profile of IL-8.

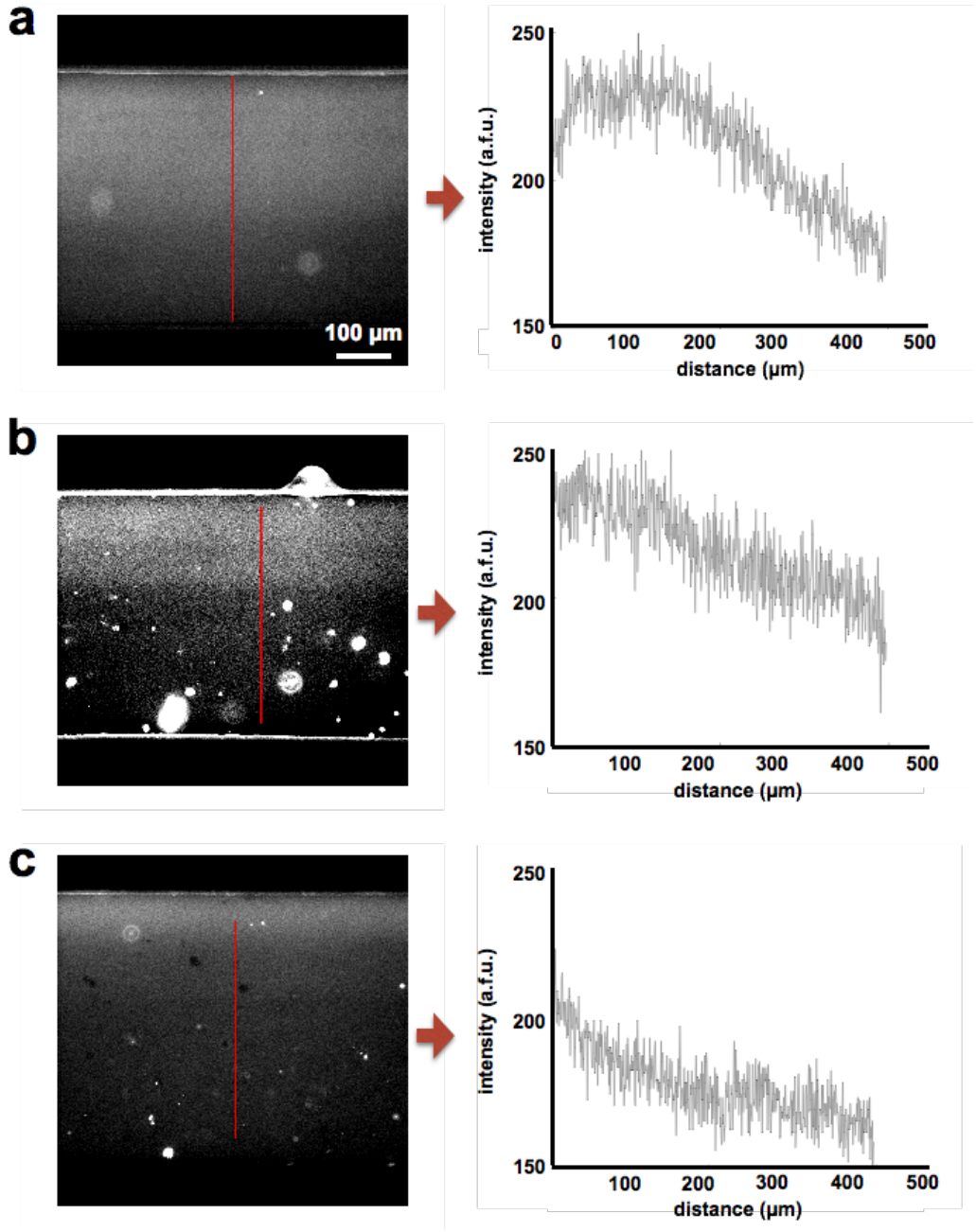

Figure 4.10: Examples of the IL-8 gradients immobilized using biotin-PEG-NHS linker. a., **b.**, and **c.** are all immobilized using the same coating procedures. As indicated by the line-scans, both the mean level and the steepness of the fluorescence labeling are less than those obtained from the IL-8 gradient immobilized using the IgG linker (cf. Fig 4.1). Furthermore, the fluorescence profiles are also more inconsistent in reproduction, and often accompanied by punctate aggregates.

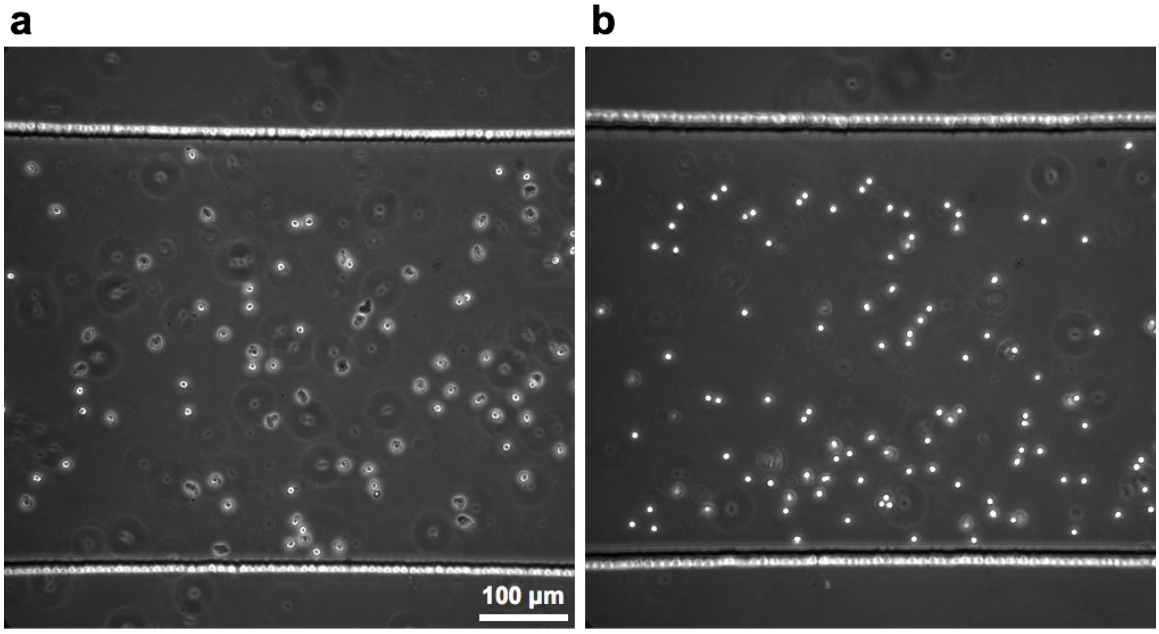

Figure 4.11: Neutrophil activation on the IL-8 immobilized *via* biotin-PEG-NHS linker. a. avidin + biotin-PEG-NHS + linked-IL-8. **b.** avidin + biotin-PEG-NHS + linked-BSA. The neutrophils activate on the PEG-linked-IL-8 (b), but not on the PEG-linked-BSA (a).

4.4.9 Neutrophil Migration on the Immobilized IL-8 Gradient

During the migration experiments, we noted that the neutrophils seeded on the PEG-ylated IL-8 are less adherent, possibly because the PEG-linkers partially shielded the BSA that served as adhesion sites for the neutrophils. As a countermeasure, we used higher concentration of neutrophils during the flow seeding to boost the number of adherent cells. We further noted that some neutrophils would stop their migration at locations that correspond to the sites of fluorescence aggregation. It is likely that these locations are sites of excess IL-8, which promoted the neutrophil to undergo a more phagocytic behavior, leading to the arrest in migration.

Applying the same methodology that we used to assess the presence of neutrophil haptotaxis on ICAM-1 gradients, we investigated how the different levels of PEG-ylated IL-8 affect neutrophil motility. Based on the coating concentrations used to study IL-8 haptotaxis in the literature (0.1, 1, and 10 μg/mL of IL-8) [12], we varied different concentrations of avidin (1, 10, and 100 μg/mL) against BSA (199, 190, and 100 μg/mL) in the binding to the glass substrate before introducing the PEG-linker and the 10 μg/mL of IL-8. However, comparison of neutrophil migration on these substrates indicated no significant differences in displacement (Fig. 4.12). Since the PEG-ylated IL-8 gradients are less consistent in reproduction, we decided to immobilized gradients in the visible range of fluorescence labeling so that we can always verify the density profile of the gradient *post hoc* (this corresponds to the substrate coated with 100 μg/mL of avidin and 100 μg/mL of BSA, which tends to yield the gradient profiles shown in Fig. 4.10a).

After conducting several migration experiments on the substrates coated using identical procedures, we pooled those with similar surface density profiles (n = 4) into a "gradient" group to boost statistical power. Again, the %+DI obtained from the gradient group is not statistically significantly different from the one obtained from the control studies on uniformly-coated IL-8 (n = 7) (Fig. 4.13). The migration experiments that were not pooled together (because each had have a different gradient profile) also do not have %+DI values or migratory patterns that indicate the presence of a directed migration.

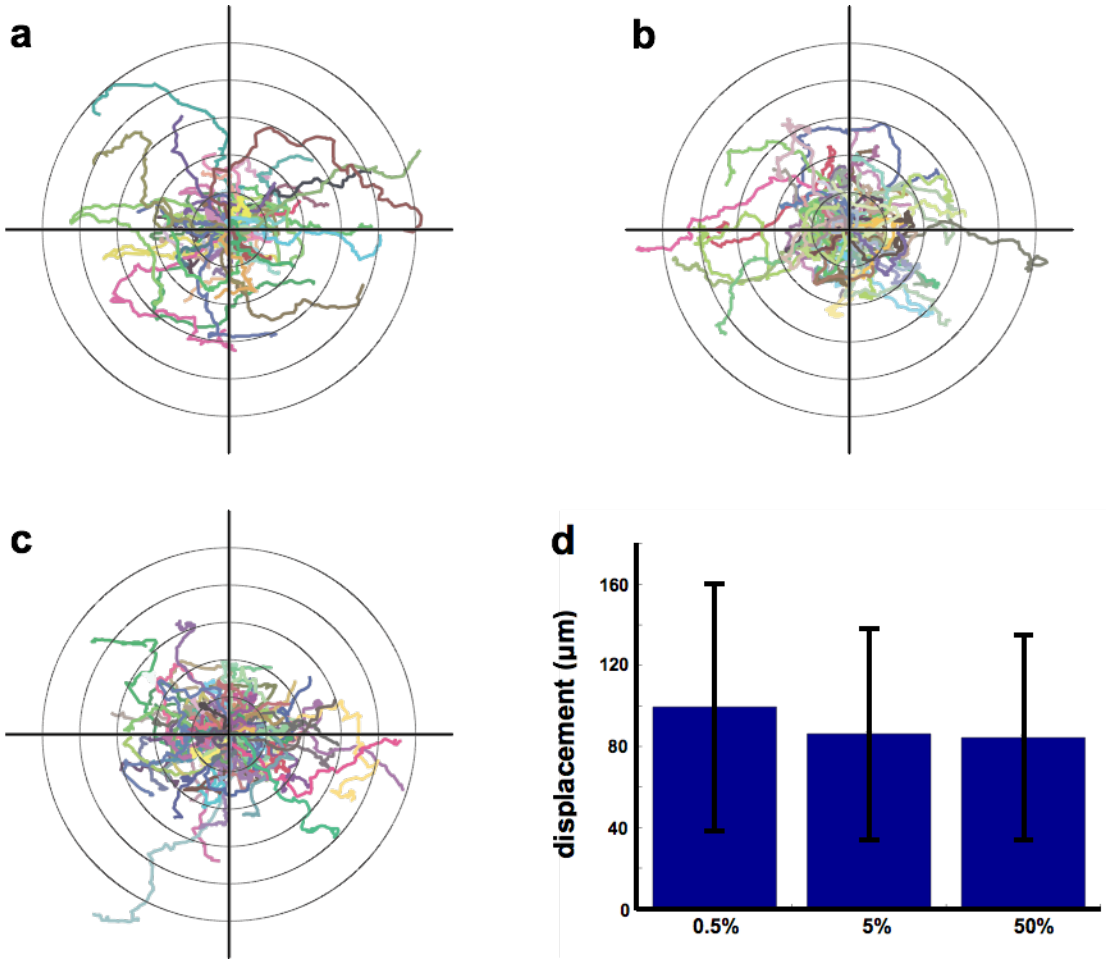

Figure 4.12: Comparison of neutrophil dispersal on different levels of PEG-ylated, uniform IL-8. a. 0.5% **(**1 µg/mL avidin + 199 µg/mL BSA), **b.** 5% **(**10 µg/mL avidin + 190 µg/mL BSA), **c.** 50% **(**100 µg/mL avidin + 100 µg/mL BSA). The distance between the neighboring concentric rings is 50 µm. **d.** Statistical comparison of neutrophil displacement on a, b, and c. Student's *T*-test at the alpha level of 0.05 (two-tailed, assuming unequal variances) indicates that there are no significant differences.

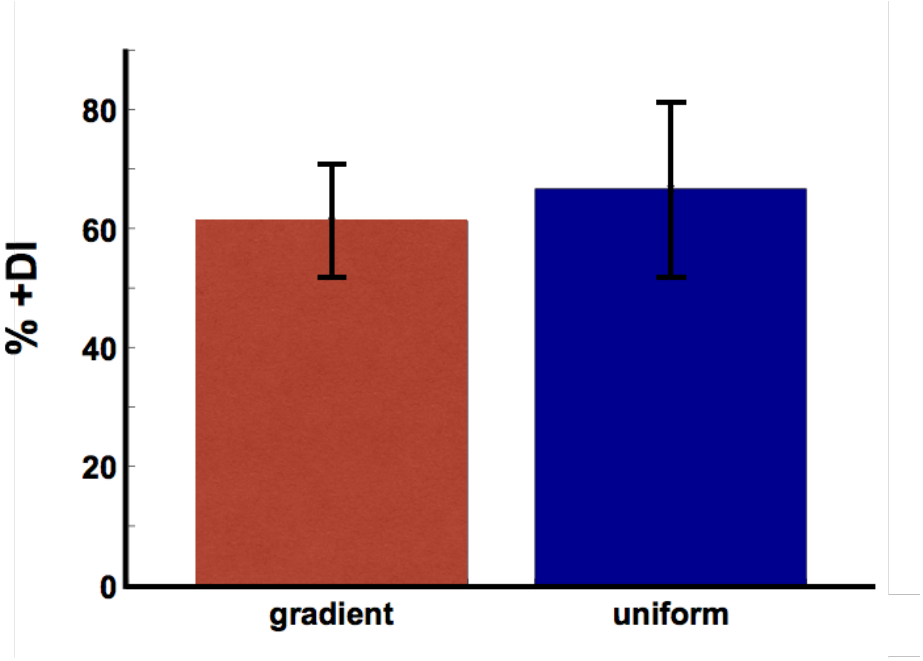

Figure 4.13: Comparison of migratory directionality on PEG-ylated IL-8 gradient and uniform IL-8. The y-axis indicates the percentages of cells migrating in the direction of higher surface densities of IL-8. Student's *T*-test at the alpha level of 0.05 (two-tailed, assuming unequal variances) indicates that there was no significant difference in the general directionality of cells on the substrates coated with uniform IL-8 and IL-8 gradient.

4.4.10 Comparison of Current IL-8 Haptotaxis Study with Prior Art

A previous study [12] has found that more neutrophils transmigrated through a positive haptotactic membrane than through a negative haptotactic membrane, which strongly suggests the occurrence of haptotaxis. While this suggestion contrasts with the absence of haptotaxis in our migration studies, the data themselves are not in direct disagreement. In our study, we examined only neutrophils that migrated for more than 30 μm in displacement, whereas in the previous study this condition is not imposed. Even though the investigator did describe the pore size (diameter = 3 μm) of the polycarbonate

membranes used in their Boyden chambers, they did not describe the thickness. Based on the available products offered by the manufacturer (formerly Nucleopore, Pleasanton, CA), it is likely that the membrane used is only 10 μm in thickness, on par with the size of the neutrophil. Therefore the migrations examined in the previous study are short in the migratory displacements.

Furthermore, we have also noticed in our initial experiments that most neutrophils are stuck (displacement < 30 μm) on the substrates coated only with IL-8 or without the adhesion molecules (*i.e.*, BSA and ICAM-1) (Fig. 4.14). It is therefore possible that many neutrophils cannot transmigrate through the negative haptotactic membrane due to the excess of IL-8 that switched the neutrophils to phagocytose the substrate instead of migrating, and the lack of adhesion molecules to appropriate the migration. It is worth noting that adhesion molecules (such as BSA) are not intentionally added in the study, so the only source of adhesion molecules are the blood serum proteins that remained after the neutrophil isolation procedure. We have also examined the %+DI for neutrophils that migrated for less than 30 μm and again found no significant difference from the haptokinenesis control.

Further studies are required to definitively demonstrate the existence of neutrophil haptotaxis on IL-8 and ICAM-1. Nevertheless, while flow assisted adhesion and haptotaxis may both aid in the recruitment of neutrophils toward sites of inflammation, the former is likely the more effective mechanism.

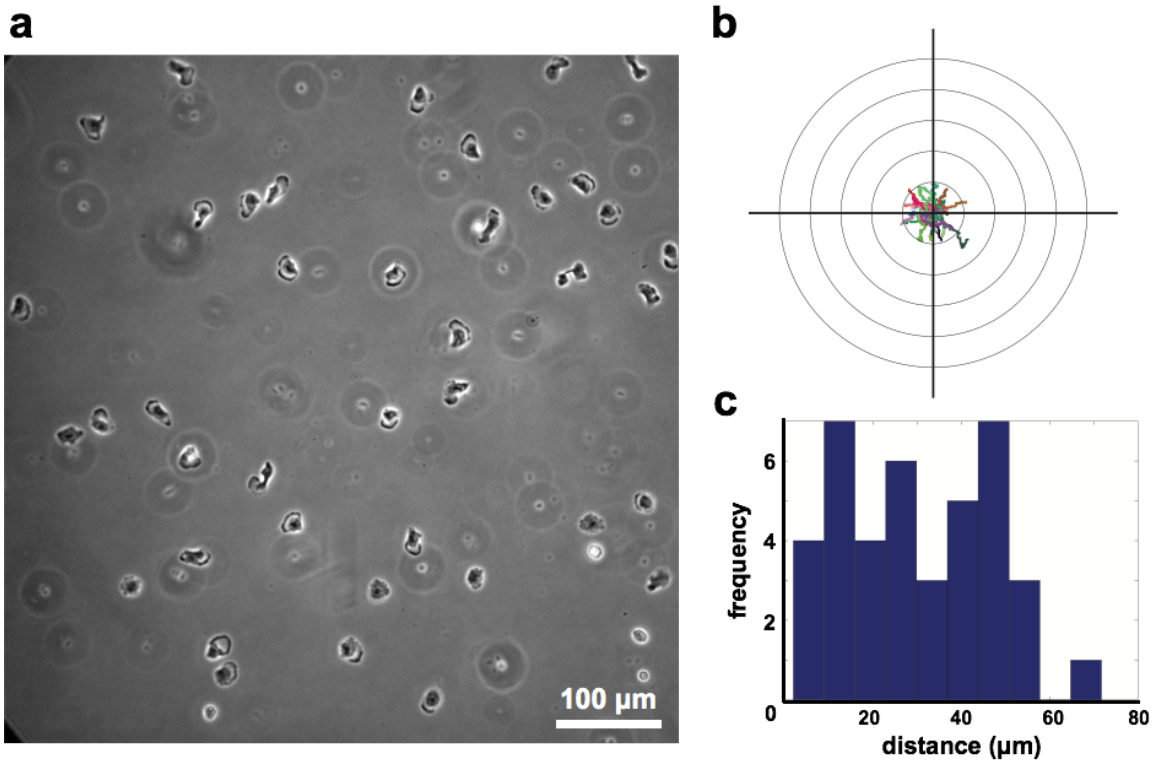

Figure 4.14: Example of neutrophils on a substrate coated with IL-8 only. a. Morphology of neutrophils on the substrate with IL-8 only. As seen, most neutrophil are fully spread, some even have multiple sites of polarization (indicated by the red arrows). **b.** Radial graph of cell migration. The distance between the neighboring concentric rings is 50 µm. In comparison to the substrates where adhesion molecules are also present (*e.g.*, Fig. 4.3 and Fig. 4.12), the cells are less dispersive in their migration. **c.** Histogram of migratory displacement. As indicated, ~50% of the cells do no migrate more than 30 µm in displacement.

4.5 Summary and Conclusions

We set out to determine if a directed migration of neutrophils can be induced on ICAM-1- and IL-8- modified substrates, using different protocols of surface modifications, including direct adsorption or the use of IgG- and PEG- based linkers, to create immobilized gradients of different steepness and mean level of surface density. However, of all the approaches taken, none were able to promote an effective haptotaxis of neutrophils. While the physiological implications of haptotaxis remained to be further explored, the standard operating procedures established in this work, with or without the linker extension, are readily applicable to other molecules for the direct migration or growth of different cell types. A number of useful outcomes were obtained from the present efforts. These include:

1. A 1st order approximation of the reagents and the times required to fully saturate a surface in a flow channel.
2. An automated image processing tool to measure the various parameters of cell motility.
3. A statistically rigorous framework to detect the presence of haptotaxis.

We have demonstrated that IgG-based linkers allow the formation of immobilized gradients that are highly reproducible, with well characterized binding kinetics. Unfortunately this chemistry is not stable at 37°C. We have also demonstrated the use of biotin-PEG-NHS as a linker for IL-8 immobilization. While the PEG-based linker can covalently immobilize many different types of candidate chemoattractants, it is less consistent in reproducing gradients with the same density profile. This may be due to the

randomness associated with the promiscuity of the NHS in protein binding or premature hydrolysis of the reactive group. Therefore an improvement or a replacement of the biotin-PEG-NHS linker chemistry might improve the consistency of immobilized IL-8 gradients that remain stable at 37°C.

4.6 References

1. Carter, S.B., *Haptotaxis and the mechanism of cell motility*. Nature, 1967. **213**: p. 256-260.
2. Tonetti, M.S., M.A. Imboden, and N.P. Lang, *Neutrophil Migration Into the Gingival Sulcus Is Associated With Transepithelial Gradients of Interleukin-8 and ICAM-1**. Journal of Periodontology, 1998. **69**(10): p. 1139-1147.
3. Sumagin, R. and I.H. Sarelius, *Intercellular adhesion molecule-1 enrichment near tricellular endothelial junctions is preferentially associated with leukocyte transmigration and signals for reorganization of these junctions to accommodate leukocyte passage*. The Journal of Immunology, 2010. **184**(9): p. 5242-5252.
4. Martich, G.D., et al., *Detection of interleukin 8 and tumor necrosis factor in normal humans after intravenous endotoxin: the effect of antiinflammatory agents*. The Journal of Experimental Medicine, 1991. **173**(4): p. 1021-1024.
5. Van Zee, K.J., et al., *IL-8 in septic shock, endotoxemia, and after IL-1 administration*. The Journal of Immunology, 1991. **146**(10): p. 3478-3482.
6. DeForge, L.E., et al., *Biphasic production of IL-8 in lipopolysaccharide (LPS)-stimulated human whole blood. Separation of LPS-and cytokine-stimulated components using anti-tumor necrosis factor and anti-IL-1 antibodies*. The Journal of Immunology, 1992. **148**(7): p. 2133-2141.
7. Nupponen, I., et al., *Neutrophil CD11b expression and circulating interleukin-8 as diagnostic markers for early-onset neonatal sepsis*. Pediatrics, 2001. **108**(1): p. e12-e12.
8. Webb, L., et al., *Binding to heparan sulfate or heparin enhances neutrophil responses to interleukin 8*. Proceedings of the National Academy of Sciences, 1993. **90**(15): p. 7158-7162.
9. Witt, D.P. and A.D. Lander, *Differential binding of chemokines to glycosaminoglycan subpopulations*. Current Biology, 1994. **4**(5): p. 394-400.
10. Kuschert, G.S.V., et al., *Identification of a glycosaminoglycan binding surface on human interleukin-8*. Biochemistry, 1998. **37**(32): p. 11193-11201.
11. Schlorke, D., et al., *The influence of glycosaminoglycans on IL-8-mediated functions of neutrophils*. Carbohydrate Research, 2012. **356**: p. 196-203.
12. Rot, A., *Neutrophil attractant/activation protein-1 (interleukin-8) induces in vitro neutrophil migration by haptotactic mechanism*. European Journal of Immunology, 1993. **23**(1): p. 303-306.
13. Dertinger, S.K.W., et al., *Gradients of substrate-bound laminin orient axonal specification of neurons*. Proceedings of the National Academy of Sciences, 2002. **99**(20): p. 12542-12547.
14. Jiang, X., et al., *A general method for patterning gradients of biomolecules on surfaces using microfluidic networks*. Analytical Chemistry, 2005. **77**(8): p. 2338-2347.
15. Jeon, N.L., et al., *Generation of solution and surface gradients using microfluidic systems*. Langmuir, 2000. **16**(22): p. 8311-8316.

16. Ehrenberg, M.S., et al., *The influence of protein adsorption on nanoparticle association with cultured endothelial cells*. Biomaterials, 2009. **30**(4): p. 603-610.
17. Dertinger, S.K.W., et al., *Generation of gradients having complex shapes using microfluidic networks*. Analytical Chemistry, 2001. **73**(6): p. 1240-1246.

4.7 Supplementary Information Section (SIS§)

4.7.1 1st Order Estimate for Why the Protein Adsorption is Not Diffusion-limited

During a static coating, the characteristic time τ_D required for the proteins to interrogate up and down the height of the flow channel can be described by 1D diffusion, and is given by:

$$\tau_D = \frac{\delta^2}{2D} \qquad (4.7.1)$$

where δ is the characteristic distance covered by the protein and D is the diffusion coefficient of the protein, obtained by:

$$D = \frac{KT}{6\pi r\eta} \qquad (4.7.2)$$

where K is Boltzmann's constant, T is temperature, η is fluid viscosity, and r is hydrodynamic radius of the diffusing protein. At room temperature (25 °C), KT takes on the value of 4.112×10^{-21} N·m.

After substituting Eqn. 4.7.2 into Eqn. 4.7.1 with $\delta = h/2$ (half-height of the rectangular channel), the time τ_D required for surface saturation is given by

$$\tau_D = \frac{3}{4}\left(\frac{\pi r\eta h^2}{KT}\right) \qquad (4.7.3)$$

According to Eqn 4.7.3, the diffusion of the protein G, avidin, and IL-8 (r ~2-3 nm) up and down the 50-μm tall flow channel of our flow-mixing gradient generator is complete in within a minute. Since surface saturation in our experiment generally requires ~20 min, the adsorption of the protein to the substrate is likely to be reaction-limited, not diffusion-limited.

Chapter 5
Concluding Remarks

5.1 Pnc-Si-based Shear-free Chemotaxis System

5.1.1 Summary of Findings

We successfully directed the migration of neutrophils using a flow-generated gradient of fMLP and screened the flow from directly exerting forces on the neutrophils with the use of a thin, nanoporous membrane. With the membrane, the shear stress seen by the neutrophils was five orders of magnitude less than that without, effectively rendering the system shear-free. While the fMLP gradient can propagate through the membrane and retain its linearity, a substantial decrease in steepness occurs because lateral diffusion tends to smooth any concentration differences as the gradient diffuses to the cell compartment floor. Lastly, we demonstrated that the migrated neutrophils can be fluorescently-labeled and washed without their positions being altered.

5.1.2 Future Directions

In terms of design improvement, we plan to replace the flow-mixing gradient generator with the T-sensor as the main mechanism for forming the gradient (both are described in details in Section 1.2.3 of Chapter 1). While the T-sensor generally requires

a long mixing zone to diffusively smooth a concentration jump to a more linear gradient, in the case of our membrane-based system this is actually an advantage. The yet to be linear gradient will be fully linear once it passed through the membrane and reached the floor of the cell hosting-space. Additionally, in comparison to the flow-mixing gradient generator, the T-sensor is simpler in design, confers less flow resistance, and is less susceptible to flow blockage because it has larger channel size and fewer flow channels. Since the T-sensor is generally smaller than the premixer gradient generator, less area is required for the T-sensor to bond to the silicon chip that hosts the membrane. This translates to more chips per silicon wafer and a substantial reduction in cost on a per chip basis.

We also plan to integrate on-chip valves to regulate multiple flow streams, that each carries a different solute or concentration, to regulate the biochemical environment of the cell-hosting space. One immediate functionality gained is the ability to quickly switch the parity of the gradient to study how fast the neutrophil can turn. By orchestrating a set of valves in peristalsis, flow pumping can also be achieved. This will eventually eliminate the need of bulky external flow pumps and long lengths of tubing.

In terms of immediate contribution to understanding neutrophil migration, we can use the pnc-Si-based system to test the hypothesis that activated LFA-1 clusters steer the migration of the neutrophil, while Mac-1 is sequestered to the uropod to provide a basal level of adhesion. This hypothesis was alluded to, but not confirmed by the study of Heit *et al.* (described in Section 1.1.6 of Chapter 1). Specifically, we can sequentially label migrating neutrophils and observe how LFA-1 and Mac-1 organize over the cell

membrane. LFA-1 blocking antibody can then introduced to the migrating neutrophils to see if there is a loss of migration directionality or a disruption in the clustering of LFA-1.

5.2 Analytical Model of Flow Reduction

5.2.1 Summary of Findings

As the flow passes by each pore in the flow channel, a portion enters the cell compartment, gradually building up the flow magnitude. However, the cell compartment flow would eventually return to the flow channel to conserve the total mass that exits the system through the flow channel. Due to system symmetry, the rate of flow returning to the flow channel is a mirror image of the rate of flow entering the cell compartment. Thus the maximum flow in the cell compartment would always be at the center of the cell compartment. No matter how flow-resistive each pore is, for a membrane that is sufficiently long, eventually enough flow would have entered the cell compartment such that the absolute flow rate maximum would be reached. This flow rate maximum is equal to the product of the input flow rate and the ratio of the resistance of the flow channel to the sum of resistance of the flow channel and the cell compartment. The key to maintaining the cell compartment shear-free is to have sufficiently resistive pores and a sufficiently short membrane so that the flow starts to leave the cell compartment before a significant built-up in magnitude. The 1D analytical model successfully captured these key system attributes, and accurately described the magnitude of the cell compartment flow as a function of the distance along the length of the membrane. Importantly, the

analytical model allows the prediction of when the absolute flow rate maximum will be attained, and provided the following simple rules of thumb to predict cell compartment flow: the maximum flow seen is dependent on the pore radius to the second power, linearly proportional to the porosity and the input flow, and inversely proportional to the membrane thickness.

We have also provided a simple method to convert an array of pores into one homogenous medium with a defined permeability. This methodology allows CFM simulations to be performed at a much faster pace because it eliminates the large discrepancy of dimensions in the different system components. Instead of meshing geometry that transitioned six orders of magnitude (from the nano- to the centimeter domain), a transition of three orders of magnitude is sufficient for yielding an accurate prediction of cell compartment flow.

5.2.2 Future Directions

The configuration of two compartments separated by a flow-permeable medium is common to many tissues and microfluidic systems. We plan to use the same analytical framework but vary the boundary conditions to predict the fluid transport for different scenarios. These include:

1. Flow of opposite directions at either side of the membrane, as in the case of counter-current dialysis.

2. An open reservoir (to atmosphere) on one side of the membrane. This is analogous to the micro-jet system showcased by Keenan et al. and VanderSarl et al. [1, 2]. We believe

the ease of access offered by the open-top system, such as the exchange of media and cells through manual pipetting, will make the system user-friendly and allows a gain in popularity over the Transwell/Boyden chamber in chemotaxis and drug permeation studies. An understanding of the fluid transport in such systems is therefore essential for a well-controlled experiment.

While it may also be important to understand how diffusion and convection are coupled to influence solute transport in the membrane-based system, our current experience suggests that as long as the flow reduction is significant, the solute diffusion can be modeled independently. This is supported by the observation that a purely diffusive model alone is able to predict the steady-state concentration profile of the gradient at the cell compartment floor.

5.3 Gradient Immobilization

5.3.1 Summary of Findings

While we were able to immobilize IL-8 and ICAM-1 gradients of different steepness and mean level of surface density through either direct adsorption or linker extension, none of the gradients were able to promote the directed migration of neutrophils. Control experiments on neutrophil activation and adhesion indicated that both the IL-8 and the ICAM-1 retained their function after immobilization, therefore the absence of directed migration is not due to loss of function. Despite the failure to observe haptotaxis, we learned a great deal about surface functionalization. We are able to estimate the amount

of protein and the time required to saturate a substrate, as well as the range of the flow velocity for immobilizing specific gradient profiles. The combination of protein G and IgG allows the formation of gradients with highly reproducible profiles of surface density. We have also experimented with the combination of avidin and biotin-PEG-NHS linker to immobilize IL-8 gradients. While the NHS-mediated bonding allows the covalent immobilization of many different kinds of protein, the bonding is less specific. Consequently, the immobilized gradients tend be less reproducible, and have lower steepness and mean level of surface density.

We have automated the cell tracking and the measurement of key motility parameters to characterize cell migration. Some of these include speed, pathlength, displacement, persistence, and the general direction of migration. If the substrate was fluorescently-labeled, the change in the speed and the direction of the cells can also be correlated to the local profiles of surface density. Lastly, we have also formalized a novel statistical method to detect the presence of directed migration.

5.3.2 Future Directions

The IgG-based linker chemistry offered many promising applications. Different regions of the same substrate can be functionalized with different antigen-specific IgG to detect a specific library of cells. These include immune cells, infectious microbes, and even viruses. Post detection, the bound cells can be harvested by introducing non-interacting IgG to displace the antigen-specific IgG off the protein G. While the detection relies on an all-or-nothing adhesion rather than a functional migration, the assay produces

cleaner readouts that are easier and faster to analyze (*i.e.*, number of cells vs migration of cells). The need to direct the flow of the cells and the IgG for the coating and the subsequent collection further emphasizes the importance of on-chip valves.

5.4 References

1. Keenan, T.M., C.-H. Hsu, and A. Folch, *Microfluidic "jets" for generating steady-state gradients of soluble molecules on open surfaces.* Applied Physics Letters, 2006. **89**(11): p. 114103.
2. VanDersarl, J.J., A.M. Xu, and N.A. Melosh, *Rapid spatial and temporal controlled signal delivery over large cell culture areas.* Lab on a Chip, 2011. **11**(18): p. 3057-3063.